2013

Phase behavior of silica-polypeptide hybrid particles immersed in cholesteric liquid crystals

Melissa Elizabeth Collins
Louisiana State University and Agricultural and Mechanical College, mcolli4@tigers.lsu.edu

Follow this and additional works at: https://digitalcommons.lsu.edu/gradschool_dissertations

Part of the Chemistry Commons

PHASE BEHAVIOR OF SILICA-POLYPEPTIDE HYBRID PARTICLES IMMERSED IN
CHOLESTERIC LIQUID CRYSTALS

A Dissertation

Submitted to the Graduate Faculty of
Louisiana State University and
Agricultural and Mechanical College
in partial fulfillment of the
requirements for the degree of
Doctor of Philosophy

in

The Department of Chemistry

by
Melissa Elizabeth Collins
B.S., Louisiana State University, 2003
M.S., Louisiana State University, 2007
December 2013

TABLE OF CONTENTS

LIST OF TABLES

LIST OF FIGURES

ABBREVIATIONS AND SYMBOLS

D_{app}	Apparent diffusion coefficient
AF4	Asymmetric Field Flow Fractionation
x	Axial ratio
k_B	Boltzmann's constant
CAMD	Center for Advanced Microstructures and Devices
CLCs	Cholesteric Liquid Crystals
c	Concentration
Γ	Decay time
$\rho(\boldsymbol{r})$	Density distribution
DFT	Density Functional Theory
DDLS	Depolarized Dynamic Light Scattering
d	Diameter
DWS	Diffusing Wave Spectroscopy
DMF	Dimethylformamide
μ	Dipole moment
DC	Direct Current
$\boldsymbol{r}$	Direction vector
h	Distance
DLS	Dynamic Light Scattering
E	Electric field
EV	Electron Volts
FFF	Field Flow Fractionation

FITC	Fluorescein isothiocyanate
F	Free energy
GPC	Gel Permeation Chromatography
R_{geom}	Geometric radius
GUI	Graphical User Interface
HCP	Hexagonal Close Packed
H	Horizontal polarization
R_h	Hydrodynamic radius
I.D.	Inside Diameter
I	Intensity
L	Length
LC	Liquid Crystal
mV	Milivolts
MW	Molecular Weight
MALS	Multi-Angle Light Scattering
DMF	N,N-dimethyformamide
NCA	N-carboxyanhydride
O.D.	Outside Diameter
r	Particle Radius
PTA	Phosphotungstic acid
PCS	Photon Correlation Spectroscopy
π	Pi
POM	Polarized Optical Microscopy

PBLG	Poly(γ-benzyl-L-glutamate)
PNIPAM	Poly(N-isopropylacrylamide)
PSLG	Poly(γ-stearyl-α-L-glutamate)
PS	Polystyrene
PTFE	Polytetrafluoroethylene
PTFE	Polytetrafluoroethylene
PVDF	Polyvinylidene fluoride
W	Potential
QELS	Quasi-Elastic Light Scattering
R_g	Radius of gyration
RI	Refractive Index
D_r	Rotational diffusion
θ	Scattering angle
q	Scattering vector
s	Second
t_{shell}	Shell thickness
SAXS	Small Angle X-ray Scattering
η	Solvent viscosity
SLS	Static light scattering
σ	Surface density
T	Temperature
TEOS	Tetraethyl orthosilicate
THF	Tetrahydrofuran

t	Time
TMV	Tobacco Mosaic Virus
D_t	Translational diffusion
TEM	Transmission Electron microscopy
UV-vis	Ultraviolet-visible spectroscopy
U	Unpolarized
V	Vertical polarization
ϕ_r	Volume fraction of rods
λ_0	Wavelength in vacuo
WAXS	Wide Angle X-ray Scattering

ABSTRACT

Silica-polypeptide hybrid particles are core-shell colloids. Established synthetic methods ensure uniformly sized cores and provide the ability to have magnetic or fluorescent inclusions. The polypeptide shell is highly functional in its ability to respond to stimuli through changes in shape and formation of ordered phases above certain concentrations or temperatures. This research explores the interactions of hybrid particles mixed with polypeptides dispersed in solution. Depletion theory, which considers mainly entropic interactions between particles, can be used to explain the phase behavior of colloids. Due to the chemical similarities between the polypeptides attached to the surface and those free in solution, enthalpic interactions are considered to be negligible. The primary polypeptide employed in this dissertation is poly (γ-benzyl-L-glutamate), PBLG, which is capable of forming liquid crystalline phases on its own.

Phase behavior of the colloidal particles combined with polypeptides was monitored by polarized optical microscopy (POM) to determine the onset of the liquid crystalline phase. Wide-angle X-ray scattering (WAXS) was used to gain information about the crystalline structure of the mixtures. Further characterization of hybrid particles by hydrodynamic modeling established that their behavior is indeed core-shell in solution and depends on shell density and length. Poly (tetrafluoroethylene) latex was analyzed by depolarized dynamic light scattering (DDLS) as a precursor to the study of magnetic hybrid particles which also have a depolarizing affect.

CHAPTER 1. GENERAL INTRODUCTION

1.1 Colloids

Interest in colloidal mixtures dates back to the early 1900s when latex was first discovered. Since then scientists have sought to learn as much as possible about the unique characteristics of colloidal systems. Colloids are defined as particles of one phase dispersed in a medium of a different phase with a particle size ranging from approximately 1 nanometer to 1 micron.[1] Colloidal particles can take on the form of droplets of liquid or hard particles that remain suspended in solution for some time. Well-known colloidal mixtures include aerosols, paints, and foams. Ideally, they exist in stable dispersions, but they are easily destabilized and often require modification in order to maintain their ordered arrangement. The particles can be stabilized by charge,[2] surfactants,[3] or incorporation of other particles[4] into the colloidal matrix. When colloids are destabilized, the particles aggregate. The tendency towards aggregation can be measured by examining the zeta potential of a dispersed particle, where high potentials (greater than 40 mV) correspond to more stable mixtures.[5] Colloidal particles fall into a defined size range, but not necessarily a defined shape. Spherical is the most familiar, followed by rods and disks, but with new technologies capable of fabricating more detailed shapes, colloidal particles now include uniformly-sized rings, tetrahedra, and ellipsoids.[6-9]

Colloidal suspensions are often studied when individual particle characteristics are desired, but increases in particle concentration do not always lead to an amorphous aggregate. In some instances, depending on shape, size, density, etc. colloidal crystals form. Colloidal crystals are defined by an ordered array of microparticles where a crystalline packing arrangement can be assigned. For example, monodisperse silica microspheres organize into a hexagonal close packed (HCP) crystal.[10] Opal is a naturally occurring colloidal crystal[11] whose aesthetic value arises

from the many colors visible at the surface. Colloidal crystals diffract certain wavelengths of light, based on the size of the interstitial regions, making it a useful tool for developing materials with tuned optical properties.[12, 13]

The colloidal properties obtained from a system potentially depend on whether the system is dilute or concentrated. In dilute systems colloidal particles experience unrestricted Brownian motion, a random trajectory imposed by multiple collisions with solvent molecules. These random motions can be correlated to determine diffusion behavior, which leads to information about size or shape.[14] In more concentrated systems, interactions between particles come into play and physical parameters such as surface charge and excluded volume, which dictates the distance between colloids, provides information about how the colloidal particles assemble or aggregate.[15, 16] Chapter 3 of this dissertation deals with colloidal interactions between hybrid particles and rodlike polymers, specifically ones that are capable of self-assembly into ordered structures.

1.2 Polypeptides

1.2.1 General Properties

When amino acids form covalent bonds the resultant functional group is an amide and the neighboring carbon bears a pendant group. There are 22 possible variations of this pendant group that make up the standard set of amino acids.[17] The conformation of the side chain attached to the backbone takes on either an (L) or (D) descriptor based on the direction in which it rotates polarized light. The length of the chain determines the terminology used to refer to it. Up to 50 amino acids is commonly referred to as a peptide, where a polypeptide can contain over a thousand amino acids. The structure of proteins, comprised of amino acids, has four primary levels of complexity: primary, secondary, tertiary and quaternary. Primary is concerned with the

sequence of amino acids that make up a polypeptide. Secondary structures, the alpha helix and beta sheet, ensue once chains are long enough to form intramolecular hydrogen bonds. Tertiary structure refers to the entire folded conformation of a protein made up of many polypeptides and quaternary is composed of an oligomeric assembly of subunits. Both tertiary and quaternary are much larger in size than the polymers studied here.
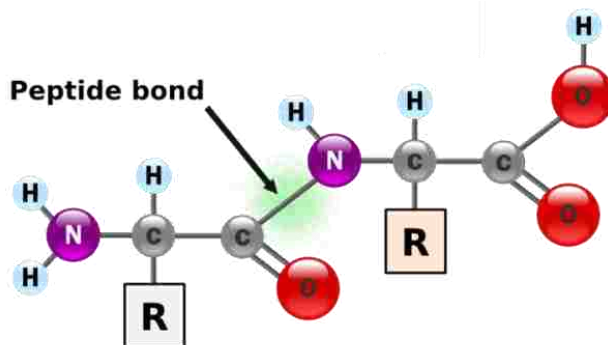
Figure 1.1 Structure of a peptide bond between two amino acids. "R" refers to the pendant group that defines the peptide.

Synthetic poly (α-amino acids) have been used extensively not only for mimicking protein behavior, but because of their predictable nature they are often modified and incorporated into other polymers, particles and fibers. Pauling and Corey[18-20] were the first to report the alpha helical structure of poly (α-amino acids), where hydrogen bonding between the oxygen of the carbonyl and the hydrogen attached to the backbone nitrogen stabilize the structure. There also exists a 3_{10}-helix with only three residues per turn, but of the two, the alpha helix is more stable and the most common secondary structure found in nature.[21] In beta-sheet arrangement hydrogen bonding again serves as the stabilizing force for the structure, but the polymer is extended with bonding between parallel sheets.[22-24]

When regular order does not exist in the structure the polymer conformation is referred to as random coil. Polypeptides are not locked into a particular secondary structure; they are

capable of reversibly changing from α-helical to random coil with varying temperature or solvent conditions.[25] Often helical polypeptides have intermittent regions of disorder where they randomly coil and display a lack of structure at the ends of the helix.[26, 27]
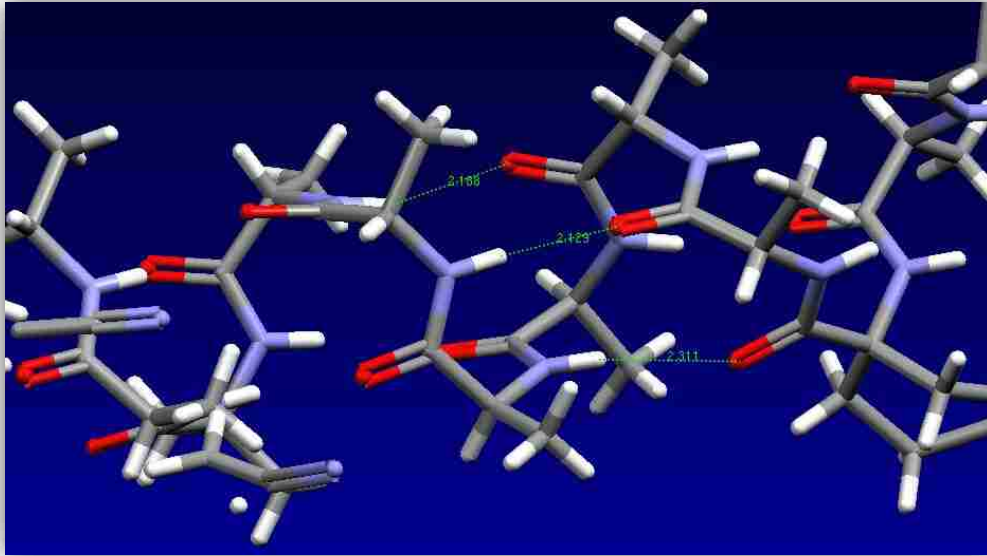
Figure 1.2 Hydrogen bonding in a generic α-helical polypeptide. The green dashed lines follow the direction of hydrogen bonding and the corresponding numbers are the length over which it extends.
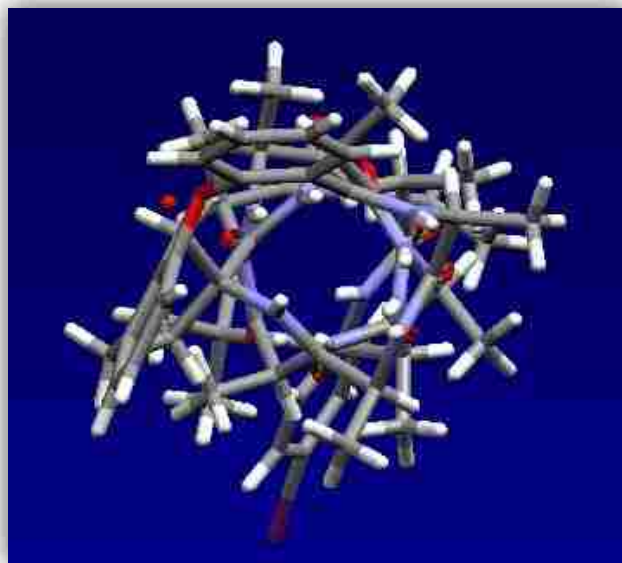
Figure 1.3 Axial view of a generic α-helical polypeptide. Side chains extend outward from the central axis.

Figure 1.2 shows the hydrogen bonding of a generic polypeptide. The green dashed lines refer to the path of interaction between the carbonyl oxygen and the hydrogen extending from the nitrogen. The corresponding numbers are the lengths of the hydrogen bonds measuring just over 2 Å (SYBYL software, Tripos, Inc. St. Louis, MO), which are similar to values obtained by Aravinda.[28] The α-helical structure also works to minimize steric repulsion. An axial view of the polypeptide is shown in Figure 1.3 where pendant groups extend outward from the backbone. As the molecule curves around, a staggered arrangement is created where each pendant group is slightly rotated from the next.

1.2.2 Poly (γ-benzyl-L-glutamate) (PBLG)

1.2.2.1 Structure

When a polypeptide consists of a single type of amino acid it is referred to as a homopolypeptide. They are frequently synthesized as useful tools for studying a particular property of one amino acid. PBLG in particular is one of the most studied synthetic polypeptides given the ease of synthesis, lengths over which it maintains its rodlike structure and solubility in a number of solvents at a range of temperatures.[22, 29-87]
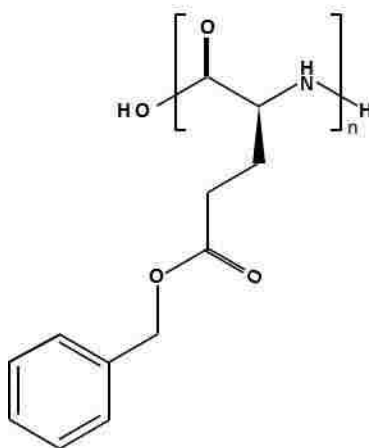
Figure 1.4 Structure of Poly (γ-benzyl-L-glutamate).

The most stable conformation of α-helical PBLG is an 18/5 helix, where 18 refers to the number of residues and 5 refers to the number of helical turns required. A 7/2 helix is also found for PBLG, but it is less stable and irreversibly converts to an 18/5 helix.[88, 89] The average number of residues per turn in the more stable conformation is 3.6. Polypeptide length is calculated by taking into consideration that each peptide residue covers 1.5Å in linear height.[90] As a result of these dimensions, a simple equation can be used to calculate the contour length of a polypeptide chain.

$$Length \ (\text{Å}) = \frac{MW_{polypeptide}}{MW_{monomer}} * 1.5 \qquad (1.1)$$

Synthesis of the PBLG monomer begins with L-glutamic acid; commonly studied due to its numerous biomedical applications and uses in food science.[91-93] Esterification with benzyl alcohol leads to the formation of benzyl-L-glutamate (BLG), and finally, treatment with an acyl chloride yields the N-carboxyanhydride (NCA) of BLG. Polymerization follows through a ring-opening process with a basic initiator, where choice of initiator corresponds to differences in molecular weight.[93] Addition of each monomer leads to the elimination of carbon dioxide gas, which also serving as an indicator of the progression of the reaction.[34]

1.2.2.2 Solvent Interactions

Solvent plays a large role in the behavior of a polymer. For example, we ascribe the terms good, poor or theta to a solvent depending upon a polymer's reaction to it.[94, 95] For polypeptides, the solvent interactions affect whether the polymer adopts the helical conformation or random coil. Certain solvents are considered to be helicogenic, meaning the polymer maintains its α-helical state in solution. Doty *et al*[96] were among the first to study the shape and aggregation state of PBLG in solution by viscometry and light scattering. Since then several studies have been conducted to refine this list for various temperatures, molecular weights and

concentrations.[25, 26, 38, 48, 97-104] Helix-coil transitions have also been studied theoretically in order to determine the effect of neighboring peptides on those locked in the helical conformation.[98]

Dimethylformamide, m-cresol, dichloromethane and pyridine are typical helicogenic solvents. All have polarity in common, making them capable of dissolving PBLG, but all are aprotic so that they do not disrupt the hydrogen bonding; however, solubility of the polymer does not ensure the polymers are dispersed. Some solvents, such as THF and dioxane, lead to aggregation.[105]

Acidic solvents such as dichloroacetic acid and trifluoroacetic acid initiate the transition from helix to coil in PBLG by competitively hydrogen-bonding with available carbonyl oxygen or by protonation of the amide nitrogen.[99, 103] The full transition from helix to coil happens quickly upon solvation of the polymer as opposed to a slow unraveling of the helix.[38] Strong acids also debenzylate the side chain, resulting in glutamic acid or a polyelectrolyte.

In this dissertation most of the studies for PBLG are conducted in pyridine, which does not disrupt the helical form even though pyridine is capable of hydrogen bonding.[103, 106] Pyridine is a proton acceptor and would not easily compete with the polypeptide backbone carbonyl. Instead, it may be inclined to associate with the ester group of the side chain. Physically, the bulky benzyl group may provide steric hindrance from allowing pyridine, which is larger than the interstitials of the polymer chain, to interact with the core of the helix.

The same alignment of the amide groups along the polypeptide axis that allows for hydrogen bonding also gives rise to a net dipole moment on the polymer, which increases with the length of the polypeptide.[99, 105, 107] As a result, PBLG responds well to both electronic and magnetic fields. Because alignment of polypeptides creates birefringence, its optical properties are coupled to its electronic response and optical measurements become possible. Several

experiments conducted by Watanabe exploited the electo-optical properties of PBLG, where alignment of the polypeptide under various conditions in an electric field altered its optical properties.[99, 108-110] The dielectric constant, which is the response of the polymer to an electric field, is affected by solvent conditions,[105] polymer concentration,[100] and shear.[75] PBLG also exhibits a strong response to magnetic fields in solution or dried films.[73, 111-113]

Knowledge of PBLG's α-helical structure in solution permits study of its hydrodynamic behavior to determine the degree of rigidity of the polymer. Although it is often considered a rigid rod for simplification of calculations, PBLG displays some flexibility in solution.[114] It has been proposed that there are portions of the polymer chain that take on a random coil structure, sometimes referred to as "kinks," allowing bending of the chain leading to an overall description of PBLG as semi-flexible.[115] The persistence length of a polymer corresponds to the length over which it remains linear. This is much longer for α-helical polypeptides than it is for regular freely jointed chains or even polymers with extensively conjugated backbones.[116]

1.3 Liquid Crystals

1.3.1 General Properties of Liquid Crystals

Once confined to scientific discourse, liquid crystals (LCs) have now become part of our everyday language due to the popularity of liquid crystalline displays (LCDs). Their unique color properties that arise from the order of the material and its capability to manipulate light make LCs a beautiful subject for scientific study. What makes them useful materials to study is the fact that liquid crystals can be manipulated by temperature, concentration changes and electric and magnetic fields opening up an abundance of possibilities.

All molecules possess enough energy to vibrate in space, but the vibrations are minimal and do not disrupt the order. Figure 1.5 shows the rigid alignment of a solid crystal which

8

maintains order in the x, y and z planes. Alternately, a liquid's molecules are randomly arranged and are free to move and rotate in any direction. Liquid crystals combine these characteristics by allowing the molecules to have the freedom to translate and rotate, but only in certain directions. As a result the term mesomorphic, stemming from the Greek words middle and form or structure, is applied to liquid crystals as they possess characteristics of both solid crystals and liquids. The anisotropic particles or polymers that make up these phases are referred to as mesogens. When the particles are randomly positioned with no alignment in any direction, the system is called isotropic.
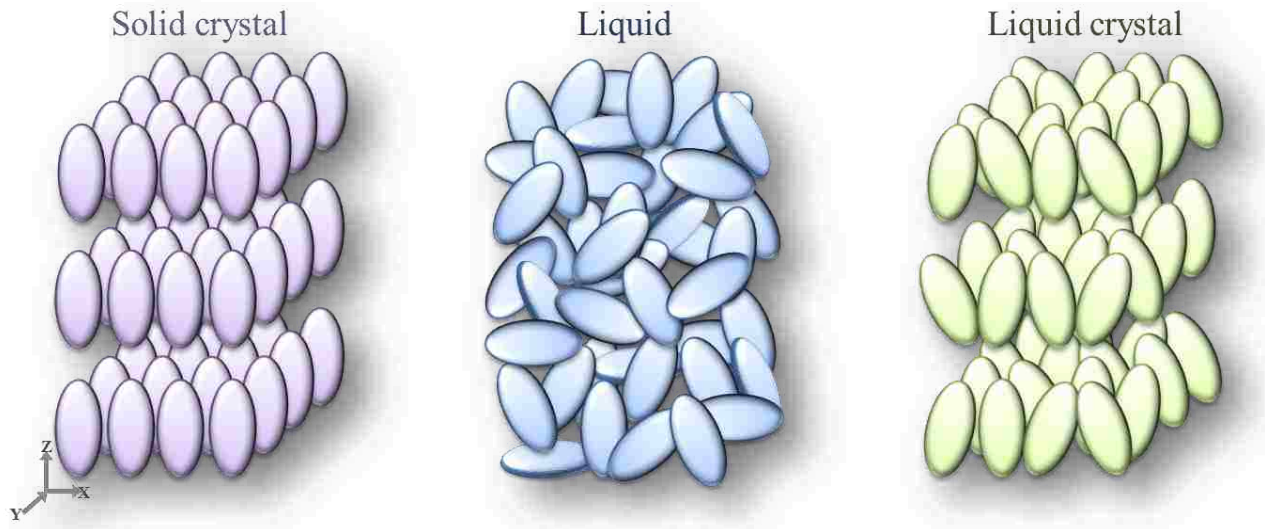
Figure 1.5 Molecules in the arrangement of a solid crystal, liquid, and liquid crystal.

Refractive index is a number that characterizes how light propagates through a material. When particles in a fluid have long-range alignment, light propagation through that fluid is affected. Liquid crystals are birefringent, meaning two refractive indices are present, because of the anisotropy of the particles. Under crossed polarized light microscopy (discussed more in Chapter 2) birefringent materials may display colors from its interaction with light. Isotropic solutions are not ordered and show no color in these types of experiments.

9

The primary categories of liquid crystal are called nematic, smectic, and cholesteric as defined by Friedel[117] with rodlike polypeptides participating in all three. Nematic liquid crystals are ordered only in the z-direction, parallel to the long axis of the molecule, the director. They are named for their appearance in some instances that resemble a threadlike structure. Smectics encompass a broad range of liquid crystalline order due to the many variations of the primary structure. The order most resembles a solid crystal in two planes, x and z, resulting in a layered organization, but in the y plane order is optional. Another subset applies to the tilt of the particle away from a central z-axis, which can vary with each layer. Subscripts and superscripts are assigned to each case with more than a dozen being identified so far.[118]

Cholesterics are of primary interest in this dissertation as it is the dominant structure adapted by PBLG. Cholesterics are also referred to as chiral nematics because of their helical superstructure, but are not typically put into the same category as nematics because of the large difference in structural behavior and optical properties. Cholesteric liquid crystals have a layered-type structure, but not similar to smectics. Within each horizontal plane there is order similar to a nematic, but each plane is twisted slightly from the one below giving an overall helical character to the structure. This twist is induced by the chiral nature of the polymers themselves.

The schematic of the cholesteric twist is shown in Figure 1.6A. A full 360° turn is considered to be the pitch of the helix, only half of that is depicted here. Alongside it is a typical cholesteric liquid crystal viewed in crossed polarized microscopy. Noticeable are the striations present in the sample that are characteristic of cholesterics. These light and dark patterns result from the polarization of light being alternately parallel then perpendicular to the long axis of the polymer. The cholesteric pitch varies with concentration of the solute, ionic strength of the

solvent, temperature, polymer length, or intentionally manipulated by the application of an electric field.[119-122]
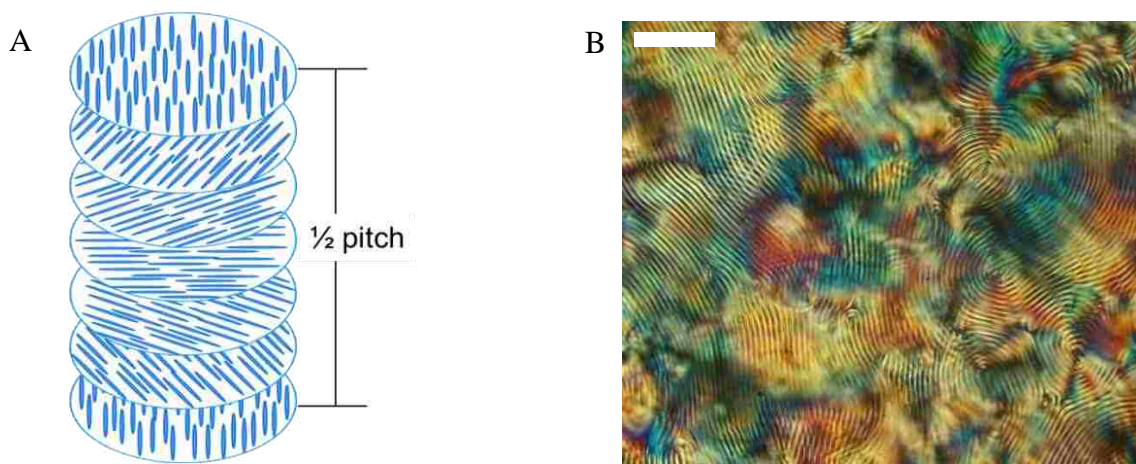
Figure 1.6 (A) Schematic showing the periodic changes in the director and (B) banding pattern of a cholesteric. Scale bar is 50 microns.

Cholesterics circularly polarize light as the electric field rotates in accordance with the director of each plane; following a helical pattern in space as the incident light propagates along the optical director.[123] Brilliant colors are reflected as CLCs interact with white light. A single color is reflected when the wavelength of light entering the helical twist is on the same order as the pitch. This selective reflection depends on pitch and slight changes result in the refection of different wavelengths. The ability to produce phototunable liquid crystals is important for the development of new display materials. Doping is another method commonly used to affect color. Use of azobenzene dyes that undergo tautomerization altering the orientation of the liquid crystal has become a popular technique.[124-126]

The condition for liquid crystal phase formation is characterized as either thermotropic or lyotropic. The phase transition for a thermotropic LC occurs with variation in temperature, while for lyotropic it depends on concentration.[77, 80, 81, 127] Not only polypeptides, but many other rodlike polymers form lyotropic liquid crystals, such as DNA,[128, 129] polysaccharides[130] and

cellulose derivatives.[131] The simplest phase formation, isotropic to nematic (I-N), has been described theoretically, experimentally, and by simulation. Flory[132, 133] and Onsager[134] are considered pioneers in the field of liquid crystals. Both constructed models for the transition of anisotropic particles in solution from random to ordered phases, but their models used different mathematical approaches. Flory applied a lattice theory where each point on the lattice is occupied by either a solvent molecule or a monomer unit.[127] Onsager was the first to show that the Density Functional Theory (DFT) approximated to the second virial coefficient could be applied to long, thin rods.[133] Since then his theory has been extended to include rods that are semi-flexible, charged, or possess a low aspect ratio.[135]

The transition from isotropic to crystalline is not sharp in lyotropic LCs. An intermediate region lies between the two phases where both isotropic and crystalline phases coexist. In the biphasic region, spherulites or large droplets of the crystalline phase form. Theoretical calculations for onset of the crystalline phase were established by both Flory and Onsager. Flory derived the transition from isotropic to biphasic as $\phi_A = (8/x)/(1-2/x)$, where $x = L/d$ and ϕ_B is the point at which the solution is completely cholesteric. Onsager's definition depends on a scaling of the axial ratio, $\phi_A = 4/x = 4d/L$, where d is diameter and L the length. According to Bu *et al.* the transition point for semiflexible chains begins at a slightly higher concentration than Onsager's theory predicts, but Flory's expectation is too high.[35]

1.3.2 PBLG Liquid Crystals

Synthetic PBLG was reported to be birefringent by Elliott and Ambrose in 1950 and a few years later Robinson reported extensively on the formation of PBLG liquid crystals.[61, 62, 128, 136] As mentioned previously, PBLG is widely used in studies of liquid crystalline behavior due to its rodlike shape. Most often PBLG takes the form of a cholesteric, but it can also adopt a

nematic or smectic arrangement under certain conditions. Solvent contributes to the handedness of the cholesteric helix. In 1,4-dioxane and chloroform the cholesteric is right-handed, but in dichloroethane it is left-handed. Mixtures of solvents that induce opposite twists constrain PBLG to a nematic state, likewise mixtures of left-and right-handed poly (γ-benzyl glutamate) result in a nematic liquid crystal.[127, 137] Application of a strong magnetic field also causes cholesteric PBLG cholesteric to untwist to a nematic where the optical axis is aligned parallel to the magnetic field. Both the strength of the magnet and the time allotted for transformation are factors. Weak magnetic fields align large domains of the cholesteric, but do not create a single nematic phase; in any case a sufficient amount of time is required for the transition due to the viscosity of the solution.[113, 138, 139]

PBLG falls under the category of lyotropic and forms liquid crystals in the organic solvents methylene chloride, dimethylformamide, and pyridine.[64] During the transition from isotropic to crystalline PBLG organizes itself into spherulites, which are droplets of liquid crystalline phase in the middle of an otherwise isotropic region, where their circular shape is attributed to the interfacial tension between it and the surrounding phase. Robinson noted that the transition from ϕ_A to ϕ_B has no strong dependence on molecular weight and the B point was typically at a concentration slightly above A for all molecular weights.

In the fully crystalline region PBLG takes on all of the characteristics mentioned for a cholesteric liquid crystal, including fingerprint texture and optical properties. The periodicity of the fingerprint pattern varies inversely with the square of concentration in both m-cresol and dioxane. Similar results were observed for methyl glutamate, but this does not imply it is the case for all polypeptides. Phase behavior diagrams for PBLG in various solvents have been developed. Russo and Miller showed that PBLG coexists as two different types of crystalline

phases at very specific concentrations and temperatures in DMF.[64, 65, 140] In solvent mixtures containing acid, random coil PBLG transitions to helical when heated allowing it to form a crystalline phase. As the mixture is further heated, it returns to the isotropic state.[48]

1.4 Hybrid Particles

Hybrid particles are prominent in scientific research due to the ample number of combinations possible for core-shell particles targeted to specific applications. They are multi-layered microspheres where each layer serves its own purpose. The structure is normally core-shell, where a dense or solid core is coated with a flexible, functional outer shell. This is the most common format, but rapid expansion of the field has made room for a variety of hybrid structures. The attractiveness of composite particles lies in the ability to create custom particles that can be tailored for a specific need.

Metallic nanoparticles, especially gold and silver, are often studied due to their optical, electrical, and chemical properties.[4, 5, 141, 142] The ability to functionalize these particles and study their physical behavior has been examined thoroughly, making them useful for composite particle research. Gold nanoparticle cores have been functionalized with liquid crystal–forming mesogens with the intent of creating ordered phases.[143] "Smart" particles were also constructed using a gold core and PNIPAM as the stimuli-responsive shell.[144] Silver nanoparticles, useful as catalytic agents, are likely to aggregate irreversibly. Coatings of PS-PNIPAM copolymers serve to stabilize the particles in solution while providing for stimuli-responsive behavior.[145]

The areas of application for composite particles are broad. Inorganic-organic microspheres were designed for antireflective coatings[146] and poly-lactic acid-coated silica particles are a biocompatible and biodegradable option for drug delivery and tissue regeneration.[147] Conducting particles, functionalized with disk-shaped mesogens,[148] were

designed to form columnar crystalline phases instead of the more traditional nematic liquid crystal.

The structure of the composite particle allows for creativity not only in determining which functions will be incorporated into the different layers, but the synthesis of the layers within. Malenovska's work includes synthetic feats such as tri-layer inorganic-organic-inorganic hybrid particles intended to push the boundaries of layered structures.[149] Other possibilities for composite particles are magnetic[150] or fluorescent[151] inclusions within the central core allowing for easy manipulation or observation of the particles. The approach to composite particles can be strictly pragmatic. Zorn *et al.*[152] attached diblock copolymers to nanorods solely for the purpose of solubilizing them, but their primary focus was on the semiconducting properties and anisotropic shape of the rods that promotes liquid crystal formation.

In the case of hybrid particles with polymer shells, it is a logical choice to apply the knowledge gained about polypeptides to functional materials. Early studies of this kind of system were conducted more than 30 years ago and the area has steadily progressed since then.[153, 154] The writer's home group has worked extensively with various polypeptides covalently attached to surfaces.[29, 71, 72, 155-157] A variety of fields have taken advantage of polypeptide hybrid particles. For instance, biotechnology is enhanced by particles that show promise for drug encapsulation by the polypeptide shell or for molecular imaging.[59, 158-160] Sensors are another popular application due to the helix to coil transition initiated by temperature and pH changes.[161] The ordered structures polypeptides can form are of interest in this dissertation and the phase behavior of silica-polypeptide hybrid particles is explored.

1.5 References

1.   Shaw, D. J., *Introduction to Colloid and Surface Chemistry*. Elsevier Science Ltd.: Burlington, MA, 1992.

2. Seebergh, J. E.; Berg, J. C. Depletion flocculation of aqueous, electrosterically-stabilized latex dispersions. *Langmuir* 1994, 10, (2), 454-463.

3. Spillmann, C. M.; Naciri, J.; Wahl, K. J.; Garner, Y. H.; Chen, M.-S.; Ratna, B. R. Role of Surfactant in the Stability of Liquid Crystal-Based Nanocolloids. *Langmuir* 2009, 25, (4), 2419-2426.

4. Elghanian, R.; Storhoff, J. J.; Mucic, R. C.; Letsinger, R. L.; Mirkin, C. A. Selective Colorimetric Detection of Polynucleotides Based on the Distance-Dependent Optical Properties of Gold Nanoparticles. *Science* 1997, 277, (5329), 1078-1081.

5. Gao, J.; Fu, J.; Lin, C.; Lin, J.; Han, Y.; Yu, X.; Pan, C. Formation and Photoluminescence of Silver Nanoparticles Stabilized by a Two-Armed Polymer with a Crown Ether Core. *Langmuir* 2004, 20, (22), 9775-9779.

6. Okubo, M.; Fujibayashi, T.; Terada, A. Synthesis of micron-sized, monodisperse polymer particles of disc-like and polyhedral shapes by seeded dispersion polymerization. *Colloid Polym Sci* 2005, 283, (7), 793-798.

7. Rolland, J. P.; Maynor, B. W.; Euliss, L. E.; Exner, A. E.; Denison, G. M.; DeSimone, J. M. Direct Fabrication and Harvesting of Monodisperse, Shape-Specific Nanobiomaterials. *Journal of the American Chemical Society* 2005, 127, (28), 10096-10100.

8. Merkel, T. J.; Herlihy, K. P.; Nunes, J.; Orgel, R. M.; Rolland, J. P.; DeSimone, J. M. Scalable, Shape-Specific, Top-Down Fabrication Methods for the Synthesis of Engineered Colloidal Particles. *Langmuir* 2009, 26, (16), 13086-13096.

9. Kuijk, A.; van Blaaderen, A.; Imhof, A. Synthesis of Monodisperse, Rodlike Silica Colloids with Tunable Aspect Ratio. *Journal of the American Chemical Society* 2011, 133, (8), 2346-2349.

10. McGeary, R. K. Mechanical Packing of Spherical Particles. *Journal of the American Ceramic Society* 1961, 44, (10), 513-522.

11. Jones, J. B.; Sanders, J. V.; Segnit, E. R. Structure of Opal. *Nature* 1964, 204, (4962), 990-991.

12. Arpin, K. A.; Mihi, A.; Johnson, H. T.; Baca, A. J.; Rogers, J. A.; Lewis, J. A.; Braun, P. V. Multidimensional Architectures for Functional Optical Devices. *Advanced Materials* 2010, 22, (10), 1084-1101.

13. Zhang, J.; Sun, Z.; Yang, B. Self-assembly of photonic crystals from polymer colloids. *Current Opinion in Colloid & Interface Science* 2009, 14, (2), 103-114.

14. Cush, R. C.; Russo, P. S. Self-Diffusion of a Rodlike Virus in the Isotropic Phase†. *Macromolecules* 2002, 35, (23), 8659-8662.

15. Gögelein, C.; Tuinier, R. Phase behaviour of a dispersion of charge-stabilised colloidal spheres with added non-adsorbing interacting polymer chains. *The European Physical Journal E: Soft Matter and Biological Physics* 2008, 27, (2), 171-184.

16. Zhou, J.; van Duijneveldt, J. S.; Vincent, B. The Phase Behavior of Dispersions of Silica Particles in Mixtures of Polystyrene and Dimethylformamide. *Langmuir* 2010.

17. Creighton, T. E., *Proteins: structures and molecular properties*. W.H. Freeman and Company: New York, NY, 1992.

18. Cochran, W.; Crick, F. Evidence for the Pauling-Corey α-Helix in Synthetic Polypeptides. *Nature* 1952, 169, 234-235.

19. Corey, R. B.; Pauling, L. Fundamental dimensions of polypeptide chains. *Proceedings of the Royal Society of London. Series B-Biological Sciences* 1953, 141, (902), 10-20.

20. Pauling, L.; Corey, R. B.; Branson, H. R. The structure of proteins: two hydrogen-bonded helical configurations of the polypeptide chain. *Proceedings of the National Academy of Sciences* 1951, 37, (4), 205-211.

21. Toniolo, C.; Polese, A.; Formaggio, F.; Crisma, M.; Kamphuis, J. Circular Dichroism Spectrum of a Peptide 3-10-Helix. *Journal of the American Chemical Society* 1996, 118, (11), 2744-2745.

22. Papadopoulos, P.; Floudas, G.; Klok, H. A.; Schnell, I.; Pakula, T. Self-Assembly and Dynamics of Poly(γ-benzyl-L-glutamate) Peptides. *Biomacromolecules* 2003, 5, (1), 81-91.

23. Pauling, L.; Corey, R. B. The pleated sheet, a new layer configuration of polypeptide chains. *Proceedings of the National Academy of Sciences of the United States of America* 1951, 37, (5), 251.

24. Pauling, L.; Corey, R. B. Configurations of polypeptide chains with favored orientations around single bonds: two new pleated sheets. *Proceedings of the National Academy of Sciences of the United States of America* 1951, 37, (11), 729.

25. Zimm, B. H.; Bragg, J. K. Theory of the Phase Transition between Helix and Random Coil in Polypeptide Chains. *The Journal of Chemical Physics* 1959, 31, (2), 526-535.

26. Gruenewald, B.; Nicola, C. U.; Lustig, A.; Schwarz, G.; Klump, H. Kinetics of the helix-coil transition of a polypeptide with non-ionic side groups, derived from ultrasonic relaxation measurements. *Biophysical Chemistry* 1979, 9, (2), 137-147.

27. Buhot, A.; Halperin, A. Extension Behavior of Helicogenic Polypeptides. *Macromolecules* 2002, 35, (8), 3238-3252.

28. Aravinda, S.; Datta, S.; Shamala, N.; Balaram, P. Hydrogen-Bond Lengths in Polypeptide Helices: No Evidence for Short Hydrogen Bonds. *Angewandte Chemie* 2004, 116, (48), 6896-6899.

29. Balamurugan, S. S.; Soto-Cantu, E.; Cueto, R.; Russo, P. S. Preparation of Organosoluble Silica-Polypeptide Particles by "Click" Chemistry. *Macromolecules* 2010, 43, (1), 62-70.

30. Balik, C. M.; Hopfinger, A. J. Quantization of the solvent effect on the adsorption of pol(γ-benzyl-L-glutamate). *Journal of Colloid and Interface Science* 1978, 67, (1), 118-126.

31. Martínez-Barbosa, M. E.; Bouteiller, L.; Cammas-Marion, S.; Montembault, V.; Fontaine, L.; Ponchel, G. Synthesis and ITC characterization of novel nanoparticles constituted by poly(γ-benzyl-L-glutamate)-β-cyclodextrin. *Journal of Molecular Recognition* 2008, 21, (3), 169-178.

32. Barbosa, M. E. M.; Montembault, V.; Cammas-Marion, S.; Ponchel, G.; Fontaine, L. Synthesis and characterization of novel poly(γ-benzyl-L-glutamate) derivatives tailored for the preparation of nanoparticles of pharmaceutical interest. *Polymer International* 2007, 56, (3), 317-324.

33. Bellomo, E. G.; Davidson, P.; Imperor-Clerc, M.; Deming, T. J. Aqueous Cholesteric Liquid Crystals Using Uncharged Rodlike Polypeptides. *Journal of the American Chemical Society* 2004, 126, (29), 9101-9105.

34. Block, H., *Poly(γ-benzyl-L-glutamate) and other glutamic acid containing polymers*. Gordon and Breach: New York, 1983.

35. Bu, Z.; Russo, P. S.; Tipton, D. L.; Negulescu, I. I. Self-Diffusion of Rodlike Polymers in Isotropic Solutions. *Macromolecules* 1994, 27, (23), 6871-6882.

36. Champion, J. V.; Nicholas, J. W. The infrared electric dichroism of poly-γ-benzyl-L-glutamate solutions. *Chemical Physics Letters* 1972, 14, (5), 573-576.

37. Chang, Y.-C.; Frank, C. W. Grafting of Poly(γ-benzyl-L-glutamate) on Chemically Modified Silicon Oxide Surfaces. *Langmuir* 1996, 12, (24), 5824-5829.

38. Doty, P.; Yang, J. T. Polypeptides. VII. Poly-γ-benzyl-L-glutamate: The helix-coil transition in solution. *Journal of the American Chemical Society* 1956, 78, (2), 498-500.

39.   Ginzburg, B. M.; Shepelevskii, A. A. Construction Of The Full Phase Diagram For The System Of Poly(γ-benzyl-L-glutamate)/dimethylformamide On The Basis Of The Complex Of Literature Data. *Journal of Macromolecular Science, Part B: Physics* 2003, 42, (1), 1 - 56.

40.   Gitsas, A.; Floudas, G.; Mondeshki, M.; Lieberwirth, I.; Spiess, H. W.; Iatrou, H.; Hadjichristidis, N.; Hirao, A. Hierarchical Self-Assembly and Dynamics of a Miktoarm Star chimera Composed of Poly(γ-benzyl-L-glutamate), Polystyrene, and Polyisoprene. *Macromolecules* 2010, 43, (4), 1874-1881.

41.   Guoquan Zhu, F. W., Zhen Ding, Yuying Liu, Qiaochun Gao. Aggregation behavior of poly(ethylene glycol)-*block*-poly(γ-benzyl-*L*-glutamate)-*graft*-poly(ethylene glycol) colpolymer and its blends with Poly(γ-benzyl-L-glutamate homopolymer in mixed solvents. *Journal of Macromolecular Science, Part A: Pure and Applied Chemistry* 2010, 47, 1006-1011.

42.   Hartmann, L.; Kremer, F.; Kratzmuller, T.; Braun, H. G. Molecular dynamics of grafted PBLG in the swollen and dried state. *Dielectrics and Electrical Insulation, IEEE Transactions on* 2001, 8, (3), 390-394.

43.   Jamil, T.; Russo, P. S. Dynamic light scattering from a semiflexible polymer at very low concentrations. *J. Chem. Phys.* 1992, 97, (4), 2777-2782.

44.   Jaworek, T.; Neher, D.; Wegner, G.; Wieringa, R. H.; Schouten, A. J. Electromechanical Properties of an Ultrathin Layer of Directionally Aligned Helical Polypeptides. *Science* 1998, 279, (5347), 57-60.

45.   Kishi, R.; Sisido, M.; Tazuke, S. Liquid-crystalline polymer gels. 2. Anisotropic swelling of poly(γ-benzyl-L-glutamate) gel crosslinked under a magnetic field. *Macromolecules* 1990, 23, (16), 3868-3870.

46.   Kiss, G.; Porter, R. S. Rheology of concentrated solutions of helical polypeptides. *Journal of Polymer Science: Polymer Physics Edition* 1980, 18, (2), 361-388.

47.   Lee, S.-D.; Meyer, R. B. The growth of highly ordered textures in planar poly(γ-benzyl-L-glutamate) liquid crystals. *Liquid Crystals* 1990, 7, (3), 451 - 455.

48.   Lin, J.; Abe, A.; Furuya, H.; Okamoto, S. Liquid Crystal Formation Coupled with the Coil-Helix Transition in the Ternary System Poly(γ-benzyl-L-glutamate)/Dichloroacetic Acid/Dichloroethane. *Macromolecules* 1996, 29, (7), 2584-2589.

49.   Liu, D.; Li, Y.; Deng, J.; Yang, W. Synthesis and characterization of magnetic Fe3O4-silica-poly(γ-benzyl-L-glutamate) composite microspheres. *Reactive and Functional Polymers* 2011, 71, (10), 1040-1044.

50. Ludwigs, S.; Krausch, G.; Reiter, G.; Losik, M.; Antonietti, M.; Schlaad, H. Structure Formation of Polystyrene-block-poly(γ-benzyl-L-glutamate) in Thin Films. *Macromolecules* 2005, 38, (18), 7532-7535.

51. Machida, S.; Urano, T. I.; Sano, K.; Kawata, Y.; Sunohara, K.; Sasaki, H.; Yoshiki, M.; Mori, Y. A Chiral Director Field in the Nematic Liquid Crystal Phase Induced by a Poly(γ-benzyl-L-glutamate) Chemical Reaction Alignment Film. *Langmuir* 1995, 11, (12), 4838-4843.

52. Martínez-Barbosa, M. E.; Cammas-Marion, S.; Bouteiller, L.; Vauthier, C.; Ponchel, G. PEGylated Degradable Composite Nanoparticles Based on Mixtures of PEG-b-Poly(γ-benzyl-L-glutamate) and Poly(γ-benzyl-L-glutamate). *Bioconjugate Chemistry* 2009, 20, (8), 1490-1496.

53. Miller, W. G.; Flory, P. J. Dimensions of polypeptide chains in helicogenic solvents. *Journal of Molecular Biology* 1966, 15, (1), 298-314.

54. Mori, Y.; Ookubo, N.; Hayakawa, R.; Wada, Y. Low-frequency and high-frequency relaxations in dynamic electric birefringence of poly(γ-benzyl-L-glutamate) in m-cresol. *Journal of Polymer Science: Polymer Physics Edition* 1982, 20, (11), 2111-2124.

55. Muroga, Y.; Nagasawa, M. On the flexibility of poly(γ-benzyl-L-glutamate) in helicogenic solvents. *Biopolymers* 1998, 45, (4), 281-288.

56. Neagu, E.; Neagu, R.; Daly, W. H.; Negulescu, I. I. Dielectric relaxations in thermotropic liquid crystalline polypeptides. *Electrical Insulation, IEEE Transactions on* 1993, 28, (1), 122-127.

57. Nguyen, L.-T. T.; Musser, A. J.; Vorenkamp, E. J.; Polushkin, E.; ten Brinke, G.; Schouten, A. J. Annealing-Induced Changes in Double-Brush Langmuir-Blodgett Films of α-Helical Diblock Copolypeptides. *Langmuir* 2010, 26, (17), 14073-14080.

58. Nguyen, L.-T. T.; Vorenkamp, E. J.; ten Brinke, G.; Schouten, A. J. Dipping-Induced Azimuthal Helix Orientation in Langmuir-Blodgett Monolayers of α-Helical Amphiphilic Diblock Copolypeptides. *Langmuir* 2010, 26, (13), 11018-11024.

59. Özcan, İ.; Bouchemal, K.; Segura-Sánchez, F.; Özer, Ö.; Güneri, T.; Ponchel, G. Synthesis and characterization of surface-modified PBLG nanoparticles for bone targeting: In vitro and in vivo evaluations. *Journal of Pharmaceutical Sciences* 2011, 100, (11), 4877-4887.

60. Poche, D. S.; Daly, W. H.; Russo, P. S. Synthesis and Some Solution Properties of Poly(γ-stearyl-α,L-glutamate). *Macromolecules* 1995, 28, (20), 6745-6753.

61. Robinson, C. Liquid-crystalline structures in solutions of a polypeptide. *Transactions of the Faraday Society* 1956, 52, 571-592.

62. Robinson, C.; Ward, J. C.; Beevers, R. B. Liquid crystalline structure in polypeptide solutions. Part 2. *Discussions of the Faraday Society* 1958, 25, 29-42.

63. Russo, P. S.; Baylis, M.; Bu, Z.; Stryjewski, W.; Doucet, G.; Temyanko, E.; Tipton, D. Self-diffusion of a semiflexible polymer measured across the lyotropic liquid-crystalline-phase. *Journal of Chemical Physics* 1999, 111, (4), 1746.

64. Russo, P. S.; Miller, W. G. On the nature of the poly(γ-benzyl-L-glutamate)-dimethylformamide "complex phase". *Macromolecules* 1984, 17, (7), 1324-1331.

65. Russo, P. S.; Miller, W. G. Coexistence of liquid crystalline phases in poly(γ-benzyl-α,L-glutamate)-dimethylformamide. *Macromolecules* 1983, 16, (11), 1690-1693.

66. Schmidt, A.; Lehmann, S.; Georgelin, M.; Katana, G.; Mathauer, K.; Kremer, F.; Schmidt-Rohr, K.; Boeffel, C.; Wegner, G.; Knoll, W. Molecular Dynamics of "Hairy Rod" Molecules in the Solid State: Poly(γ-methyl L-glutamate)-co-(γ-n-octadecyl-L-glutamate) in Solution-Cast Films. *Macromolecules* 1995, 28, (16), 5487-5497.

67. Schmidtke, S.; Russo, P.; Nakamatsu, J.; Buyuktanir, E.; Turfan, B.; Temyanko, E.; Negulescu, I. Thermoreversible Gelation of Isotropic and Liquid Crystalline Solutions of a "Sticky" Rodlike Polymer. *Macromolecules* 2000, 33, (12), 4427-4432.

68. Seo, M. S.; Jang, K.; Sohn, D.; Kang, P.; Choo, J. Side chain effect of rodlike polyglutamate, poly(γ-stearyl-α,L-glutamate). *Synthetic Metals* 2001, 117, (1-3), 293-295.

69. Sohn, D.; Kitaev, V.; Kumacheva, E. Self-Assembly of Substituted Polyglutamates on Solid Substrates: The Side-Chain Effect. *Langmuir* 1999, 15, (5), 1698-1702.

70. Sohn, D.; Yu, H.; Nakamatsu, J.; Russo, P. S.; Daly, W. H. Monolayer properties of a fuzzy rod polymer: Poly(γ-stearyl-α,L-glutamate). *Journal of Polymer Science Part B: Polymer Physics* 1996, 34, (17), 3025-3034.

71. Soto-Cantu, E. Synthesis and Surface Characterization of Silica-Polypeptide Composite Particles. Dissertation, Louisiana State University, Baton Rouge, 2008.

72. Soto-Cantu, E.; Turksen-Selcuk, S.; Qiu, J.; Zhou, Z.; Russo, P. S.; Henk, M. C. Silica−Polypeptide Composite Particles: Controlling Shell Growth. *Langmuir* 2010, 26, (19), 15604-15613.

73. Sridhar, C. G.; Hines, W. A.; Samulski, E. T. Polypeptide liquid crystals: Magnetic susceptibility, twist elastic constant, rotational viscosity coefficient, and poly-γ-benzyl-L-glutamate sidechain conformation. *The Journal of Chemical Physics* 1974, 61, (3), 947-953.

74. Tadmor, R.; Khalfin, R. L.; Cohen, Y. Reversible Gelation in Isotropic Solutions of the Helical Polypeptide Poly(γ-benzyl-L-glutamate): Kinetics and Formation Mechanism of the Fibrillar Network†. *Langmuir* 2002, 18, (19), 7146-7150.

75. Takashima, S. Dielectric behavior of helical polyamino acids in shear gradients. *The Journal of Physical Chemistry* 1970, 74, (25), 4446-4452.

76. Tang, H.; Zhang, D. General Route toward Side-Chain-Functionalized α-Helical Polypeptides. *Biomacromolecules* 2010, 11, (6), 1585-1592.

77. Tsai, M. L.; Chen, S. H.; Marshall, K. L.; Jacobs, S. D. Thermotropic and optical properties of chiral nematic polymers. *Int J Thermophys* 1990, 11, (1), 213-223.

78. Tschoegl, N. W.; Ferry, J. D. Dynamic Mechanical Properties of Poly-γ-benzyl-L-glutamate in a Helicogenic Solvent. *Journal of the American Chemical Society* 1964, 86, (8), 1474-1477.

79. Tsujita, Y.; Ojika, R.; Tsuzuki, K.; Takizawa, A.; Kinoshita, T. Circular dichroism of copoly(γ-stearyl-L-glutamate–γ-methyl-L-glutamate). *Journal of Polymer Science Part A: Polymer Chemistry* 1987, 25, (4), 1041-1048.

80. Watanabe, J.; Goto, M.; Nagase, T. Thermotropic polypeptides. 3. Investigation of cholesteric mesophase properties of poly(γ-benzyl-L-glutamate)-co-γ-dodecyl-L-glutamates) by circular dichroic measurements. *Macromolecules* 1987, 20, (2), 298-304.

81. Watanabe, J.; Ono, H.; Uematsu, I.; Abe, A. Thermotropic polypeptides. 2. Molecular packing and thermotropic behavior of poly(L-glutamates) with long n-alkyl side chains. *Macromolecules* 1985, 18, (11), 2141-2148.

82. Watanabe, J.; Takashina, Y. Columnar liquid crystals in polypeptides. 1. A columnar hexagonal liquid crystal observed in poly(γ-octadecyl-L-glutamate). *Macromolecules* 1991, 24, (11), 3423-3426.

83. Wieringa, R. H.; Siesling, E. A.; Werkman, P. J.; Angerman, H. J.; Vorenkamp, E. J.; Schouten, A. J. Surface Grafting of Poly(L-glutamates). 2. Helix Orientation. *Langmuir* 2001, 17, (21), 6485-6490.

84. Yamane, Y.; Kanekiyo, M.; Koizumi, S.; Zhao, C.; Kuroki, S.; Ando, I. Preparation and characterization of highly oriented poly(γ-benzyl L-glutamate) networks and gels with long channels with micrometer-scale diameters. *Journal of Applied Polymer Science* 2004, 92, (2), 1053-1060.

85. Yen, C.-C.; Edo, S.; Oka, H.; Tokita, M.; Watanabe, J. Phase Diagram for Solutions of alpha-Helical Poly(L-glutamate)s in m-Cresol Including Isotropic, Cholesteric, and Columnar Phases. *Macromolecules* 2008, 41, (10), 3727-3733.

86.   Yu, S. M.; Soto, C. M.; Tirrell, D. A. Nanometer-Scale Smectic Ordering of Genetically Engineered Rodlike Polymers: Synthesis and Characterization of Monodisperse Derivatives of Poly(γ-benzyl-α,L-glutamate). *Journal of the American Chemical Society* 2000, 122, (28), 6552-6559.

87.   Zhao, C.; Zhang, H.; Yamanobe, T.; Kuroki, S.; Ando, I. Diffusional Behavior of Solvent in Polypeptide Liquid Crystalline and Gel States with Highly Oriented Chains As Studied by NMR Spectroscopy. *Macromolecules* 1999, 32, (10), 3389-3395.

88.   Papadopoulos, P.; Floudas, G., Self-Assembly and the Associated Dynamics in PBLG-PEG-PBLG Triblock Copolymers. In *Nonlinear Dielectric Phenomena in Complex Liquids*, Rzoska, S.; Zhelezny, V., Eds. Springer Netherlands: 2005; Vol. 157, pp 327-334.

89.   Jabbari, E., *Biologically-responsive hybrid biomaterials: a reference for material scientists and bioengineers*. World Scientific Publishing Company Incorporated: 2010.

90.   Floudas, G.; Papadopoulos, P.; Klok, H. A.; Vandermeulen, G. W. M.; Rodriguez-Hernandez, J. Hierarchical Self-Assembly of Poly(γ-benzyl-L-glutamate)−Poly(ethylene glycol)−Poly(γ-benzyl-L-glutamate) Rod−Coil−Rod Triblock Copolymers. *Macromolecules* 2003, 36, (10), 3673-3683.

91.   Liu, J.; He, D.; Li, X.-z.; Gao, S.; Wu, H.; Liu, W.; Gao, X.; Zhou, T. γ-Polyglutamic acid (γ-PGA) produced by Bacillus amyloliquefaciens C06 promoting its colonization on fruit surface. *International Journal of Food Microbiology* 2010, 142, (1–2), 190-197.

92.   Kurosaki, T.; Kitahara, T.; Kawakami, S.; Higuchi, Y.; Yamaguchi, A.; Nakagawa, H.; Kodama, Y.; Hamamoto, T.; Hashida, M.; Sasaki, H. γ-Polyglutamic acid-coated vectors for effective and safe gene therapy. *Journal of controlled release* 2010, 142, (3), 404-410.

93.   Cheng, J.; Deming, T. J., Synthesis of Polypeptides by Ring-Opening Polymerization of α-Amino Acid N-Carboxyanhydrides. In *Peptide-Based Materials*, Springer: 2012; pp 1-26.

94.   Richards, E. E. G.; Dover, S. S. D., *An introduction to the physical properties of large molecules in solution*. CUP Archive: 1980; Vol. 3.

95.   Flory, P. J. Spatial configuration of macromolecular chains. *British Polymer Journal* 1976, 8, (1), 1-10.

96.   Doty, P.; Bradbury, J. H.; Holtzer, A. M. Polypeptides. IV. The Molecular Weight, Configuration and Association of Poly-γ-benzyl-L-glutamate in Various Solvents. *Journal of the American Chemical Society* 1956, 78, (5), 947-954.

97.   Hanlon, S. The Protonation of Poly-γ-benzyl-L-glutamate in Mixed Solvents Containing Dichloroacetic Acid. *Biochemistry* 1966, 5, (6), 2049-2061.

98.   Lifson, S.; Roig, A. On the Theory of Helix---Coil Transition in Polypeptides. *The Journal of Chemical Physics* 1961, 34, (6), 1963-1974.

99.   Watanabe, H.; Yoshioka, K.; Wada, A. Electrooptical and dielectric investigations on the conformation and the electrical properties of poly-γ-benzyl-L-glutamate in mixed solvents. *Biopolymers* 1964, 2, (1), 91-101.

100.   Seeling, J.; Schwarz, G. Concentration dependence of dielectric relaxation due to the helix–coil transition of poly(γ-benzyl-L-glutamate). *Biopolymers* 1969, 8, (3), 429-431.

101.   Ananthanarayanan, V. S.; Davenport, G.; Stimson, E. R.; Scheraga, H. A. Helix-Coil Transition in Mixed Solvents. II. Calorimetric Study of Poly(γ-benzyl L-glutamate) in Dichloroacetic Acid-Dichloroethane Mixtures. *Macromolecules* 1973, 6, (4), 559-563.

102.   Zimmermann, R.; Kratzmüller, T.; Erickson, D.; Li, D.; Braun, H.-G.; Werner, C. Ionic Strength-Dependent pK Shift in the Helix-Coil Transition of Grafted Poly(l-glutamic acid) Layers Analyzed by Electrokinetic and Ellipsometric Measurements. *Langmuir* 2004, 20, (6), 2369-2374.

103.   Hanlon, S.; Klotz, I. M. Protonation of Polypeptides in "Helix-Breaking" Solvents: Spectral and Optical-Rotatory Properties in Solutions Containing Strong Organic Acids. *Biochemistry* 1965, 4, (1), 37-48.

104.   Stake, M. A.; Klotz, I. M. Protonation of Polypeptides in Helix-Breaking Solvents. Electrical Conductance. *Biochemistry* 1966, 5, (5), 1726-1729.

105.   Wada, A. Dielectric Properties of Polypeptide Solutions. I. The Electric Dipole Moment of alpha Helix in Dioxane. *The Journal of Chemical Physics* 1958, 29, (3), 674-675.

106.   Adam, W.; Grimison, A.; Hoffmann, R.; Zuazaga de Ortiz, C. Hydrogen bonding in pyridine. *Journal of the American Chemical Society* 1968, 90, (6), 1509-1516.

107.   Block, H.; Hayes, E. F. Dielectric behaviour of stiff polymers in solution when subjected to high voltage gradients. *Transactions of the Faraday Society* 1970, 66, (0), 2512-2525.

108.   Tsuji, K.; Watanabe, H. Electro-optical investigation of the effect of space charge on molecular alignment in poly-γ-benzyl-L-glutamate solutions. *The Journal of Chemical Physics* 1977, 66, (3), 1343-1351.

109.   Tsuji, K.; Watanabe, H. Molecular association of polypeptides in concentrated solutions investigated by the electrooptical method: I. Poly-γ-benzyl-L-glutamate-dichloroethane system. *Journal of Colloid and Interface Science* 1977, 62, (1), 101-113.

110.   Watanabe, H.; Fukuda, Y.; Nakano, T. Molecular association of polypeptides in concentrated solutions investigated by the electrooptical method: II. Frequency-dependent electric birefringence of poly-γ-benzyl-L-glutamate (PBLG) solutions by pulsed altern current field with sufficient strength. *Journal of Colloid and Interface Science* 1985, 108, (2), 347-355.

111.   Panar, M.; Phillips, W. D. Magnetic ordering of poly (γ–benzyl L-glutamate) solutions. *Journal of the American Chemical Society* 1968, 90, (14), 3880-3882.

112.   Samulski, E. T.; Tobolsky, A. V. Some Unusual Properties of Poly(γ-benzyl-L-glutamate) Films Cast in Strong Magnetic Fields. *Macromolecules* 1968, 1, (6), 555-557.

113.   Doucet, G. J.; Russo, P. S. Self-Diffusion of a Semiflexible Polypeptide in a Magnetically Aligned Liquid Crystalline Phase. *Molecular Crystals and Liquid Crystals* 2013, 570, (1), 67-75.

114.   Schmidt, M. Combined integrated and dynamic light scattering by poly(γ-benzyl-L-glutamate) in a helocogenic solvent. *Macromolecules* 1984, 17, (4), 553-560.

115.   DeLong, L. M.; Russo, P. S. Thermodynamic and dynamic behavior of semiflexible polymers in the isotropic phase. *Macromolecules* 1991, 24, (23), 6139-6155.

116.   Aharoni, S. M. On entanglements of flexible and rodlike polymers. *Macromolecules* 1983, 16, (11), 1722-1728.

117.   Friedel, G. The mesomorphic states of matter. *Ann. Phys* 1922, 18, 273-474.

118.   Chandrasekhar, S., *Liquid Crystals*. 2nd ed.; Press Syndicate of the University of Cambridge: New York, NY, 1992.

119.   DuPre, D. B.; Duke, R. W. Temperature, concentration, and molecular weight dependence of the twist elastic constant of cholesteric poly-γ-benzyl-L-glutamate. *The Journal of Chemical Physics* 1975, 63, (1), 143-148.

120.   Dogic, Z.; Fraden, S. Cholesteric Phase in Virus Suspensions. *Langmuir* 2000, 16, (20), 7820-7824.

121.   Grelet, E.; Fraden, S. What Is the Origin of Chirality in the Cholesteric Phase of Virus Suspensions? *Physical Review Letters* 2003, 90, (19), 198302.

122.   Choi, S. S.; Morris, S. M.; Huck, W. T. S.; Coles, H. J. Electrically Tuneable Liquid Crystal Photonic Bandgaps. *Advanced Materials* 2009, 21, (38-39), 3915-3918.

123.   De Gennes, P. G.; Prost, J., *The Physics of Liquid Crystals*. Oxford University Press, Inc.: New York, NY, 1993.

124. Hrozhyk, U. A.; Serak, S. V.; Tabiryan, N. V.; White, T. J.; Bunning, T. J. Optically switchable, rapidly relaxing cholesteric liquid crystal reflectors. *Opt. Express* 2010, 18, (9), 9651-9657.

125. Chilaya, G.; Chanishvili, A.; Petriashvili, G.; Barberi, R.; Bartolino, R.; De Santo, M.; Matranga, M.; Collings, P. Light control of cholesteric liquid crystals using azoxy-based host materials. *Molecular Crystals and Liquid Crystals* 2006, 453, (1), 123-140.

126. Fang, G.; Shi, Y.; Maclennan, J. E.; Clark, N. A.; Farrow, M. J.; Walba, D. M. Photo-Reversible Liquid Crystal Alignment using Azobenzene-Based Self-Assembled Monolayers: Comparison of the Bare Monolayer and Liquid Crystal Reorientation Dynamics. *Langmuir* 2010, 26, (22), 17482-17488.

127. Uematsu, I.; Uematsu, Y., Polypeptide liquid crystals. In *Liquid Crystal Polymers I*, 1984; pp 37-73.

128. Robinson, C. Liquid-crystalline structures in polypeptide solutions. *Tetrahedron* 1961, 13, (1-3), 219-234.

129. Ao, G.; Nepal, D.; Aono, M.; Davis, V. A. Cholesteric and Nematic Liquid Crystalline Phase Behavior of Double-Stranded DNA Stabilized Single-Walled Carbon Nanotube Dispersions. *ACS Nano* 2011, 5, (2), 1450-1458.

130. Maret, G.; Milas, M.; Rinaudo, M. Cholesteric order in aqueous solutions of the polysaccharide Xanthan. *Polymer Bulletin* 1981, 4, (5), 291-297.

131. Suto, S.; Kimura, S.; Karasawa, M. Determination of the order parameter in cholesteric liquid crystalline phase cellulose derivatives solutions by refractometry. *Journal of Applied Polymer Science* 1987, 33, (8), 3019-3036.

132. Flory, P. J. Statistical Thermodynamics of Mixtures of Rodlike Particles. 5. Mixtures with Random Coils. *Macromolecules* 1978, 11, (6), 1138-1141.

133. Flory, P., Molecular theory of liquid crystals. In *Liquid Crystal Polymers I*, 1984; pp 1-36.

134. Onsager, L. The Effects of Shape on the Interaction of Colloidal Particles. *Annals of the New York Academy of Sciences* 1949, 51, (Molecular Interaction), 627-659.

135. Dogic, Z.; Fraden, S., Phase Behavior of Rod-Like Viruses and Virus-Sphere Mixtures. In *Soft Matter: Complex Colloidal Suspensions*, Wiley-VCH: 2006; Vol. 2, pp 1-78.

136. Elliott, A.; Ambrose, E. J. Evidence of chain folding in polypeptides and proteins. *Discussions of the Faraday Society* 1950, 9, (0), 246-251.

137. Toriumi, H.; Yahagi, K.; Uematsu, I.; Uematsu, Y. Cholesteric Structure of Lyotropic Poly (γ-benzyl-L-glutamate) Liquid Crystals. *Molecular Crystals and Liquid Crystals* 1983, 94, (3), 267-284.

138. Samulski, E.; Tobolsky, A. Distorted α-helix for poly (γ-benzyl-L-glutamate) in the nematic solid stale. *Biopolymers* 1971, 10, (6), 1013-1019.

139. Wagner, N. J.; Walker, L. M. Determination of the texture viscosity and elasticity of a nematic PBLG/d-DMF solution through magnetic field alignment. *Macromolecules* 1994, 27, (21), 5979-5986.

140. Squire, I.; Elliott, A. Liquid Crystalline Phases of Poly-γ-Benzyl-Glutamate in Solution. *Molecular Crystals and Liquid Crystals* 1969, 7, (1), 457-468.

141. Wessels, P. P. F.; Mulder, B. M. Entropy-induced microphase separation in hard diblock copolymers. *Physical Review E* 2004, 70, (3), 031503.

142. Lioubashevski, O.; Chegel, V. I.; Patolsky, F.; Katz, E.; Willner, I. Enzyme-Catalyzed Bio-Pumping of Electrons into Au-Nanoparticles: A Surface Plasmon Resonance and Electrochemical Study. *Journal of the American Chemical Society* 2004, 126, (22), 7133-7143.

143. Xiangbing, Z.; Feng, L.; Alan, G. F.; Goran, U.; Liliana, C.; Georg, H. M.; Macdonald, J. E. 3D Ordered Gold Strings by Coating Nanoparticles with Mesogens. *Advanced Materials* 2009, 21, (17), 1746-1750.

144. Li, D.; He, Q.; Li, J. Smart core/shell nanocomposites: Intelligent polymers modified gold nanoparticles. *Advances in Colloid and Interface Science* 2009, 149, (1-2), 28-38.

145. Lei, Z.; Li, N.; Lin, L.; Jia, Y.; Pang, X.; Ren, N. Formation of Ag nanoparticles within the thermosensitive hairy hybrid particles. *Materials Letters* 2009, 63, (12), 975-977.

146. Chen, C.-C.; Lin, D.-J.; Don, T.-M.; Huang, F.-H.; Cheng, L.-P. Preparation of organic-inorganic nano-composites for antireflection coatings. *Journal of Non-Crystalline Solids* 2008, 354, (32), 3828-3835.

147. Zalzberg, L.; Avnir, D. Biocompatible hybrid particles of poly(L-lactic acid)@silica. *Journal of Sol-Gel Science and Technology* 2008, 48, (1), 47-50.

148. Kumar, S.; Pal, S. K.; Kumar, P. S.; Lakshminarayanan, V. Novel Conducting nanocomposites: synthesis of triphenylene-covered gold nanoparticles and their insertion into a columnar matrix. *Soft Matter* 2007, 3, 896-900.

149. Malenovska, M.; Litschauer, M.; Neouze, M.-A.; Schubert, U.; Peled, A.; Lellouche, J.-P. Multi-component hybrid inorganic-organic-inorganic particles with various metal oxide outer shells. *Journal of Organometallic Chemistry* 2009, 694, (7-8), 1076-1080.

150. Liu, G.; Wang, H.; Yang, X.; Li, L. Synthesis of tri-layer hybrid microspheres with magnetic core and functional polymer shell. *European Polymer Journal* 2009, 45, (7), 2023-2032.

151. Nagao, D.; Yokoyama, M.; Saeki, S.; Kobayashi, Y.; Konno, M. Preparation of composite particles with magnetic silica core and fluorescent polymer shell. *Colloid & Polymer Science* 2008, 286, (8), 959-964.

152. Zorn, M.; Meuer, S.; Tahir, M. N.; Khalavka, Y.; Sönnichsen, C.; Tremel, W.; Zentel, R. Liquid crystalline phases from polymer functionalised semiconducting nanorods. *Journal of Materials Chemistry* 2008, 18, 3050-3058.

153. Dietz, V. E.; Fery, N.; Hamann, K. Polyreaktionen an pigmentoberflächen. IV. Mitteilung: Polymerisation von n-carboxy-α-aminosäureanhydriden auf der oberfläche von siliciumdioxid. *Die Angewandte Makromolekulare Chemie* 1974, 35, (1), 115-129.

154. Laible, R.; Hamann, K. Formation of chemically bound polymer layers on oxide surfaces and their role in colloidal stability. *Advances in Colloid and Interface Science* 1980, 13, (1–2), 65-99.

155. Qiu, J. Properties of Silica-Polypeptide Composite Particles. Dissertation, Louisiana State University, Baton Rouge, 2007.

156. Fong, B.; Turksen, S.; Russo, P. S.; Stryjewski, W. Colloidal Crystals of Silica-Homopolypeptide Composite Particles. *Langmuir* 2004, 20, (1), 266-269.

157. Turksen, S. Synthesis and Characterization of Superparamagnetic Silica-Homopolypeptide Composite Particles. Louisiana State University, Baton Rouge, LA, 2004.

158. Atmaja, B.; Lui, B. H.; Hu, Y.; Beck, S. E.; Frank, C. W.; Cochran, J. R. Targeting of Cancer Cells Using Quantum Dot–Polypeptide Hybrid Assemblies That Function as Molecular Imaging Agents and Carrier Systems. *Advanced Functional Materials* 2010, 20, (23), 4091-4097.

159. Osada, K.; Kataoka, K. Drug and gene delivery based on supramolecular assembly of PEG-polypeptide hybrid block copolymers. In *Peptide Hybrid Polymers*, Springer: 2006; pp 113-153.

160. Michalet, X.; Pinaud, F. F.; Bentolila, L. A.; Tsay, J. M.; Doose, S.; Li, J. J.; Iyer, G.; Weiss, S. In *Peptide-coated semiconductor nanocrystals for biomedical applications*, Biomedical Optics 2005, 57-68.

161. Knoop, R. J. I.; de Geus, M.; Habraken, G. J. M.; Koning, C. E.; Menzel, H.; Heise, A. Stimuli Responsive Peptide Conjugated Polymer Nanoparticles. *Macromolecules* 2010, 43, (9), 4126-4132.

CHAPTER 2. ANALYTICAL METHODS

2.1 Dynamic Light Scattering (DLS)

Berne and Pecora describe electromagnetic radiation as "one of the most important probes of the structure and dynamics of matter."[1] Proof of this idea can be seen in the diverse array of techniques and instruments based on irradiation of a material with various wavelengths of light. Dynamic light scattering employs coherent light in the visible range (400-700 nm wavelengths) to measure the size of polymers and particles and their distribution of sizes. DLS was previously named for specific components of the process, photon correlation spectroscopy (PCS) emphasized the statistical correlation of scattered light, while quasi-elastic light scattering (QELS) described the type of scattering that occurs in the process. Light scattering is still the most accurate description of the experiment, but now the word dynamic is used as a descriptor to distinguish it from static light scattering (SLS).

DLS is a nondestructive method for measuring size with one of its biggest advantages being the ability to study objects in solution. Other methods, such as transmission electron microscopy (TEM), require items to be dry and possibly stained for color, which can severely alter a polymer from its original state. Harsh electron or X-ray beams may also deteriorate the sample to the point where it can be analyzed only once making experiments more costly to repeat.

Polymers and colloidal particles are capable of being studied in almost any solvent, or even combinations of solvents, as long as the refractive indices and viscosities are known. Beyond particle sizing, the effect of temperature changes can be explored, which may provide insight into properties of thermally responsive polymers.[2] Aggregation behavior is measurable by DLS in terms of finding the critical micelle concentration for block copolymers[3] or determining

the bundling characteristics of a filament.[4] Information can also be gained from core-shell particles by refractive index matching of the solvent to either the core or the shell of the particles to examine their behavior. Intentionally aggregating particles through depleting interactions has been studied by DLS allowing the generation of phase behavior diagrams.[5]

A prerequisite of a DLS experiment to measure size is that measurements are done on dilute solutions. The governing principles of this technique are derived on the basis of the measurement of many individual scatterers. Deviation from this assumption by having multiple scatterers, e.g. a concentrated solution, decreases the accuracy of the numbers obtained. There are proposed methods of dealing with this case such as Diffusing Wave Spectroscopy (DWS), which probes particle displacement to decipher viscoelastic properties of the system,[6, 7] and 3-D cross correlation detection which conducts two light scattering experiments of the same sample simultaneously.[8, 9]

There are two modes in which DLS measurements are done, homodyne or heterodyne. Homodyne scattering is most common and is based on the detection of scattered light solely from the sample, while heterodyne detection incorporates a portion of the unscattered beam. The experimental setup for the latter differs from that of homodyne detection, which is the primary detection method used in this research, by the addition of optics or other elements that mix a portion of the laser beam with the light scattered by the sample.

The light source for DLS is usually a laser tuned to a narrow wavelength range. Before and after the sample are focusing lenses that direct light to the sample cell and from the cell to the detector. The sample is immersed in a toluene bath for refractive index matching of the glass (n_D ~1.5) to reduce reflections that occur when the laser beam enters or leaves the cell; these reflections would interfere with detection of the scattered light. Both the sample and toluene are

encased in a jacket capable of controlling the temperature of the sample, which factors into the thermal energy portion of the equation required to calculate size. Once scattered light leaves the sample, it passes through an aperture and pinhole which serve to spatially coordinate the scattered light and block light from other angles. The detector receives the scattered light and the fluctuating signal is passed on to the correlator (Figure 2.1).
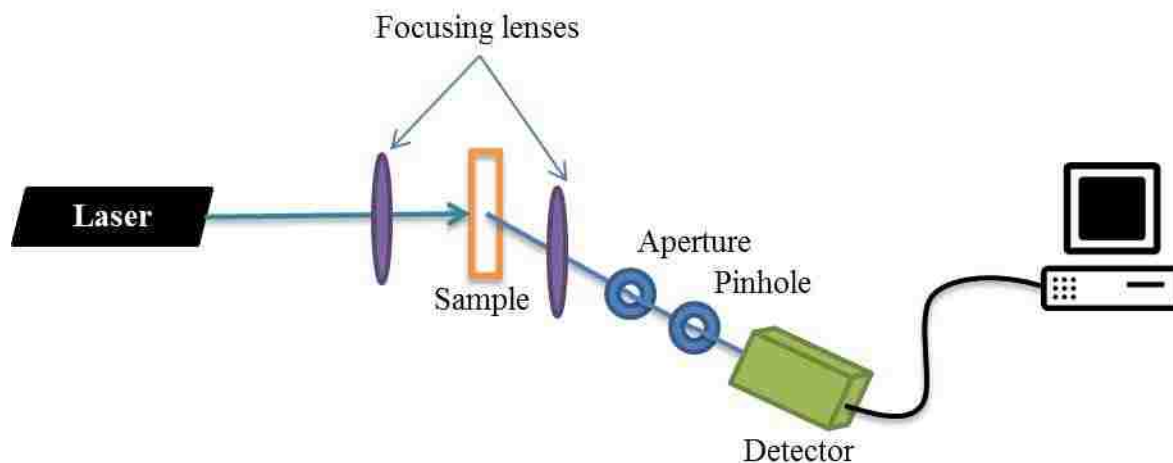
Figure 2.1 Typical setup for dynamic light scattering instrumentation.

The detector for most of the experiments reported in this dissertation was equipped with two photomultiplier tubes arranged in pseudo cross-correlation mode. True cross-correlation detection requires the use of two detectors and the individual signals are combined in an effort to minimize the effects of multiple scattering or afterpulsing where additional pulses of light follow the original pulse of light sent to the detector.[10, 11] In pseudo cross correlation, the light received by the detector is divided with a beam splitter which passes one beam on to the first photodiode and the other beam is reflected onto the second photodiode.[12] This configuration can defeat afterpulsing but not multiple scattering. To acquire scattered signal at a range of angles the detector is attached to a goniometer and rotated manually. Automated systems exist, but an

optimal situation would be the simultaneous collection of scattering at multiple angles as seen in other instruments or as proposed by Bantchev, *et al.*[13]

The scattering process occurs when the light interacts with the electrons in the particle by forcing them to resonate with the same frequency as the laser light. As particles move by Brownian motion throughout the sample, the wavelength and/or intensity of the light changes due to interference from other particles that are also emitting light. The temporal fluctuations in intensity of this collective emission of light arriving at the detector are correlated. The output is a correlation function which expresses the decay rate of the signal as a function of time.

Fluctuations in scattering from the sample actually occur in the electric field (E), and the normalized field-field correlation function is represented by

$$g^{(1)}(t) = \frac{< E(0)E^*(t) >}{< E(0)E^*(0) >} \qquad (2.1)$$

where $E(0)$ is the initial electric field and $E(t)$ is the electric field at some later time, t. The immeasurability of the electric field requires the statistical averaging of intensity fluctuations over time instead. The normalized intensity-intensity time correlation function is given by Equation 2.1 where, following the above convention, $I(0)$ is the initial intensity and $I(t)$ corresponds to the intensity at time, t. The initial intensity $I(0)$ will always be greater than $I(t)$ and the correlation function will decay as time increases.

$$g^{(2)}(t) = \frac{< I(0)I(t) >}{< I(0)^2 >} \qquad (2.2)$$

A fundamental relationship in DLS that relates the square of the normalized electric field to the normalized intensity autocorrelation function is known as the Siegert relation (Equation 2.3). The parameter f is determined by instrument settings and ranges from zero to one, with one corresponding perfect coherence.[14]

$$g^{(2)}(t) = 1 + f[g^{(1)}(t)]^2 \qquad (2.3)$$

The electric field autocorrelation function contains information about the rate at which the correlation of intensity fluctuations decay and may be expressed as

$$g^{(1)}(t) = \int_0^\infty A(\Gamma)e^{-\Gamma t}\, d\Gamma \qquad (2.4)$$

where $g^{(1)}$(t) is the Laplace transform of the decay rate distribution function A(Γ). For a dilute, monodisperse and optically isotropic dispersion the decay of the autocorrelation function is in the form of a single exponential, but for polydisperse and anisotropic systems additional terms are included where q is the scattering angle, D_i is the diffusion coefficient, and t is time.

$$g^{(1)}(q,t) = e^{-q^2 D_1 t} + e^{-q^2 D_2 t} + \cdots \qquad (2.5)$$

The diffusion coefficients obtained are not independent of concentration. Fundamentally, the assumption is that the particles are at infinite dilution and that neighbors are not interfering with the motion of the individual particle. The decay of the correlation function strongly corresponds to the long-range motion of the particles, the translational diffusion. As mentioned previously, for a monodisperse sample, the equation can be truncated to the first term and Γ is the decay rate and q defines the scattering vector where n is the refractive index of the solution, θ is the scattering angle and λ_0 is the wavelength of the incident beam.

$$\Gamma = q^2 D_t \qquad (2.6)$$

$$q = \frac{4\, n\, \pi}{\lambda_0} sin\frac{\theta}{2} \qquad (2.7)$$

Polydisperse samples exhibit a distribution of decay rates arising from the distribution of diffusion coefficients. This distribution is typically analyzed by the cumulant method, which fits ln $/g^{(1)}(t)/$ to a polynomial and the distribution of decay rates are characterized by their moments

that describe the distribution. The first cumulant describes the average decay rate, the second cumulant describes the variance and the third cumulant describes the skewness of the distribution.[15] Software used in the analysis of data is capable of generating up to third order cumulant fits (or even higher orders) and the common practice for data analysis in this dissertation is to use the first (or average) gamma of the 3-cumulant fit. Equation 2.8 is generated from the combination of the Taylor expansion of the cumulant-generating function with the correlation function. Linearizing the $g^{(1)}(t)$ by taking the natural log results in the following equation

$$ln|g^{(1)}(t)| = -\bar{\Gamma}t + \frac{\mu_2}{2!}t^2 + \frac{\mu_3}{3!}t^3 + \cdots \qquad (2.8)$$

which can be fitted directly to find the average gamma. The second coefficient used to find μ_2 is significant in that it corresponds to degree of polydispersity (PDI) in the sample.

Cumulant analysis becomes less accurate as samples become more polydisperse because a linear fit estimation is no longer valid. For a completely monodisperse system PDI is zero, but when PDI is greater than or equal to 0.3 Inverse Laplace Transform (ILT), which converts information in the frequency domain to a function in the time domain, becomes a more practical method of analysis.

In the early 1980s Stephen Provencher developed a program, written in FORTRAN, for inverting integral equations and the name CONTIN was given due to its ability to estimate continuous distributions that are consistent with the measured data.[16] CONTIN[17, 18] is an inverse Laplace transformation algorithm used to determine the decay rate distribution. CONTIN will generate a distribution of decay rates (Γ) which can then be converted to a diffusion coefficient depending on the scattering angle (Equation 2.6).

There is more than one method to define the size of a polymer. The radius of gyration, R_g, which is the average distance of any point in the polymer from the center of mass squared, is determined from static light scattering; while dynamic light scattering will provide a different measure based on the assumption that the polymer is accurately represented by a hard sphere. This hypothetical sphere correlates to the size of a hydrated polymer and the radius of the sphere is considered the hydrodynamic radius of the polymer. Stokes' equation for drag force f on a hard, spherical particle under laminar flow is given by

$$f = 6\pi\eta r \tag{2.9}$$

where η is the viscosity of the solvent and r is the radius of the sphere. Einstein relates this drag force to the diffusion of spheres in Brownian motion by

$$D = \frac{k_B T}{f} \tag{2.10}$$

where k_B is Boltzmann's constant, T is the temperature of the sample in Kelvin. Substitution of Equation (2.9) into Equation (2.10) yields the popular form of the Stokes-Einstein equation

$$R_{h,t} = \frac{k_B T}{6\pi\eta D_t} \tag{2.11}$$

where the subscript t specifies that the radius is derived from the translational diffusion coefficient.

2.2 Depolarized Dynamic Light Scattering (DDLS)

Depolarized Dynamic Light Scattering (DDLS) is a special application of light scattering that differs from polarized DLS by measuring an additional particle motion. As described above, DLS depends on translational motion, but depolarized DLS is sensitive to rotational motion as well. For spherical particles lacking optical anisotropy, rotational motion is inconsequential, but an optically anisotropic particle will scatter light differently depending on its orientation to the

incident beam. Changes in the orientation of the particle with respect to the incident beam result in changes in the scattered light as the particle tumbles about causing fluctuations in the emitted electric field and correspondingly the intensity of the detected light.[1] Similar to DLS these intensity fluctuations are correlated to determine the rotational diffusion coefficient of the particle.

The origin of the depolarized signal for anisotropic particles arises from the particle having two optical axes, one parallel and one perpendicular to the longest axis of symmetry. Incident light interacts with both axes and result in scattered light having components polarized in both the vertical and horizontal directions. The convention is to denote the vertical and horizontal directions with the letters V and H, respectively.[19] The scattered light polarization direction is listed first using an upper-case letter, with the incident light polarization following in lower-case. While laser light is generally assumed to be vertically polarized, a very small percent of the beam may not be which, for DDLS, may add noise to the scattered signal. To prevent this, a vertical polarizer is placed before the sample to ensure a single polarization enters the sample. The scattered light is also filtered using either a vertical polarizer to capture polarized signal or a horizontal polarizer to capture depolarized signal. If the depolarized signal is strong enough the scattered beam is referred to as unpolarized (denoted by the subscript U).
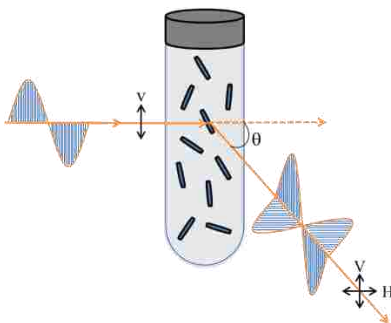
Figure 2.2 Schematic representation of depolarized light scattering in the V_V and H_V directions. Vertically polarized light enters the sample. Anisotropic particles depolarize the signal into waves whose electric fields oscillate parallel and perpendicular to the incident wave.

Carbon nanotubes,[20] rodlike polymers,[21-24] and dumbbell-shaped polymers[25] have all been characterized by DDLS, but depolarization of light is not restricted to anisotropic polymers. Solvents are also capable of depolarizing light based on the anisotropy of the molecule itself. For example, water and carbon tetrachloride depolarize light,[26, 27] but the polymers being measured will scatter more than the solvent, rendering its contribution negligible (assuming the refractive indices are not matched). Metallic nanoparticles are also included in the list of particles that can depolarize light.[28, 29] They are unique scatterers because they possess a dense electronic structure that responds strongly to the polarized incident light.

Synthesis of latex particles may result in close packing of polymer chains creating a partially crystalline particle capable of depolarizing light. Crystalline domains are often birefringent and the two refractive indices will effectively rotate light establishing a horizontal component. The overall shape of the particle need not be anisotropic as spherical, crystalline particles will produce a signal in the H_V configuration.[30, 31]

A benefit of DDLS and the measurement of rotational diffusion is that D_r is inversely proportional to R^3, a much stronger relationship than purely translational DLS, which correlates inversely as R. The mathematical developments are essentially the same as in polarized light scattering in the dilute regime;[32, 33] however, the decay rate is now expressed as

$$\Gamma_{H_V} = q^2 D_t + 6D_r \tag{2.12}$$

where D_r is the rotational diffusion coefficient. A plot of Γ vs. q^2 is linear with the slope corresponding to the translational diffusion and the intercept equals six times the rotational diffusion coefficient. Stokes-Einstein behavior is still valid in this case and leads to Equation (2.13).

$$R_{h,r} = \left(\frac{kT}{8\pi\eta_0 D_r}\right)^{1/3} \tag{2.13}$$

In addition to particle radius, a depolarization ratio ρ is reported which is the ratio of the intensity of vertically polarized signal to horizontally polarized signal. This dimensionless quantification allows for comparison of depolarization strength of one system to another. For an unpolarized light source scattering in the vertical and horizontal directions are additive and the depolarization ratio is expressed as

$$\rho_U = \frac{I_{H_V} + I_{H_H}}{I_{V_V} + I_{V_H}} \tag{2.14}$$

Commonly, the incident beam is vertically polarized due to the use of laser light and the incident horizontal components are reduced to zero leaving the final form as

$$\rho = \frac{I_H}{I_V} \tag{2.15}$$

and the subscript (V) is often dropped.

A subset of depolarized DLS is the case of zero-angle scattering. Usually applied to strongly scattering particles, this method eliminates the translational component and considers rotational diffusion exclusively.

$$\Gamma_{H_V} = 6D_R = \frac{3k_B T}{4\pi\eta R_h^3} \tag{2.16}$$

A benefit of this technique is enhanced resolution between particles of similar size, requiring only about 25% difference as opposed to the traditional DLS where the rule of thumb is a full 100% difference in size.[34, 35] Disadvantages are sensitivity to fluctuations in the laser output and low scattering intensity in comparison to the incident light that reaches the detector.[36]

2.3 Small and Wide Angle X-ray Scattering (SAXS and WAXS)

2.3.1 Introduction

Dynamic light scattering described above is used to size particles or measure fluctuations on a micron to nanometer scale. Increasing the q-range and thereby decreasing the observable size range is possible with Small and Wide Angle X-ray Scattering (SAXS and WAXS). These techniques are used to determine detailed information about the structure of a material or particle on the micrometer or nanometer scale. In some instances it is beneficial to use dynamic light scattering and X-ray scattering together for particle analysis as DLS requires an assumption of particle shape, while SAXS scattering patterns are a reflection of shape.[37, 38] The experimental concept is also similar to DLS as X-ray scattering originates from the interaction of the incident X-ray beam with the material. Oscillating electrons generate electromagnetic radiation which is coherent with the incident radiation, while the nucleus remains relatively stationary.

X-ray scattering has been applied to an array of materials: particles, fibers, micelles, polymers, films, etc.[31, 39-41] In this dissertation most of the samples measured are colloidal particles, polymers, or some combination of both in solution. For solution studies it is critical that there is sufficient electron density contrast between the solvent and the solute in order to have a measureable amount of scattering.[42, 43]

2.3.2 X-ray Scattering Experiment

All experiments in this dissertation were conducted using X-rays produced from synchrotron radiation. Generation of X-rays results when electrons travelling at relativistic speeds are accelerated in a circular orbit. Magnetic fields are applied to maintain the electron's speed and trajectory. Multiple wavelengths of X-rays are expelled from the ring in a direction tangential to its orbit. Beamlines are placed in position along these tangential directions and

monochromators are used to select a single wavelength.[44, 45] The energy of the X-rays produced are in the range of 5-10 keV, considered "hard" X-rays, and are used in crystallography, the medical field, or for security scanning applications; soft X-rays are absorbed by the air.

The X-ray beam is first passed through collimating pinholes. The first pinhole narrows the beam and intermediate pinholes are used to adjust beam size. The final pinhole often serves to select out parasitic scattering which results from X-rays interacting with the edges of the previous pinhole. Parasitic scattering is deleterious for a scattering experiment as it provides additional angles of incident beam resulting in a noisy scattered signal.[46] Care must be taken that pinholes are aligned concentrically to ensure maximum beam intensity and to reduce the possibility of scattering from the pinhole edge.
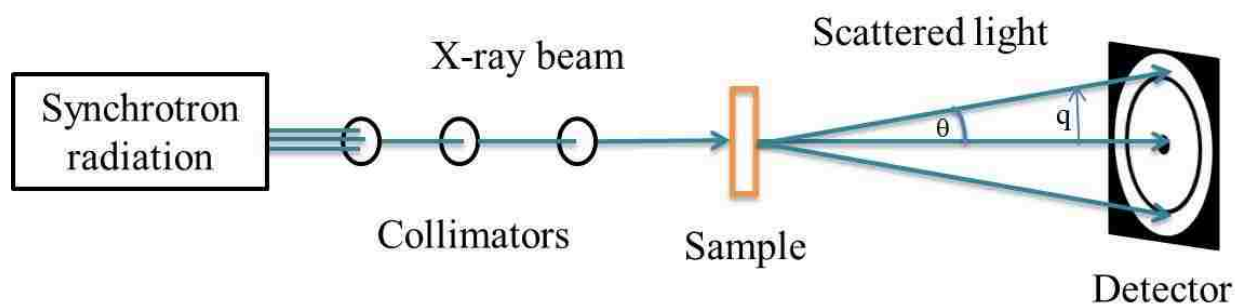
Figure 2.3 Schematic representation of SAXS setup. X-ray beam passes through collimators and is transmitted through the sample. Scattered X-rays are shown defining the angle theta and the vector *q*.

The sample is suspended in a dark chamber to prohibit interference from light (only important when film or plate detectors are used) and placed under vacuum to limit the amount of scattering from air. It is also possible to leave the sample in open air provided the gap is not large enough to absorb the scattered signal. The detector is equipped with a beamstop, which absorbs the incident beam. This protects the detector from excess photons and serves as a photodiode that

reads the photon count of the incident beam. The 2-D detector collects the scattered signal at a distance from the sample that defines the range of q-values.

2.4 Polarized Optical Microscopy (POM)

Entire books are devoted to the study of microscopy and polarized microscopy in particular.[47-49] Many laboratories that employ microscopes often have more than one available as there are many small variations and adaptations applied to this tool invented hundreds of years ago. A brief explanation of the type of microscopy conducted for this dissertation is included here.

Cross-polarized microscopy is used to view birefringent materials. The sample should be transparent for use in transmission mode as well as the substrate or cell in which the sample is placed. The optical arrangement of POM begins with a white light source, which passes through a condenser, which focuses the light, and on to a polarizer whose orientation is adjustable. The amount of light allowed through the sample is crucial for obtaining images that are not overly saturated or under illuminated. This optimal condition is referred to as Köhler illumination which provides a wide cone of light, enhancing the resolution of the image. Light transmitted through the sample passes through a second polarizer that is called an analyzer based on its position in the apparatus. The analyzer is placed perpendicular to the polarizer where only light that is the result of birefringent rotation will pass through; all other light is blocked and any other areas in the viewing field are black.

Any field that encounters crystalline materials will be familiar with POM. Colorful crystals are found in geological studies and commonly known chemicals such as folic acid, acetaminophen, and vitamin K. In the area of liquid crystals there are different classifications: intrinsic, stress/strain, structural and flow. Intrinsic birefringence arises from naturally

anisotropic particles, while the stress/strain type is induced by a physical force. Structural and flow-induced liquid crystals are birefringent because of their ordering, either by self-assembly or action of a fluid motion.

In chapter one of this dissertation reflection from liquid crystals is discussed, but POM images are the result of light passing through the liquid crystal. Mesogens will organize into multiple domains as the liquid crystals form. The color of the domain depends on its orientation to the polarized incident light. There are many orientations to consider for the interaction of light with the anisotropic polymer in a cholesteric arrangement. Each plane of a cholesteric is nematic in orientation, and possesses two refractive indices, one in the direction of the long axis of the molecule and another in the direction of the short axis. The longer axis is considered to be the optical axis. In the third dimension the axis of the helical twist is also considered to be an optical axis. Light transmitted along the optical axis passes through at a single velocity and interacts in the same manner as with an isotropic sample. Anisotropic particles positioned at an angle to the polarization position of the incident light will be visible as the light passing through is polarized in the same direction as the ordinary and extraordinary waves, which are oriented perpendicular to one another. As the light exits the crystal components of the wave that are in the same plane as the analyzer will be allowed to pass through. The waves are out of phase and combine to form a new wavelength of the visible color. The phase difference between the two waves is called the retardation. When there is very little retardation the color seen is a shade of grey, but as the amount of retardation increases the crystalline domain will display bright colors.

2.5 Asymmetric Flow Field Flow Fractionation (AF4)

Field flow fractionation (FFF) is named for its predominant feature of particle separation by forces exerted on the particle as it flows through a channel. Variations on the conditions of the

channel flow allow for differences in FFF technique. Sedimentation FFF has a circular channel that rotates at speeds up to 4000 rpm allowing centrifugal forces to act on the sample.[50] The benefit of this technique is that particles of similar size but varying density are separated. The disadvantage of sedimentation FFF is that it may create too much force, in which case asymmetric flow field flow fractionation becomes the better technique. AF4 is operated in a linear channel, under laminar flow, eliminating the threat of shear forces or particle deformation.[51] Other configurations include thermal FFF which employs a temperature gradient that can effect separation of polymers with different chemical compositions and split FFF separating micron-sized particles with the use of two flow streams and two separate outlets.[52-54]

Asymmetric Flow Field Flow Fractionation (AF4) separates polymers or particles in the size range of 10 nm to 2 microns, much larger than is possible with gel permeation chromatography (GPC).[55] It has been proven useful for the separation and characterization of spherical and rodlike particles,[56, 57] biological materials,[58, 59] and environmental samples.[60]
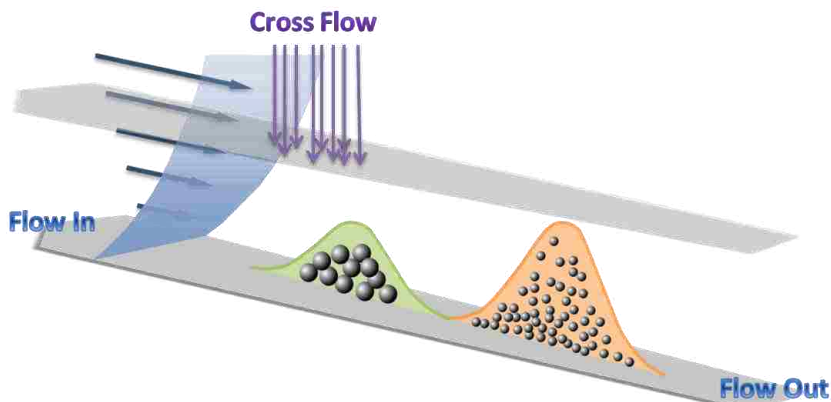
Figure 2.4 Schematic of asymmetric flow field flow fractionation (after Wyatt: http://www.wyatt.eu/index.php?id=asymmetric-flow-fff)

AF4 achieves its high-resolution separations by incorporating two different flows through the channel to produce particle separation according to size. The primary flow, the one responsible for transporting the particles down the channel, assumes a parabolic flow profile

where the highest velocity is at the center of the channel. Flow velocity gradually decreases moving outward from the center radially. The lowest velocity exists near the channel walls. This is important for creating an environment in which the largest particles elute last. The cross flow direction is from top to bottom of the channel, also known as the accumulation wall, essentially pinning the larger particles to the bottom where the velocity is low. Because of Brownian motion, smaller particles will diffuse at higher rates and reach equilibrium at a position higher in the channel where the velocity is faster.[61]

The channel is created by the use of a spacer, a few hundred microns thick, made of some nonbinding material such as Teflon or Mylar. The term asymmetric refers to the trapezoidal shape of the channel which is used to compensate for the linear velocity gradient seen in rectangular channels.[62] Having a more constant flow leads to better separation. To ensure the sample exits through the proper outlet the bottom of the channel is fitted with a frit and membrane that allow the carrier fluid to permeate, but not the sample.[61] Careful choice of a membrane/solvent system is required so that the membrane does not erode, swell, or cause interaction with the sample.[63]

The separation can be coupled to more than one detection system, such as DLS, UV-vis, or mass spectrometry.[64-66] From multi-angle light scattering an intensity versus elution volume (or time) curve is obtained. The accompanying software is capable of calculating the radius of gyration or hydration depending on the model chosen. Similarly, UV-vis and MS provides information about the fraction composition.

2.6 References

1.   Berne, B. J.; Pecora, R., *Dynamic light scattering: with applications to chemistry, biology, and physics*. Dover Publications: 2000.

2.   Lutz, J.-F.; Weichenhan, K.; Akdemir, O.; Hoth, A. About the Phase Transitions in Aqueous Solutions of Thermoresponsive Copolymers and Hydrogels Based on 2-(2-methoxyethoxy)ethyl Methacrylate and Oligo(ethylene glycol) Methacrylate. *Macromolecules* 2007, 40, (7), 2503-2508.

3.   Guoquan Zhu, F. W., Zhen Ding, Yuying Liu, Qiaochun Gao. Aggregation behavior of poly(ethylene glycol)-*block*-poly(γ-benzyl-*L*-glutamate)-*graft*-poly(ethylene glycol) colpolymer and its blends with Poly(γ-benzyl-*L*-glutamate homopolymer in mixed solvents. *Journal of Macromolecular Science, Part A: Pure and Applied Chemistry* 2010, 47, 1006-1011.

4.   Goverman, J.; Schick, L. A.; Newman, J. The bundling of actin with polyethylene glycol 8000 in the presence and absence of gelsolin. *Biophysical Journal* 1996, 71, (3), 1485-1492.

5.   Zackrisson, M.; Andersson, R.; Bergenholtz, J. Depletion Interactions in Model Microemulsions. *Langmuir* 2004, 20, (8), 3080-3089.

6.   Pine, D. J.; Weitz, D. A.; Chaikin, P. M.; Herbolzheimer, E. Diffusing wave spectroscopy. *Physical Review Letters* 1988, 60, (12), 1134-1137.

7.   Maret, G. Diffusing-wave spectroscopy. *Current Opinion in Colloid & Interface Science* 1997, 2, (3), 251-257.

8.   Espinosa-Marzal, R. M.; Nalam, P. C.; Bolisetty, S.; Spencer, N. D. Impact of solvation on equilibrium conformation of polymer brushes in solvent mixtures. *Soft Matter* 2013, 9, (15), 4045-4057.

9.   Haro-Pérez, C.; Ojeda-Mendoza, G.; Vargas, C.; Basurto-Uribe, E.; Rojas-Ochoa, L., Crystal-Liquid Transition in Binary Mixtures of Charged Colloidal Particles. In *Fluid Dynamics in Physics, Engineering and Environmental Applications*, Klapp, J.; Medina, A.; Cros, A.; Vargas, C. A., Eds. Springer Berlin Heidelberg: 2013; pp 253-259.

10.   Nicolai, T.; Urban, C.; Schurtenberger, P. Light scattering study of turbid heat-set globular protein gels using cross-correlation dynamic light scattering. *Journal of colloid and interface science* 2001, 240, (2), 419-424.

11.   Zhao, M.; Jin, L.; Chen, B.; Ding, Y.; Ma, H.; Chen, D. Afterpulsing and Its Correction in Fluorescence Correlation Spectroscopy Experiments. *Appl. Opt.* 2003, 42, (19), 4031-4036.

12.   ALV-GmbH Pseudo Cross & Cross Correlation Detectors. http://www.alvgmbh.de/Products/PMTs___APDs/PCross/pcross.html.

13.   Bantchev, G. B. Simple multiangle, multicorrelator depolarized dynamic light scattering apparatus. *Rev. Sci. Instrum.* 2006, 77, (4), 043902.

14. Wu, C.; Chu, B., Light Scattering. In *Handbook of Polymer Sciences: Experimental Methods in Polymer Science. Modern Methods in Polymer Research and Technology*, Tanaka, T.; Grosberg, A.; Doi, M., Eds. Academic Press: Boston, MA, 2000; pp 1-56.

15. Koppel, D. E. Analysis of Macromolecular Polydispersity in Intensity Correlation Spectroscopy: The Method of Cumulants. *The Journal of Chemical Physics* 1972, 57, (11), 4814-4820.

16. Provencher, S. W. *CONTIN Users Manual*; March, 1984.

17. Provencher, S. W. Contin: A General-Purpose Constrained Regularization Program for Inverting Noisy Linear Algebraic and Integral Equations. *Comput. Phys.* 1982, 27, (3), 229-242.

18. Provencher, S. W. A Constrained Regularization Method for Inverting Data Represented by Linear Algebraic Or Integral-Equations. *Computer Physics Communications* 1982, 27, (3), 213-227.

19. Doty, P.; Kaufman, H. S. The Depolarization of Light Scattered from Polymer Solutions. *The Journal of Physical Chemistry* 1945, 49, (6), 583-595.

20. Badaire, S.; Poulin, P.; Maugey, M.; Zakri, C. In Situ Measurements of Nanotube Dimensions in Suspensions by Depolarized Dynamic Light Scattering. *Langmuir* 2004, 20, (24), 10367-10370.

21. Lehner, D.; Lindner, H.; Glatter, O. Determination of the Translational and Rotational Diffusion Coefficients of Rodlike Particles Using Depolarized Dynamic Light Scattering. *Langmuir* 2000, 16, (4), 1689-1695.

22. Cush, R.; Russo, P. S.; Kucukyavuz, Z.; Bu, Z.; Neau, D.; Shih, D.; Kucukyavuz, S.; Ricks, H. Rotational and Translational Diffusion of a Rodlike Virus in Random Coil Polymer Solutions. *Macromolecules* 1997, 30, (17), 4920-4926.

23. Droegemeier, J.; Eimer, W. Polarized and depolarized dynamic light scattering study on F-actin in solution: comparison with model calculations. *Macromolecules* 1994, 27, (1), 96-101.

24. Fytas, G.; Nothofer, H. G.; Scherf, U.; Vlassopoulos, D.; Meier, G. Structure and Dynamics of Nondilute Polyfluorene Solutions. *Macromolecules* 2001, 35, (2), 481-488.

25. Hoffmann, M.; Lu, Y.; Schrinner, M.; Ballauff, M.; Harnau, L. Dumbbell-shaped polyelectrolyte brushes studied by depolarized dynamic light scattering. *The Journal of Physical Chemistry B* 2008, 112, (47), 14843-14850.

26. Kratohvil, J.; Kerker, M.; Oppenheimer, L. Light scattering by pure water. *The Journal of Chemical Physics* 1965, 43, 914.

27. Farinato, R. S.; Rowell, R. L. New values of the light scattering depolarization and anisotropy of water. *The Journal of Chemical Physics* 1976, 65, 593.

28. Gryczynski, Z.; Lukomska, J.; Lakowicz, J. R.; Matveeva, E. G.; Gryczynski, I. Depolarized light scattering from silver nanoparticles. *Chemical Physics Letters* 2006, 421, (1–3), 189-192.

29. Heckel, J. C.; Chumanov, G. Depolarized Light Scattering From Single Silver Nanoparticles. *The Journal of Physical Chemistry C* 2011, 115, (15), 7261-7269.

30. Koenderink, G. H.; Sacanna, S.; Pathmamanoharan, C.; Raşa, M.; Philipse, A. P. Preparation and Properties of Optically Transparent Aqueous Dispersions of Monodisperse Fluorinated Colloids. *Langmuir* 2001, 17, (20), 6086-6093.

31. Wagner, J.; Härtl, W.; Hempelmann, R. Characterization of Monodisperse Colloidal Particles: Comparison between SAXS and DLS. *Langmuir* 2000, 16, (9), 4080-4085.

32. Watzlawek, M.; Nägele, G. Short-time rotational diffusion in monodisperse charge-stabilized colloidal suspensions. *Physica A: Statistical Mechanics and its Applications* 1997, 235, (1–2), 56-74.

33. Hagen, M. H. J.; Frenkel, D.; Lowe, C. P. Rotational diffusion in dense suspensions. *Physica A: Statistical Mechanics and its Applications* 1999, 272, (3–4), 376-391.

34. Russo, P. S.; Saunders, M. J.; DeLong, L. M.; Kuehl, S.; Langley, K. H.; Detenbeck, R. W. Zero-angle depolarized light scattering of a colloidal polymer. *Analytica Chimica Acta* 1986, 189, 69-87.

35. DeLong, L. M.; Russo Paul, S., Particle Size Distribution by Zero-Angle Depolarized Light Scattering. In *Polymer Characterization*, American Chemical Society: 1990; Vol. 227, pp 65-81.

36. Piazza, R.; Degiorgio, V. Rotational diffusion of hard spheres: forward depolarized light-scattering measurements and comparison to theory and simulation. *Journal of Physics: Condensed Matter* 1996, 8, (47), 9497.

37. Cozzolino, S.; Galantini, L.; Leggio, C.; Pavel, N. V. Correlation between Small-Angle X-ray Scattering Spectra and Apparent Diffusion Coefficients in the Study of Structure and Interaction of Sodium Taurodeoxycholate Micelles. *The Journal of Physical Chemistry B* 2005, 109, (13), 6111-6120.

38. Green, D. L.; Lin, J. S.; Lam, Y.-F.; Hu, M. Z. C.; Schaefer, D. W.; Harris, M. T. Size, volume fraction, and nucleation of Stober silica nanoparticles. *Journal of Colloid and Interface Science* 2003, 266, (2), 346-358.

39. Leggio, C.; Galantini, L.; Zaccarelli, E.; Pavel, N. V. Small-Angle X-ray Scattering and Light Scattering on Lysozyme and Sodium Glycocholate Micelles. *The Journal of Physical Chemistry B* 2005, 109, (50), 23857-23869.

40. Pizzey, C. L.; Pomerantz, W. C.; Sung, B.-J.; Yuwono, V. M.; Gellman, S. H.; Hartgerink, J. D.; Yethiraj, A.; Abbott1, N. L. Characterization of nanofibers formed by self-assembly of β-peptide oligomers using small angle x-ray scattering. *Journal of Chemical Physics* 2008, 129, 095103.

41. Song, C. Q.; Litt, M. H.; Manas-Zloczower, I. Structures of liquid-crystalline hydroxypropylcellulose films crosslinked under shear flow fields. *Macromolecules* 1992, 25, (8), 2166-2169.

42. Bu, Z.; Perlo, A.; Johnson, G.; Olack, G.; Engelman, D.; Wyckoff, H. A small-angle X-ray scattering apparatus for studying biological macromolecules in solution. *Journal of applied crystallography* 1998, 31, (4), 533-543.

43. Zhang, S.; Pfefferle, L. D.; Osuji, C. O. Lyotropic Hexagonal Ordering in Aqueous Media by Conjugated Hairy-Rod Supramolecules. *Macromolecules* 2010, 43, (18), 7549-7555.

44. Als-Nielsen, J.; McMorrow, D., Sources. In *Elements of Modern X-ray Physics (2nd Edition)*, Wiley: Hoboken, NJ, USA 2011.

45. Narayanan, T., Synchrotron Small-Angle X-ray Scattering. In *Soft Matter Characterization*, Pecora, R. B. a. R., Ed. Springer: 2008.

46. Chu, B.; Hsiao, B. S. Small-angle X-ray scattering of polymers. *Chemical Reviews-Columbus* 2001, 101, (6), 1727-1762.

47. Viney, C., *Transmitted polarised light microscopy*. McCrone Research Institute: Chicago, IL, 1990.

48. McCrone, W. C.; McCrone, L. B.; Delly, J. G., *Polarized light microscopy*. McCrone Research Institute: Chicago, IL, 1984.

49. Delly, J. G., *Photography through the microscope*. Eastman Kodak Company: 1988; Vol. 91.

50. Giddings, J. C.; Yang, F. J. F.; Myers, M. N. Sedimentation field-flow fractionation. *Analytical Chemistry* 1974, 46, (13), 1917-1924.

51. Nilsson, L. Separation and characterization of food macromolecules using field-flow fractionation: A review. *Food Hydrocolloids* 2013, 30, (1), 1-11.

52.   Fuh, C. B. Peer Reviewed: Split-Flow Thin Fractionation. *Analytical Chemistry* 2000, 72, (7), 266 A-271 A.

53.   Messaud, F. A.; Sanderson, R. D.; Runyon, J.; Otte, T.; Pasch, H.; Williams, S. An overview on field-flow fractionation techniques and their applications in the separation and characterization of polymers. *Progress in Polymer Science* 2009, 34, (4), 351-368.

54.   Pasti, L.; Agnolet, S.; Dondi, F. Thermal Field-Flow Fractionation of Charged Submicrometer Particles in Aqueous Media. *Analytical Chemistry* 2007, 79, (14), 5284-5296.

55.   Cave, R. A.; Seabrook, S. A.; Gidley, M. J.; Gilbert, R. G. Characterization of Starch by Size-Exclusion Chromatography: The Limitations Imposed by Shear Scission. *Biomacromolecules* 2009, 10, (8), 2245-2253.

56.   Guan, X.; Cueto, R.; Russo, P.; Qi, Y.; Wu, Q. Asymmetric Flow Field-Flow Fractionation with Multiangle Light Scattering Detection for Characterization of Cellulose Nanocrystals. *Biomacromolecules* 2012, 13, (9), 2671-2679.

57.   Gigault, J.; Cho, T.; MacCuspie, R.; Hackley, V. Gold nanorod separation and characterization by asymmetric-flow field flow fractionation with UV–Vis detection. *Anal Bioanal Chem* 2013, 405, (4), 1191-1202.

58.   Chiaramonte, E.; Rhazi, L.; Aussenac, T.; White Jr, D. R. Amylose and amylopectin in starch by asymmetric flow field-flow fractionation with multi-angle light scattering and refractive index detection (AF4–MALS–RI). *Journal of Cereal Science* 2012, 56, (2), 457-463.

59.   Andersson, M.; Wittgren, B.; Wahlund, K.-G. Ultrahigh Molar Mass Component Detected in Ethylhydroxyethyl Cellulose by Asymmetrical Flow Field-Flow Fractionation Coupled to Multiangle Light Scattering. *Analytical Chemistry* 2001, 73, (20), 4852-4861.

60.   Regelink, I. C.; Koopmans, G. F.; van der Salm, C.; Weng, L.; van Riemsdijk, W. H. Characterization of Colloidal Phosphorus Species in Drainage Waters from a Clay Soil Using Asymmetric Flow Field-Flow Fractionation. *J. Environ. Qual.* 2013, 42, (2), 464-473.

61.   WyattTechnologies. How Asymmetric Field Flow Fractionation (AFFF) Theory Works. http://www.wyatt.com/theory/theory/how-asymmetric-field-flow-fractionation-afff-theory-works.html. http://www.wyatt.de/index.php?id=asymmetric-flow-fff.

62.   Litzen, A.; Wahlund, K. G. Zone broadening and dilution in rectangular and trapezoidal asymmetrical flow field-flow fractionation channels. *Analytical Chemistry* 1991, 63, (10), 1001-1007.

63.   Podzimek, S., Asymmetric Flow Field Flow Fractionation. In *Light Scattering, Size Exclusion Chromatography and Asymmetric Flow Field Flow Fractionation*, John Wiley & Sons, Inc.: 2011; pp 259-305.

64.   Bednar, A. J.; Poda, A. R.; Mitrano, D. M.; Kennedy, A. J.; Gray, E. P.; Ranville, J. F.; Hayes, C. A.; Crocker, F. H.; Steevens, J. A. Comparison of on-line detectors for field flow fractionation analysis of nanomaterials. *Talanta* 2013, 104, (0), 140-148.

65.   Modig, G.; Nilsson, L.; Bergenståhl, B.; Wahlund, K.-G. Homogenization-induced degradation of hydrophobically modified starch determined by asymmetrical flow field-flow fractionation and multi-angle light scattering. *Food Hydrocolloids* 2006, 20, (7), 1087-1095.

66.   Smith, M. H.; South, A. B.; Gaulding, J. C.; Lyon, L. A. Monitoring the Erosion of Hydrolytically-Degradable Nanogels via Multiangle Light Scattering Coupled to Asymmetrical Flow Field-Flow Fractionation. *Analytical Chemistry* 2009, 82, (2), 523-530.

CHAPTER 3. PARTICLE INTERACTIONS WITH CHOLESTERIC LIQUID CRYSTALS

3.1 Introduction

3.1.1 Phase Behavior of Colloids

A phase is defined as a region of space throughout which all physical properties of a material are essentially uniform. The importance of studying phase behavior lies in the ability to determine the structure or stability of the system. Particles and polymers of various shapes and spanning the colloidal size range are incorporated into solutions to afford them certain properties. For example, silica or titanium oxide nanoparticles, because of their light scattering properties, may make a solution white instead of clear. Rheological behavior can be tuned to exhibit a certain behavior depending on the concentration or molecular weight of the polymer. Phase behavior studies examine and quantify the interactions between the colloids and polymers in solution so that they are used effectively. For clarification, the term phase behavior is a broad description including both the one-particle transition from a disordered to ordered phase and the two-particle system where initially mixed particles separate. In this dissertation both cases are included.

The isotropic-to-nematic (I-N) transition has been described theoretically, experimentally, and by simulation. Flory[1, 2] and Onsager[3] were pioneers in the field of liquid crystals. Both constructed models for the transition of hard particles in solution from random to ordered phases, but their models used different mathematical approaches. Flory developed a lattice theory where each point on the lattice is occupied by either a solvent molecule or a monomer unit. Onsager was the first to show that the Density Functional Theory (DFT), when approximated to the second virial coefficient, could be applied to long, thin rods.[3]

DFT has become one of the most popular methods for determining where a phase transition will occur. With over three thousand citations of Onsager's paper from 1949, its principles have been applied to a variety of materials in several different fields. For the purposes of studying rodlike colloids, this theory has been extended to include rods that are semi-flexible, charged, or possess a finite length.[4-6] The equation describes the free energy (F) of a hard particle fluid and considers only the particle interactions stemming from the second virial coefficient, where $\rho(r)$ is the density distribution of particles as a function of the direction vector, r, and $\beta(r_1,r_2)$ involves the interaction potentials appropriate to pairs of particles as developed by Mayer and Mayer.[3, 7, 8] The subscripts 1 and 2 distinguish between particles in the case of two particles interacting.

$$\frac{F}{k_B T} = \int_V dr\rho(r)\ln(\rho(r)) - \frac{1}{2}\int_V dr_1 \int_V dr_2\rho(r_1)\rho(r_2)\beta(r_1,r_2) \tag{3.1}$$

The first term in the equation is considered the ideal part, similar to the behavior of ideal gases, and mathematically restricts the transition to an ordered state. The second term describes the interaction energy between two particles, which is minimized for the transition to an ordered state in some cases. Although there is competition between the two terms, the free energy equation is optimized when at its minimum, and likewise, entropy is at its maximum.

For binary mixtures of hard particles, phase behavior becomes more complex. The interaction between the particles in solution can be explained by the depletion theory put forth by Asakura and Oosawa in the late 1950s.[9, 10] It states that when the distance between two particles, immersed in a polymer solution, becomes less than the rotational volume of a polymer it is entropically favorable for the polymer to no longer inhabit that space. The polymer will remain on the outside of the two particles, creating a gradient in osmotic pressure that is greatest on the outside of the particles and lowest between them. The outside force can be perceived as a net
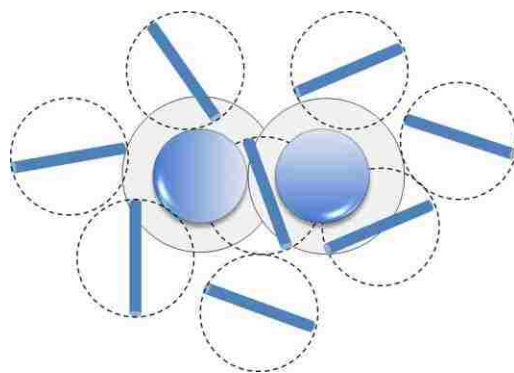
Figure 3.1 Schematic representation of the depletion of spherical particles by rods. The shaded area around the spherical particle is the region of excluded volume. For the rodlike particles, excluded volume is represented by the dashed lines.

attraction between these particles, which contributes to their ordering or demixing. In Figure 3.1 the rodlike polymer shown between the spheres serves to depict its limited range of motion in the sphere overlap region. The term depletant is given to the typically smaller entity that is creating pressure on the larger colloid. Depletants can be nonadsorbing polymers, spherical particles or rodlike particles, with rods being the most efficient type.[11-20] It should also be noted that, kinetically, depletion is not considered to be an instantaneous event. Vliegenthart describes the process as a build-up of pressure over time with diffusive processes at its root[18] and variables such as rod concentration affecting the depletion rate.[21]

The study of phase separation in colloid-colloid mixtures has expanded to include a variety of particle shapes originating from the principles of the Derjaguin theory which extends the Asakura and Oosawa model of flat plates to the curved surface of spheres with restrictions to the case of spheres larger than rods.[22, 23] Phase behavior of binary mixtures is not limited to rods and spheres; rod-rod mixtures of different aspect ratios have exhibited nematic-to-nematic transitions,[24, 25] and mixtures of rods with discs separated into a nematic or smectic phase for the rods and a columnar phase for the discs.[26] Phase behavior of colloidal particles has been studied in depth by Fraden and Dogic, known for their use of rodlike or filamentous viruses.[4, 27-34]

53

Tobacco mosaic virus (TMV) and bacteriophage *fd* are naturally occurring, rodlike polymers that are highly monodisperse, more so than what is currently available synthetically, which is particularly important because phase behavior varies with the size of the polypeptide.[30, 35] Genetic modification of viruses allows for adjustment of the length of the polymer and its surface charge density. Rodlike viruses have been mixed with spherical colloidal particles such as dextran,[29] polyethylene oxide[36] and bovine serum albumin.[31] Virus colloids mixed with spherical particles have resulted in a variety of interesting and complex phases including lamellar, smectic, columnar and disordered structures.[36]

Very specific conditions exist for most phase behavior experiments, leading to seemingly infinite combinations of colloid and solvent systems to study. A couple of the more commonly reviewed cases are charged colloidal particles and polymers, whose additional repulsive forces alter phase boundaries for particles of similar size,[37-40] and the effects of polydispersity on boundary positions.[41, 42] Theoretical studies and simulation of phase behavior of colloidal particles have improved upon initially established theories in addition to corroborating experimental data.[43-45] For rod-sphere mixtures, where the rods are longer than the spheres, but have equal diameters, Antypov and Cleaver were able to explain phase behavior in terms of the strength of the particle interactions and the concentration ratio of rods to spheres.[46] For rodlike colloids mixed with nonadsorbing polymers, it is important to distinguish between depletion attraction between rods and the entropy-driven ordering of rods as modeled by DFT.[4, 47, 48] Dijkstra has studied colloidal systems by comparing various models for colloid-polymer phase behavior. Gast *et. al.* have attempted to bridge the gap between theory and experimentation with several studies of phase transitions in two-component mixtures.[38, 49-52]

3.1.2 Particles in Liquid Crystals

Depletion interactions and isotropic-to-crystalline phase transactions occur at the more dilute end of colloidal concentration studies. The possible combinations of particles, experimental conditions and theoretical treatments are so vast that decades have been dedicated to their study. The same rodlike polymers that behave as depletants in one instance are also capable of forming a liquid crystalline phase above a certain concentration, turning the attention toward the behavior of colloidal particles immersed in a liquid crystal. Similarities remain in terms of the exclusion of spherical particles, but other factors need to be considered such as the liquid crystalline superstructure and where the particles will reside in the crystalline matrix.

Liquid crystal applications are numerous and the logical next step is to combine them with colloidal particles bringing about new materials with enhanced optical, electronic or mechanical properties.[53-57] The interactions of liquid crystals with colloidal properties are complex. Mesogens order themselves in an attempt to seek their lowest energy configuration, but the addition of colloidal particles to that matrix causes a disturbance that the liquid crystal must accommodate. Several experimental and theoretical studies have been completed concerning colloidal particles of various shapes and sizes in nematics,[58-62] but the cholesteric phase is gaining in popularity as more is learned about particle interactions in its more complex structure.[63-67] Cholesteric LCs display very specific colors depending on the helical pitch. Chepikov *et. al.* found that carbon nanotubes and clay platelets imbedded in a liquid crystalline phase are capable of changing the reflection color, but the presence of platelike particles did not affect the planar cholesteric texture. From this it was determined that the plates are oriented normal to the helical axis and integrated into the cholesteric structure.[68] Locally, when particles are much larger in diameter than the helical pitch, they distort the director and the mesogens will

wrap around the individual particle in a spiral formation. Large quantities of particles aggregate at defect points or form flat sheets of colloids as concentration is increased. This is in contrast to the particle strings formed in nematics or small particles that do not distort the director.[53, 65, 66, 69, 70] For the same reason, the coexistence state displays interesting behavior when particles are dispersed. As regions of liquid crystalline droplets nucleate and grow, particles are pushed to the outside and can eventually form a network similar to cellular structure.[71, 72] They also aggregate at interfaces between the solution and air or two different phases.[73, 74]

3.2 Experimental

3.2.1 Materials

The synthesis of the silica-polypeptide composite particles was performed by a former student of this research group, Dr. Erick Soto-Cantu. A full description of the synthetic methods can be found in his dissertation and in publication.[75, 76] For the work presented here particle synthesis is not the focus, but some background information is required to provide a full picture of the particles used in this study.

Synthesis of hybrid particles begins with a silica core followed by the addition of a polypeptide shell.[77, 78] Although this general structure has not changed, recent upgrades include the addition of iron oxide or cobalt nanoparticles at the center of the silica core and a fluorescent layer embedded between two silica layers. The silica core is synthesized by the Stöber[79] method to yield monodisperse particles; then the polypeptide is grown from the surface to create the shell of the particle. Distinction from the grafting-to method should be made as particle synthesis using the "click" method has also been completed by this group.[80] The silica core has a diameter of 102.5 ± 3.6 nm measured by DLS at the time of synthesis. Approximately 7 g of BLG-NCA was added to the mixture to create the shell.
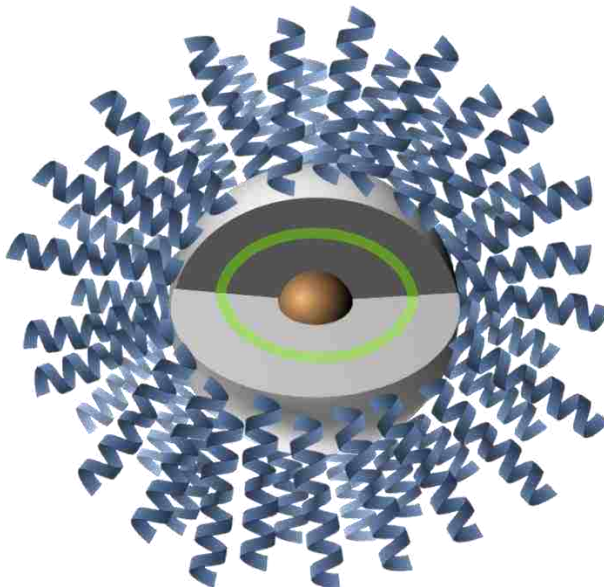
Figure 3.2 Alpha-helical polypeptide shell on a silica particle with a fluorescent layer and a magnetic core.

PBLG was obtained from Sigma Aldrich with a molecular weight of 91,000 as provided by the manufacturer (lot # 96F-5015). The polymer was not newly purchased but was tested for degradation by GPC and NMR and the polymer was intact. Anhydrous pyridine in a sure-seal bottle was also purchased from Sigma Aldrich and used without further purification. Bare silica particles having a hydroxyl surface and 150 nm in diameter, were purchased from Bangs Laboratories, Inc. Magnetic, fluorescent silica particles with amine surface groups (50 nm in diameter) were synthesized by Dr. Balamurugan.

3.2.2 Sample Preparation

Solutions were prepared by dissolving PBLG in pyridine at a high concentration, typically 40 wt%, creating a stock solution. A small portion was removed by capillary action into a Vitrocom rectangular cell (typically, 3 mm × 0.3 m i.d.) which was flame sealed and dipped in wax to guard against any small leak near the seal. The stock solution was then diluted and its concentration recalculated in order to take a new sample. Further dilutions followed until the

stock solution became isotropic. In some cases, the solution was prepared slightly below the liquid crystalline transition point and then concentrated by a stream of nitrogen gas until the stock solution became crystalline. To add silica and hybrid particles to the PBLG/Pyridine mixture, a stock solution was created. Varying amounts of the stock solution were added to achieve the desired ratio of polymer and particle to solvent.

3.2.3 Polarizing Optical Microscopy

Optical microscopy was performed using an Olympus BH polarizing optical microscope equipped with a digital AmScope Camera (Model MD 1900-CK) and image capture software provided by the same company. Photographs were taken of the samples in the Vitrocom cells in which they were prepared.

3.2.4 Confocal Microscopy

Confocal images were obtained at LSU's Socolofsky Microscopy Center using a Leica TCS SP2 Spectral Confocal microscope with compatible Leica LCS software. Samples were viewed with an HC (harmonic compound) apochromatic 20x objective with UV specification in the same Vitrocom cells used for polarizing microscopy.

3.2.5 Small/Wide Angle X-ray Scattering

X-ray scattering measurements were conducted at the Center for Advanced Microstructures and Devices (CAMD), Louisiana State University, Baton Rouge, LA with synchrotron radiation of 1.54 Å at 8.00 kEV. A narrow band of X-ray wavelengths are selected using an LNLS (Laboratorio Nacional de Luz Synchrotron, Brazil) double crystal monochromator and collimated with three pinholes of 200, 400 and 800 μm or two 800 μm pinholes. The samples are flame sealed in glass capillaries (1 cm O.D. and 10 μm wall thickness) supplied by Charles Supper Company and suspended in the beam path with a *q* range of 0.006 to

0.164 Å^{-1} for SAXS and 0.15 to 2.72 Å^{-1} for WAXS. The diffraction pattern is recorded using a Molecular Metronics Gabriel-style 2D multiwire gas-filled detector with a 200 mm diameter and a resolution of 200-250 μm FWHM in a 1024 x 1024 array. For wide angle scattering, a Kodak PhosphorImager image plate and scanner are used. The image plate has 200-μm pixel size. SAXS data were analyzed using SAXSGUI software by JJ X-ray (Denmark) and WAXS data using Fit2D developed at the European Synchrotron Radiation Facility (ESRF) in France.

SAXSGUI reads raw data from the diffractogram and recreates an image of the ring pattern. Silver behenate is used as a calibration standard for aligning *q*-values (establishing the sample-to-detector distance) and determining the center of the ring. The radial image is linearized with *q*-values increasing from left to right. Data are exported as three columns including the *q*-values, intensity in arbitrary units and the error associated with intensity. The intensity data are normalized to time and have units of counts/pixel/second. As a result, it is not necessary to divide through by sample or background transmission. All SAXS data are treated by dividing the intensity by the corrected photodiode reading, which is obtained by subtraction of the photodiode dark count. Additionally, solution samples require subtraction of the background solvent to produce the final scattering curve.

Similar to SAXSGUI, Fit2D also displays an image of the diffractogram. A certain amount of error is introduced according to the manner in which the center is chosen. For data presented here, the center is chosen using the graphical coordinate which prompts the user to choose a center spot visually. This estimation does not vary the data tremendously, but small differences may be noticeable. Scattering angle and intensity are exported, but error is not provided. WAXS data are used directly as no photodiode reading is available.

3.3 Results and Discussion

3.3.1 Potential between Two Spheres

Depletion attraction is the driving force for phase separation in a colloidal mixture of rods and spheres. For the case of a depletant smaller than the radius of the colloidal sphere the following equation was derived for the potential W, which is a function of the surface-to-surface distance h between the colloidal spheres.[12] The dimensions of the rod are length L and diameter D. The rod's volume fraction is represented by ϕ_r. The sphere radius is R and k_BT is the thermal energy.

$$W(h) = -\frac{2}{3}k_BT\phi_r \frac{L}{D}\frac{R}{D}\left(1 - \frac{h}{L}\right)^3 \qquad (3.2)$$

Negative depletion potential values describe an attraction between colloidal particles while positive values indicate repulsion. A value of zero indicates no net force is experienced by the colloids. Depletion potential curves corresponding to the systems studied in this dissertation are shown in Figure 3.X. No net force acts on the colloids when they are separated by a distance of 62 nm, which is the length of the PBLG rod, but as the particles move closer together they
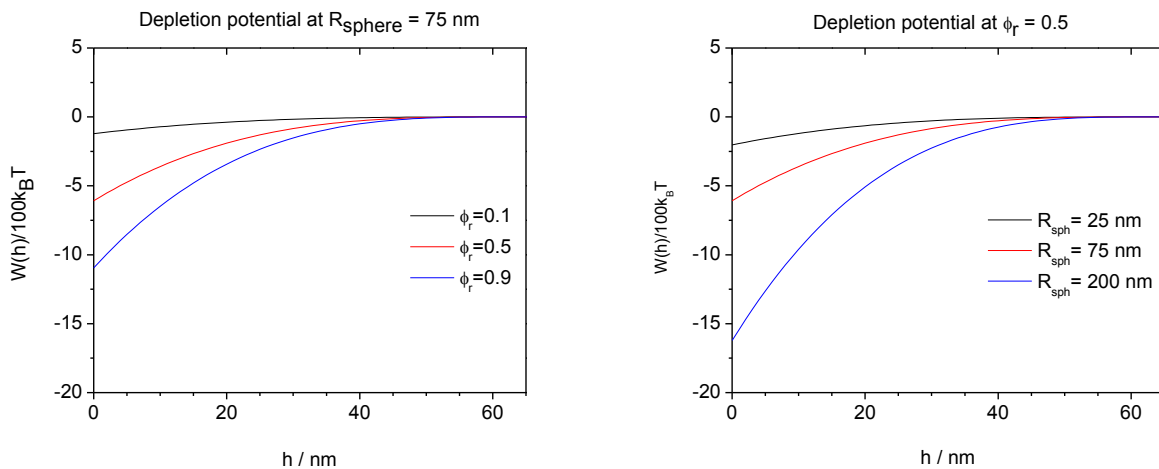
Figure 3.3 Depletion potential curves for a sphere radius of 75 nm at rod volume fractions of 0.1, 0.5 and 0.9 and for a constant rod volume fraction of 0.5 with sphere radii of 25, 75 and 200 nm.

begin to feel an attractive force. Three sphere radii and rod concentrations are shown which correspond to the three particle sizes used in the phase behavior studies. Increasing either rod volume fraction or sphere size increases the amount of depletion attraction between spheres, but having a large colloidal particle has a greater effect on depletion forces than a high concentration of rods. For phase behavior studies of rods and spheres in this dissertation, rod volume fractions never exceeded 50%, but in all cases spheres should still experience attraction at separation distances less than the length of the rod.

These depletion calculations estimate an extremely large particle interaction and particle aggregation is observed experimentally. Although depletion potentials as defined by Asakura and Oosawa include the generalities that $W(h)$ tends to infinity when $h<L$, but equal to zero when $h>L$, calculation of exact values of in the interaction potential for rod/sphere mixtures at $h>L$ are positive, indicating a repulsive force between spheres. This repulsive force is described as resulting from the stabilization of spheres due to the presence of many smaller particles, which effectively block interaction between colloids.[81] Another consideration is the concentration of the depletant. In this dissertation, the concentrations of rods far exceed those necessary to affect depletion interactions and this equation may not hold under these conditions.[13, 82] The attraction between colloidal spheres is not only important for depletion, but for the formation of the liquid crystalline phase as well. Aggregation of spheres effectively increases the rod concentration by decreasing their available volume compared to a sample of equal rod concentration with no spheres present.

3.3.2 Phase Behavior

Three different phase behavior diagrams were constructed showing the transition of PBLG from the isotropic to liquid crystalline phase in the presence of a spherical colloidal

particle. Onsager defined the points ϕ_A and ϕ_B as the concentrations from which the rodlike polymers transition from isotropic to biphasic and from biphasic to crystalline, respectively. Isotropic refers to a random arrangement of rods incapable of effectively polarizing light such that when viewed through crossed polarizers, the image is black. In a biphasic region small crystalline domains begin to appear where the polymer concentration is higher than its surroundings taking on the form of spherulites, which are birefringent spheres. A black maltese cross is often visible in the spherulite aligned in the direction of the crossed polarizers.[83] As concentration increases spherulites grow in size and potentially coalesce to form larger structures that may be slightly less defined. A continuous birefringent phase is considered to be a crystalline sample. An example of this transition can be found in a single sample in Figure 3.4 showing spherulites and a uniform crystalline region. In the phase diagrams to follow, samples viewed in the polarizing microscope were placed into one of the three categories mentioned. The phase plots are constructed in terms of weight fraction of PBLG and the colloidal particle without changes in pyridine concentration shown directly. This focuses on the effects of increasing the polypeptide and colloid concentration, which were kept at a constant ratio to one
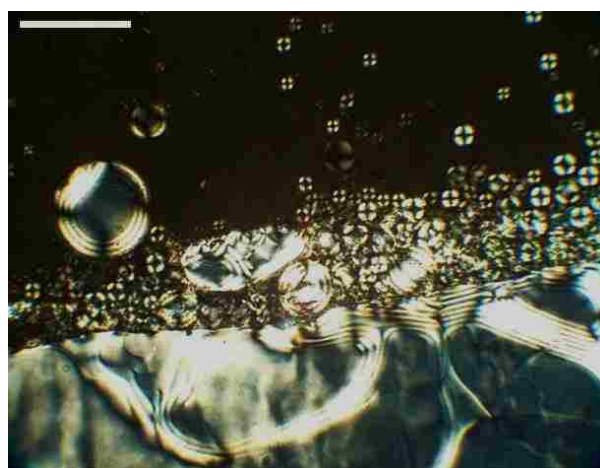
Figure 3.4 Transition from a biphasic region to a crystalline region in a single sample. Sample composition is 2 wt% silica, 17 wt% PBLG (MW 91k, L=62 nm), and 81 wt% pyridine. Scale bar 150 μm.

another as the amount of solvent was varied. The effect of maintaining the concentration ratio of rods and spheres gives the phase data the appearance of rays emanating from the origin. The same data plotted on a ternary triangular plot has a similar appearance in terms of where the phase boundaries are located.

Early concerns that the silica particles may be attracted to the glass wall of the sample cell were explored by confocal microscopy. Figure 3.5 is a series of photographs taken at different depths of a single sample region. The aggregate of silica circled in blue is initially out of focus, but becomes progressively more visible as the focusing depth changes, while other particles move out of focus, indicating that the silica is not gathered only at the surface of the liquid crystalline phase.
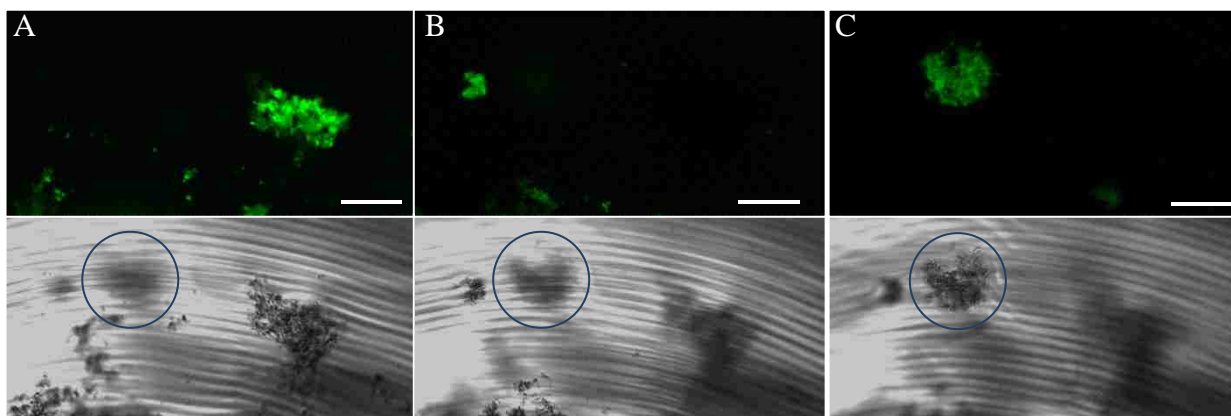
Figure 3.5 Confocal and corresponding fluorescence images of a sample of fluorescent silica (50 nm diameter) immersed in a PBLG/pyridine cholesteric liquid crystal. The three images are of the same position on the sample at depths of (A) 60, (B) 139 and (C) 191 microns from the surface. Scale bar is 50 microns.

3.3.2.1 PBLG with Magnetic Silica Particles

Silica particles with a magnetite core and a fluorescent layer from FITC were used to create a phase diagram for PBLG in pyridine. The particle surface was functionalized with an amino group ($-NH_2$), which is the precursor to addition of polypeptides to the surface. The total diameter of the silica particles is 50 nm which is smaller than the length of PBLG rods at 62 nm.

In general, adding colloidal particles to the mixture hastens the formation of the liquid crystalline

phase. Along the x-axis, where particle concentration is zero, PBLG transitions from isotropic to

Figure 3.6 Phase plot showing transition from isotropic to crystalline for fluorescent, magnetic silica particles (50 nm in diameter) mixed with PBLG (MW 91k, L=62 nm) and pyridine.

biphasic at approximately 18 wt%. As the particle concentration is increased, the transition point

occurs earlier and the biphasic region is no longer visible. At low PBLG concentrations, less than

10 wt%, no crystalline regions are formed.

The obvious aggregation of the particles could result from depletion affects in which the

liquid crystalline phase eventually formed around them, but some portion of their attraction may

be attributed to their magnetic cores. Pictured in Figure 3.7 are polarized optical microscopy

photographs representative of samples falling in the categories of isotropic, biphasic and

crystalline phases. The isotopic region shows no birefringence from PBLG. Tiny specs of light

are potentially dust particles, which are also often birefringent. In the biphasic region spherulites

appear and the crystalline phase is uniformly birefringent. Silica appears dark brown in color

because of the magnetic core and high concentrations of silica nearly block out light transmitted through the liquid crystal in some cases. More sample photographs can be found in Appendix A along with their corresponding concentrations.
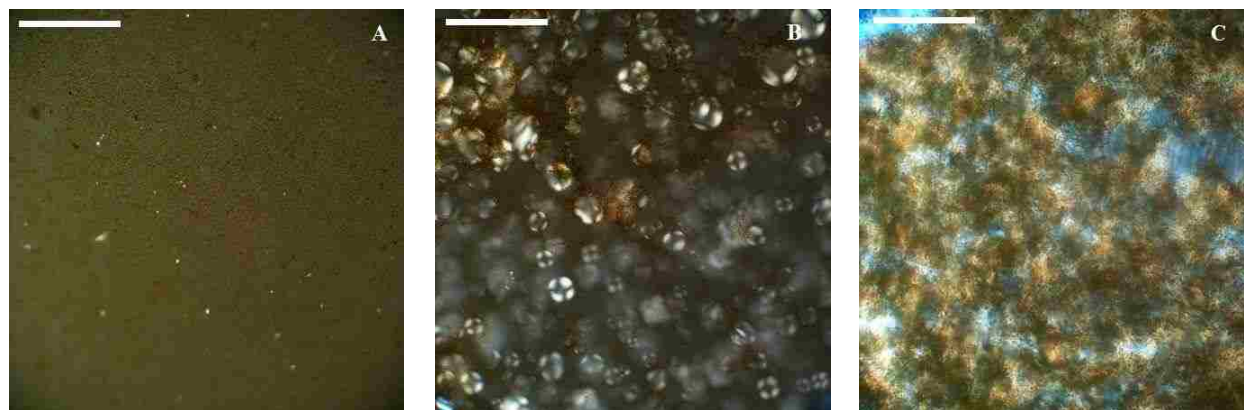
Figure 3.7 Representative POM photographs of the (A) isotropic, (B) biphasic and (C) crystalline regions of the phase diagram for PBLG (MW 91k, L=62 nm), pyridine and magnetic, fluorescent silica particles (50 nm in diameter).

3.3.2.2 PBLG with Bare Silica Particles

Silica particles with a 150-nm diameter, lacking magnetic and fluorescent inclusions, were used for a second phase diagram with the goal of comparing bare particles with those that are polypeptide coated. Many of the hybrid particles synthesized by the group have a silica core with a diameter between 100 and 200 nm, so this size was chosen with the intent of falling within that range. The particles in this phase diagram are not functionalized in any way and have only hydroxyl groups (-OH) on the surface.

Along the x-axis the same plot of PBLG's transition to the crystalline phase is used. Similar to the previous phase diagram, less PBLG is required to transition to biphasic as particle concentration is increased. Although a direct relation cannot be formed because these particles are not magnetic, a comparison to the previous phase diagram shows that the biphasic region does not form as quickly with increase in particle concentration as with the magnetic particles. It
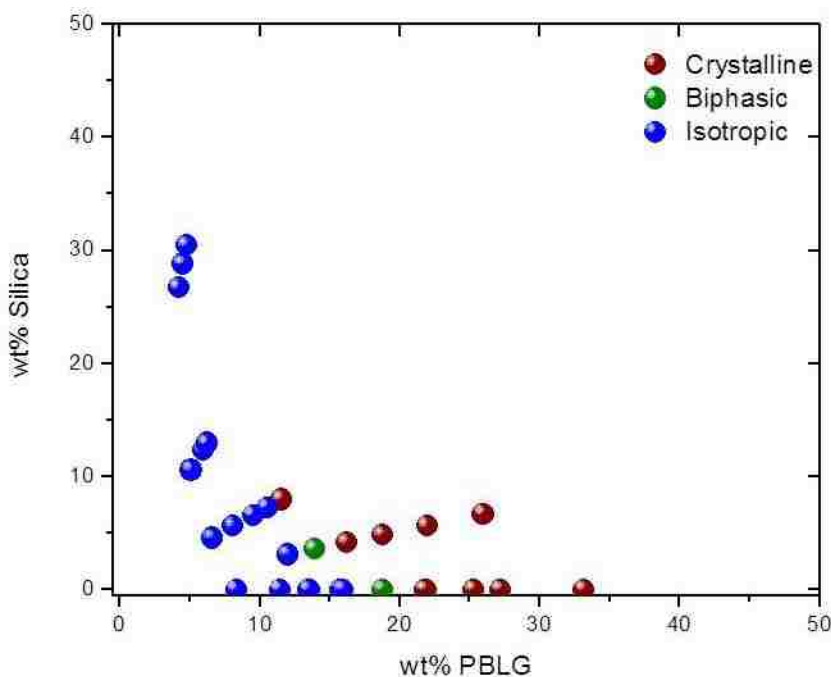
Figure 3.8 Phase plot showing transition from isotropic to crystalline for silica particles (150 nm in diameter) mixed with PBLG (MW 91k, L=62 nm) and pyridine.

may be that the non-magnetic silica particles are more easily integrated into the crystalline phase having the effect of broadening and delaying the onset of the biphasic region.

An interesting effect was observed with only colloidal silica and pyridine. Silica particles in basic solvents such as dimethylformamide and pyridine are charged.[37, 84] The electrostatic repulsion between charged particles contributes to their stability in solution and ultimate ability to form colloidal crystals instead of only amorphous aggregates.[85] It is questionable whether this effect should be incorporated into a phase diagram for liquid crystals, but for the purpose of establishing textural changes of the samples in the phase diagram, it is included. Figure 3.9 is a POM image showing only silica and the bright colors that arise from this sample.

In general, samples with more PBLG than silica will resemble samples of PBLG alone (Figure 3.4). As the silica concentration increases the mixture takes on a different texture and the distance between cholesteric pitch lines become much smaller. In Figure 3.10 both silica and
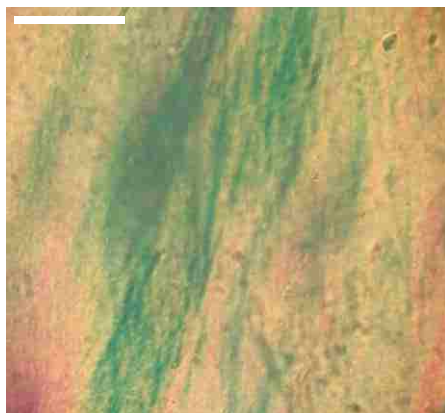
Figure 3.9 POM photograph of silica (31 wt%) in pyridine. Scale bar is 150 μm.

PBLG are at a concentration of approximately 21 wt%. There are no obvious aggregates as seen in earlier cases and the silica appears to be integrated into the liquid crystalline matrix. The photograph of a single spot in the sample is shown with and without crossed polarizers. The golden brown tint is due to the high concentration of silica as PBLG (without crossed polarizers) has no apparent color. While the cholesteric pitch range is 16-34 μm for PBLG (91k MW in pyridine) liquid crystals, the addition of a high concentration of silica decreases it to approximately 4 μm.
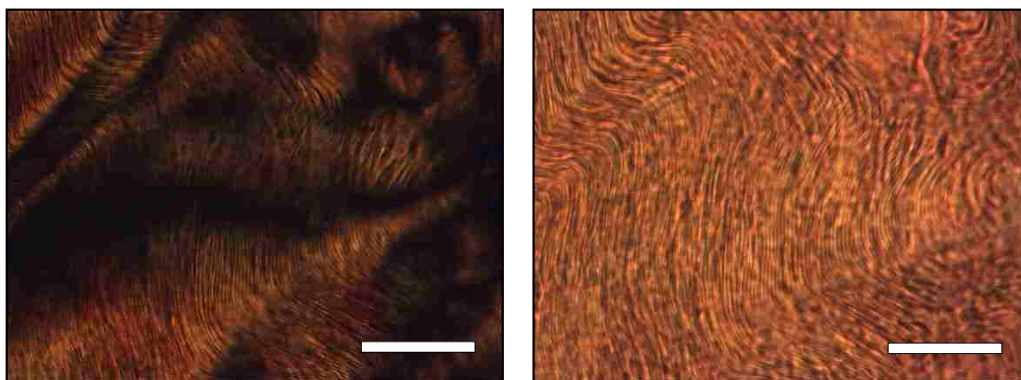
Figure 3.10 POM image of 21 wt% 50:50 Silica:PBLG (PBLG 91k, L=62 nm) in pyridine. The sample is taken in the same spot with (left) and without (right) crossed polarizers. (MC.1.15D). Scale bar is 50 μm.

3.3.2.3 PBLG with Hybrid Silica-PBLG Particles

Depletion interactions result when it becomes entropically unfavorable for a rod to maintain its position between spheres where their excluded volumes overlap. Additionally, for rodlike polymers, it is entropically favorable for them to form ordered structures at high concentrations. Silica-polypeptide hybrid particles are the primary particle of interest in this study with the objective being to explore particles that would not interact chemically with unbound polypeptides in solution, but only physically.

The phase diagram for silica-polypeptide particles mixed with PBLG is once again constructed with PBLG along the x-axis. Similar to previous phase diagrams, the presence of particles in solution lessens the required amount of PBLG to reach the biphasic state. The y-axis contains only hybrid particles and a biphasic region is observed above 35 wt%, where the polypeptides on the surface of the particle can interact enough to form birefringent regions, but a continuous crystalline phase is not achieved. In terms of the boundaries between phases, immediately noticeable is the large size of the biphasic region of this phase diagram compared to the previous ones with bare silica. As suggested earlier for the larger silica particle, an increased biphasic region could indicate a closer interaction between the particle and the polypeptides in solution, but the drastic increase in this biphasic region may be considered in two ways. In one respect, the much larger diameter (400 nm) of the hybrid particle prevents the uniform crystalline phase from forming as just over 20 wt% PBLG is required with or without particles in order to form the continuous LC phase. Alternately, it could be considered that the hybrid particles can surround large spherulites help to stabilize them and prevent them from coalescing into the uniform phase (Figure 3.12).
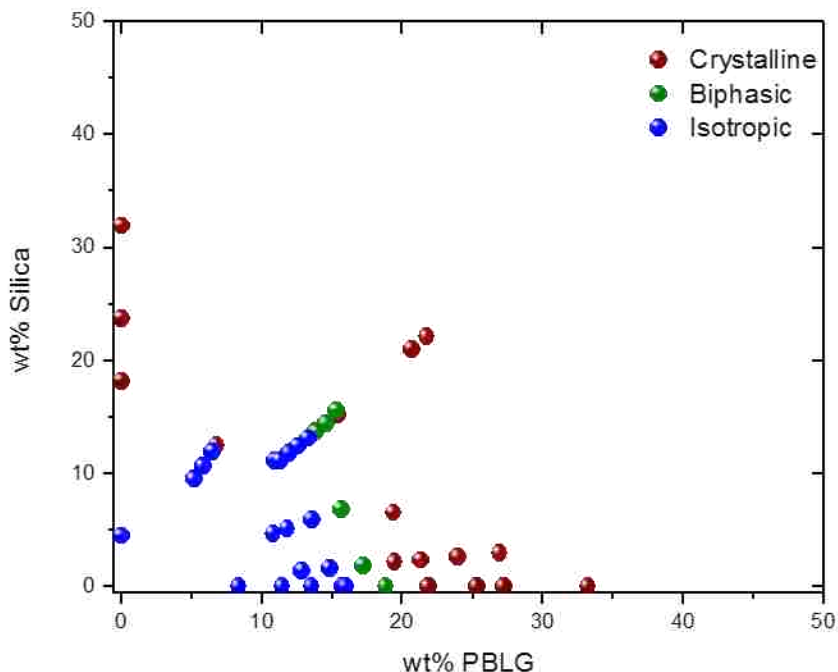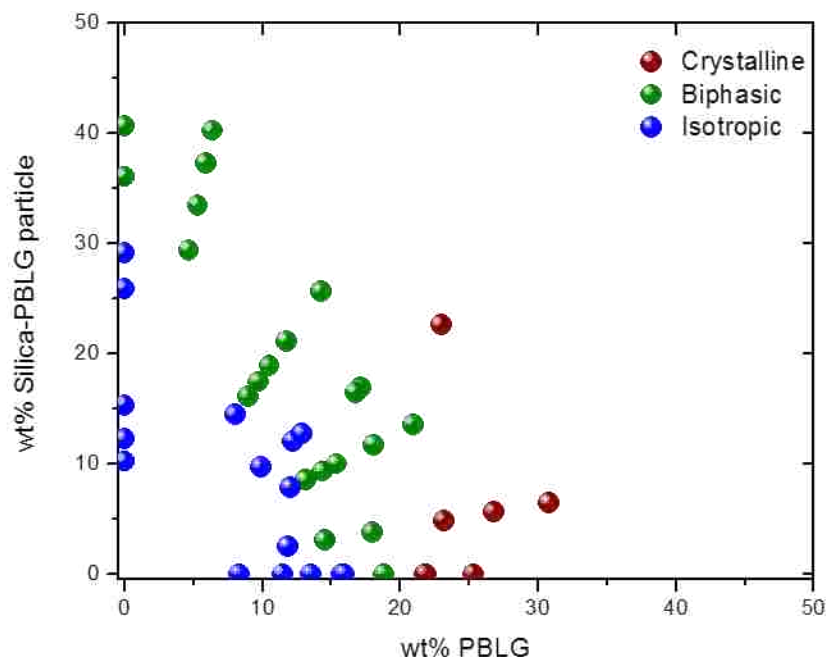
Figure 3.11 Phase plot showing transition from isotropic to crystalline for silica-PBLG hybrid particles (400 nm in diameter) mixed with PBLG (91k, L=62 nm) and pyridine.

Particles with homeotropic anchoring, where the polymers extend normal from the surface of the colloid, are expelled from nematic LC droplets because their presence can lead to long-range defects which are energetically unfavorable.[72] Homeotropic anchoring of PBLG to the silica core may have the same disruptive effect on the formation of an ordered cholesteric droplet because of the local nematic ordering, pushing particles to the outside of spherulites. The morphology of the sample also depends on the kinetics of the phase transition to liquid crystal. It has been observed that when spherulites are allowed to grow slowly in size and the particles continue to be expelled, they will eventually form a cellular-like network between crystalline phases.[71, 72]

When looking at the phase plot, it is tempting to follow the "rays" that appear to extend form the origin, but more informative are comparisons made between similar concentrations of hybrid particles and varying amounts of PBLG, and vice versa (reading across the diagram left-

69
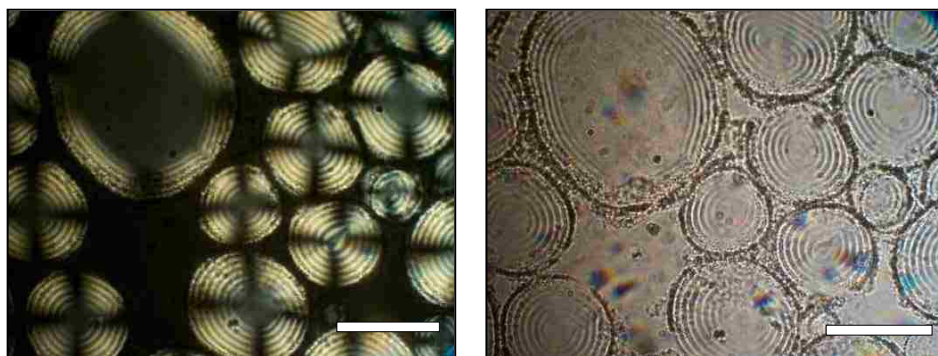
Figure 3.12 Particle-stabilized biphasic region of the phase diagram composed of 13.2 wt% PBLG (MW 91k, L=62 nm), 8.5 wt% silica, and 78.3 wt% pyridine. The photograph is taken of the same spot on the sample with and without crossed polarizers. Scale bar is 50 μm.

right and up-down, respectively). Comparing 9 wt% and 17 wt% PBLG at a fixed amount of 16 wt% hybrid particle (Figure 3.13), both samples are in the biphasic region, but the sample containing the higher amount of PBLG has larger spherulites and no obvious particle presence, while the sample with the higher particle concentration appears to show some birefringence from particle aggregation and the spherulites are less well defined. Keeping the concentration of PBLG fixed at 14 wt% and varying the concentration of hybrid particle from 3 wt% to 25 wt%
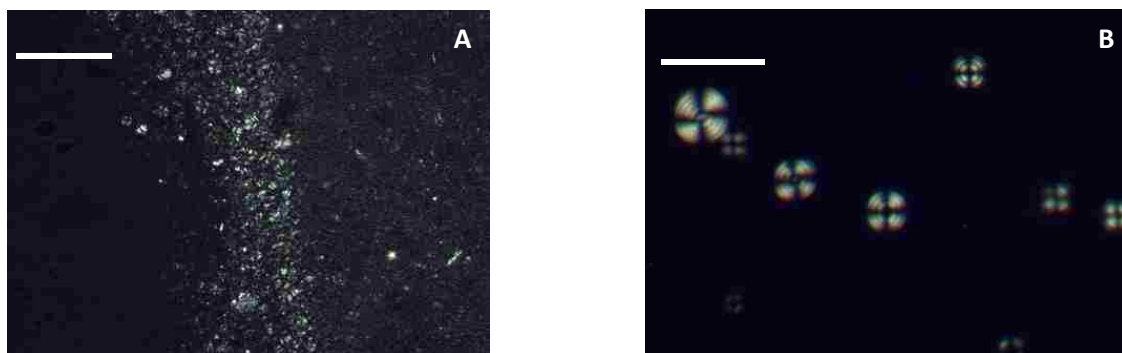
Figure 3.13 Comparison of 16 wt% hybrid particle with (A) 9 wt% and (B) 17 wt% PBLG. Scale bar is 150 microns.

brings the mixture from the early stages of the biphasic region to a nearly uniform LC. Some resolution is lost in translating the images to print, but the pitch in Figure 3.14B is in the range of 2-4 microns, similar to what is measured for high concentrations of bare silica mixed with

70

PBLG. If a straight line on the phase diagram is drawn from 35 wt% hybrid particle to 18 wt% PBLG, allowing for some error in the transition between the isotropic and biphasic region, particle concentration has a greater effect on the transition to crystalline than the concentration of PBLG which is reflected in the images below.

In addition to visual differences between samples, there were also physical differences regarding how well the sample flowed. Glass cells were placed flat on the microscope stage for viewing. A majority of samples were stationary in this position, but in some cases the crystalline phase would begin to flow even to the extent of being difficult to photograph. To compensate, these samples were placed at a slight upward angle to prevent movement. Samples with high concentrations of particles (for example, 40 wt%) were very viscous and would only flow under force or over several hours.
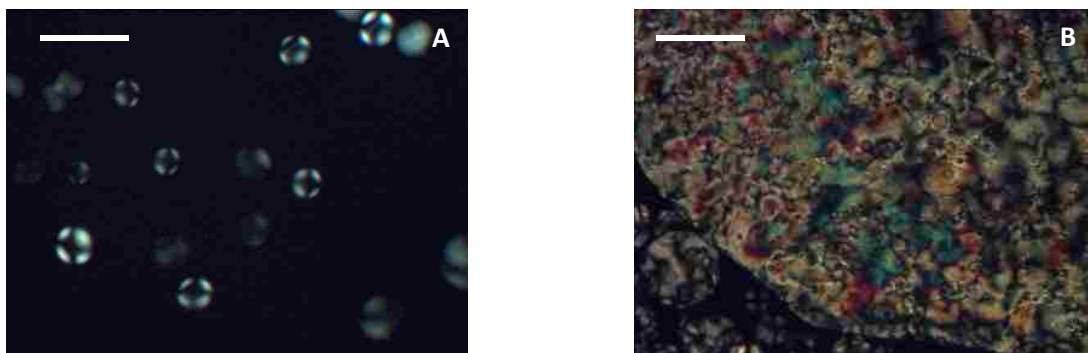
Figure 3.14 Comparison of 14 wt% PBLG with (A) 3 wt% and (B) 25 wt% hybrid particle. Scale bar is 150 microns.

3.3.3 Wide-Angle X-ray Scattering of Phase Behavior

To gain more information about the arrangement of PBLG and colloidal particles some samples from the phase behavior diagram were studied by wide-angle X-ray scattering. For PBLG liquid crystals in pyridine that have not been annealed, there is only one peak from the PBLG chain that falls in the q range of ~2-4 nm^{-1}, which corresponds to a d-spacing of ~3-1.5 nm. Figure 3.15 shows a series of PBLG liquid crystals at concentrations ranging from 18-40

71

wt%. PBLG (MW 100k) at a concentration of 18 wt% falls in the biphasic region, but samples in the higher concentrations of 32 and 40 wt% are uniformly crystalline. As concentration increases the peak moves to higher q values indicating that the rods are moving closer together. No higher-order reflections are resolvable past this initial peak. The large peak occurring at approximately $q=14$ nm^{-1} (d=0.45 nm) is attributed to the solvent.
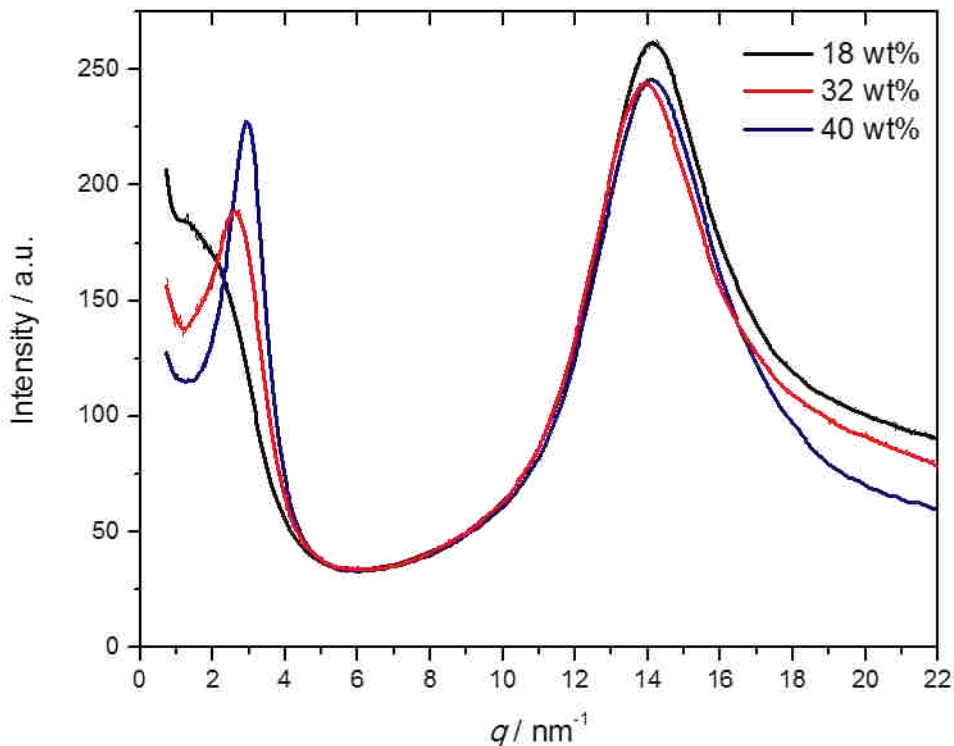
Figure 3.15 Wide-angle X-ray scattering of PBLG (100k MW) liquid crystal in pyridine at concentrations of 18, 32 and 40 wt%.

As mentioned previously in the discussion of phase behavior, the addition of particles lowers the concentration required to transition to the biphasic region. X-ray scattering of phase samples with similar PBLG concentrations, but differing in hybrid particle concentration, are shown in Figure 3.16. The sample containing 18 wt% PBLG and 4 wt% hybrid particle has a very broad peak centered at approximately $q=1$ nm^{-1} (if it were fully resolved), which gives a range of d-spacings much larger than the diameter of a single rod. This is similar to what is

observed for PBLG (18 wt%) liquid crystal without added particles in Figure 3.15 above. With particle concentration increased to 17 wt% a peak corresponding to a d-spacing of 1.6 nm forms, which is consistent with ordered PBLG. Some undulations are noticeable in the lower q-numbers, but they do not convincingly correspond to the hexagonal packing expected for PBLG, or any other commonly occurring lattice structure.

Three concentrations of hybrid particles from the phase diagram were measured and are shown in Figure 3.17. At 15 wt% the sample is isotropic and has no peak corresponding to a periodic PBLG pattern. At the higher concentrations of 29 wt% and 36 wt% the samples are biphasic which reveals that there is some interaction between the rods on the particle surface. At the highest concentration a peak at $q=3.1$ nm^{-1} ($d=2.0$ nm) reveals long range ordering similar to what is observed in a liquid crystal.
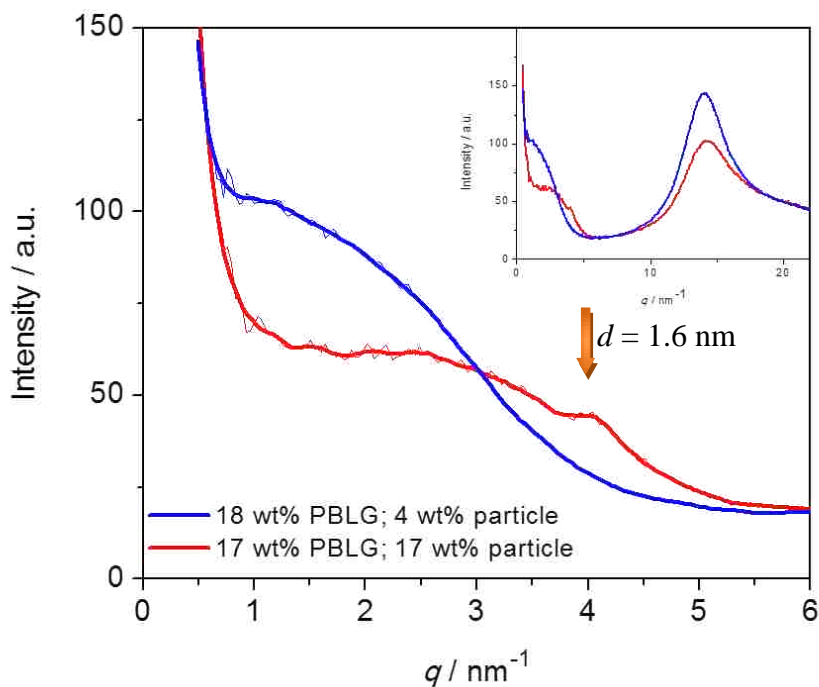
Figure 3.16 Wide-angle X-ray scattering of phase behavior samples at (blue) 18 wt% PBLG, 4 wt% hybrid particle and (red) 17 wt% PBLG, 17 wt% hybrid particle. The inset shows the full q-range including the solvent peak.
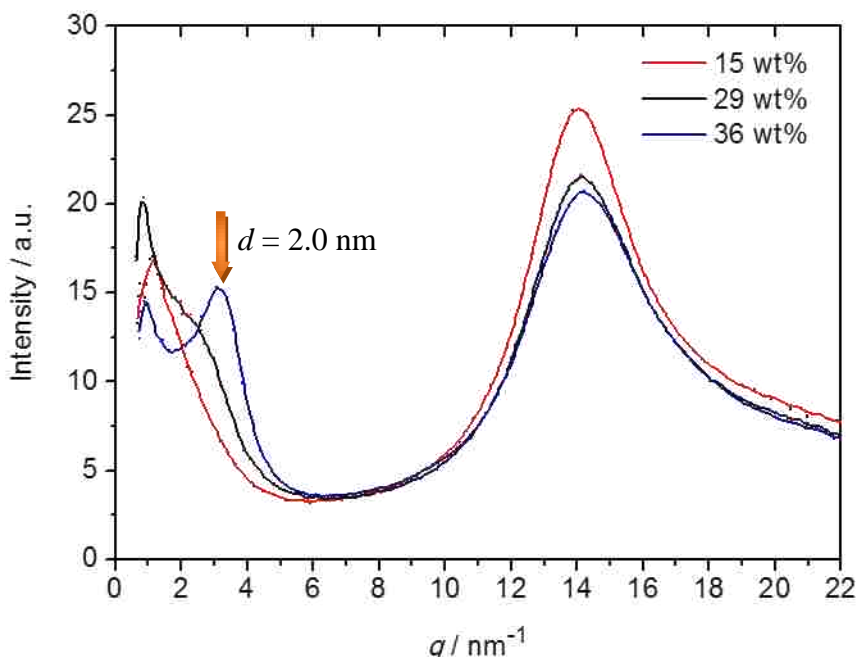
Figure 3.17 Wide-angle X-ray scattering of silica-PBLG hybrid particles in pyridine. Samples adapted from phase diagram with concentrations of 15, 29 and 36 wt%.

3.3.4 Jamming of Hybrid Particles

Silica-PBLG particles suspended in pyridine were placed in a capillary for X-ray scattering and centrifuged 30 minutes to concentrate the particles at the bottom of the capillary. The sample was viewed in the polarizing microscope for birefringence, which was observed at the most concentrated end. Moving upward, the sample became visually less concentrated and no longer birefringent. Samples were transported to CAMD in an upright position to discourage dilution.

Wide angle X-ray scattering measurements were made along the length of the capillary moving from the most concentrated end to the least (Figure 3.18). Scattering from the PBLG chain produces a peak corresponding to a d-spacing of 1.4 nm, which is the distance between rod centers, and a second broad peak with a d-spacing of 0.4 nm resulting from amorphous side chains.[97, 98] Peaks corresponding to the PBLG chain increase in intensity as the concentration increases indicating that the rods are closer to one another. The position of this peak is similar to

74

what is observed in a PBLG (40 wt%) liquid crystal in pyridine (Figure 3.15). At the high concentration the pendant groups may slightly overlap given the distance between rod centers is less than the width of a PBLG chain, which is 1.6 nm, and presence of a peak related to pitch that is not as visible in less concentrated regions or the liquid crystalline sample.[86]

Diffraction patterns provide some information about the order of the rods in solution. In Figure 3.19, the scattering ring from silica-PBLG is not as strong as the solvent ring, which is reflected by the relative intensity of the peaks in the scattering curve. Overall, the scattering
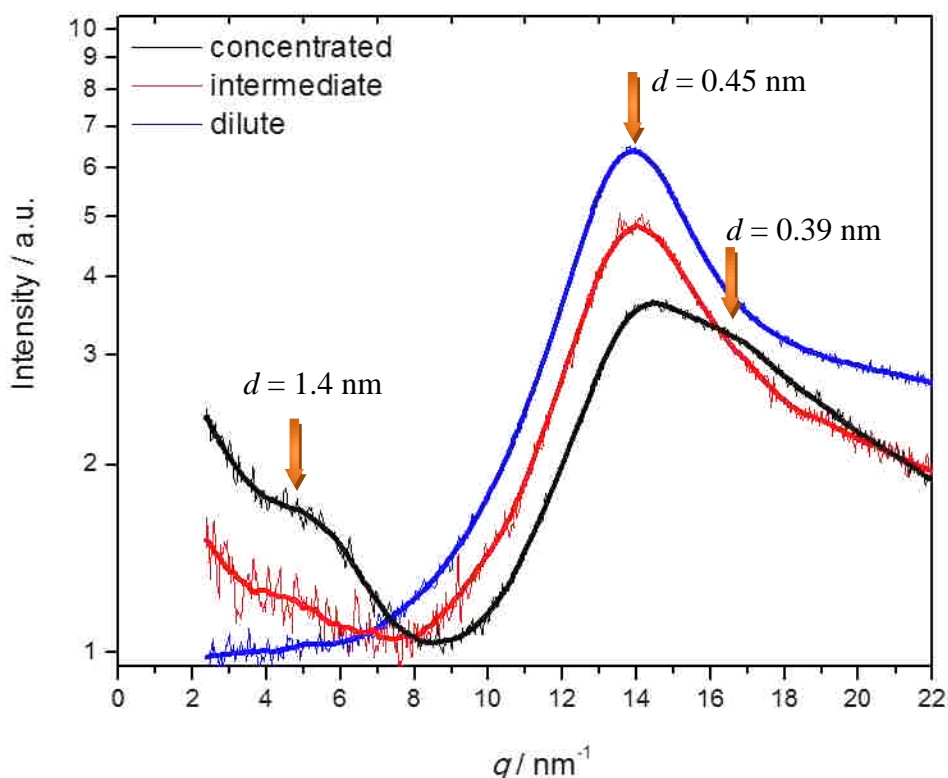
Figure 3.18 WAXS plot of centrifuged silica-polypeptide particles measured from highest to lowest concentration along the capillary. $R_g = 150$ nm (DLS).

intensity is weak, increasing the signal to noise, but the halo corresponding to PBLG is much more diffuse and lacks order compared to the liquid crystalline diffraction pattern. Jamming the particles together by force may have caused the polypeptides on the surface to arrange in a fashion similar to a liquid crystal, but force may be required to create this much interaction.

Based on the phase diagram presented earlier, hybrid particles in pyridine at the highest concentrations formed clusters of ordered domains but not the large, dense crystalline regions typical of a concentrated liquid crystalline phase.
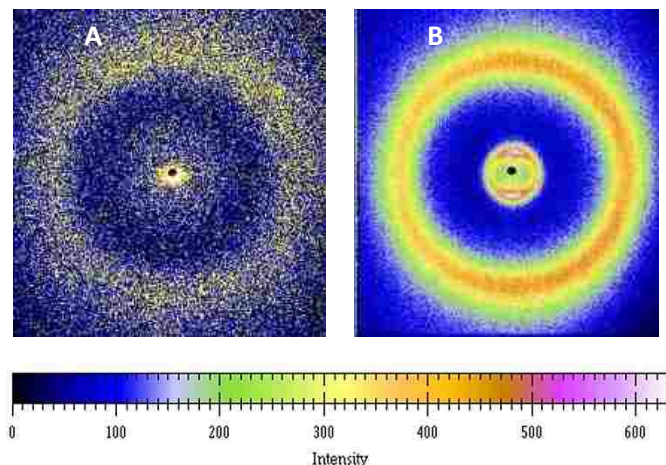
Figure 3.19 WAXS diffraction patterns from (A) the highest concentration of silica-PBLG particles and (B) a PBLG (40 wt%) liquid crystal in pyridine.

At high concentrations of hybrid particles, the exact positions of the PBLG chains attached to the silica are not easily resolved by microscopy or X-ray scattering. A schematic depicting the possible orientations are shown in Figure 3.20. As two particles approach each other the polymer chains can either interdigitate or bend away from the normal to the surface to form ordered domains. Although PBLG is rodlike at lengths of about 100 nm, there is potential for flexibility under force. Additionally, if PBLG is tilted as it grows from the surface this type of arrangement may be more easily achieved. In all cases, the curvature of the silica core would not allow the formation of long range order unless the particles could be packed into a crystalline arrangement or aligned into long chains.

3.3.5 Magnetic and Fluorescent Particles in Liquid Crystals

Magnetic silica particles respond to a magnetic field by forming linear chains in solution, but in liquid crystals their behavior can change. Theoretical work by de Gennes considered

Figure 3.20 Schematic representation of possible arrangements of PBLG chain attached to the silica surface.

whether the addition of magnetic particles to a nematic or cholesteric liquid crystal would enhance its magnetic susceptibility,[87] but particle aggregation at high concentrations produces a barrier to experimental studies of this concept.[88] The polypeptide shell of hybrid particles may provide some steric repulsion preventing large aggregates from forming. Phase behavior of hybrid particles described earlier in this chapter shows the ability of these particles to become enmeshed with the liquid crystal. Future studies would include phase behavior of magnetic and fluorescent hybrid particles in cholesteric or even nematic LCs. In this section are considered bare particles that are magnetic and fluorescent.

Silica particles with a magnetite core and diameter of 50 nm (the same as shown in Figure 3.7) were mixed with a PBLG LC at high concentrations. In Figure 3.21A the magnetic particles have spontaneously aggregated into a large structure with smooth edges on two of its sides. The liquid crystal accommodates large structures by reorienting around the obstacle instead of reverting to anisotropic state. Near the edges of the aggregate, cholesteric banding parallel to that edge gives the impression that interfacial tension is tolerated more easily in a configuration where polypeptides are anchored tangential to the silica surface. This change in orientation from the helical axis being perpendicular to a surface to parallel is also observed near the air-liquid crystal interface even if the bulk solution is oriented in a different direction (Figure 3.20B).[66, 89] The same type of interfacial tension between the ordered and isotropic phases also exists at spherulite boundaries.
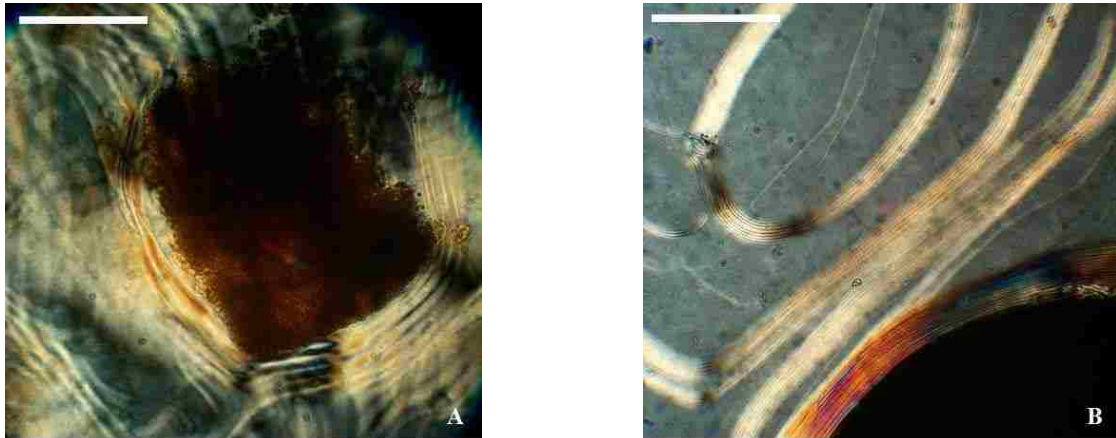
Figure 3.21 (A) 50-nm (diameter) magnetic silica particles in PBLG (MW 91k, L=62 nm) form a sharp boundary in the midst of the liquid crystal. (B) Air-solution interface of the liquid crystal showing uniform cholesteric banding. Scale bar is 100 microns.

In studying the flow behavior of PBLG LCs, Robinson observed that as the sample is tilted shearing forces caused a spherulite to draw into a cylindrical shape and become progressively thinner until it forms a birefringent thread between the two portions.[90] Similar behavior is shown in Figure 3.22. The shear forces here are applied by the movement of magnetic particles through the liquid crystal under a magnetic field and the edges of the projections end up intertwined with the aggregates. Robinson notes the retraction of the thread back into the spherulite, but in this case threads remain in place potentially due to gravitational
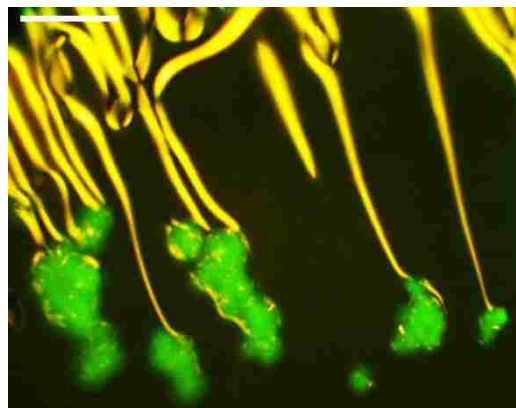
Figure 3.22 Combined polarized and fluorescence microscopy of fluorescent magnetic silica particles (50 nm diameter) in PBLG (91k, L=62 nm)/pyridine liquid crystal. A magnetic field was applied to this sample. Scale bar 100 microns.

forces if the sample cell is placed upright, but it may be pinned in this position by the presence of the particle aggregates. The image is the result of both fluorescence illumination and standard polarizing optical microscopy.

Fluorescent, magnetic silica particles at 1.4 wt% were mixed with PBLG liquid crystal (20 wt % PBLG in pyridine) to determine how a more dilute solution of particles would align under a magnetic field in a viscous liquid crystal. Figure 3.23 shows the sample after the particles are mixed with PBLG and pyridine. The fluorescence picture on the right is taken at the
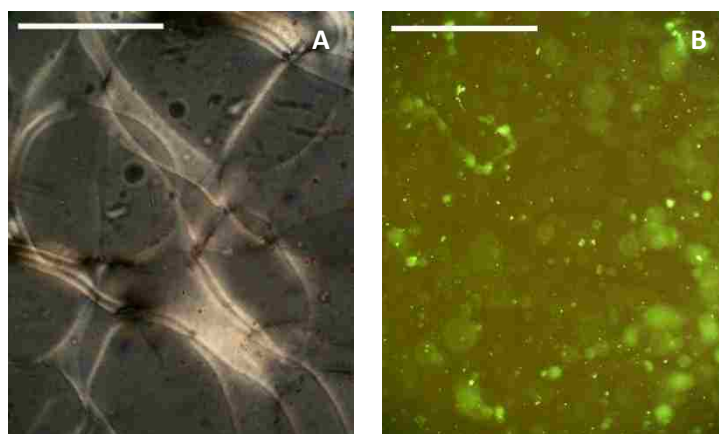
Figure 3.23 50-nm fluorescent, magnetic silica particles immersed in liquid crystalline PBLG (20 wt% in pyridine). Images are of the same position on the sample in (A) crossed POM and (B) fluorescence microscopy. Scale bar is 150 microns.

same magnification and sample location as the one on the left. Some particles appear in focus and others appear as hazy circles, which are most likely spheres out of focus due to the depth of the sample. The capillary tubes have an inside path length of 400 microns, which is thick enough to stack over 2000 silica particles so there is ample room for the particles to disperse throughout the liquid crystal. No particular alignment of the particles by the liquid crystal is observed.

The sample was placed above a 0.3 Tesla bar magnet (measured with an MD 1-ST DC Gaussmeter, AlphaLab, Inc.) where the magnetic field lines were parallel to the surface of the sample cell for approximately 10 minutes. The particles begin to form long chains that are not

linear, but curved along disclination lines in the liquid crystal as indicated by the blue oval in Figure 3.24 (images A and B). A different position of the sample is shown in Figure 3.24C where more particles are visible and the long, curved chains that result.
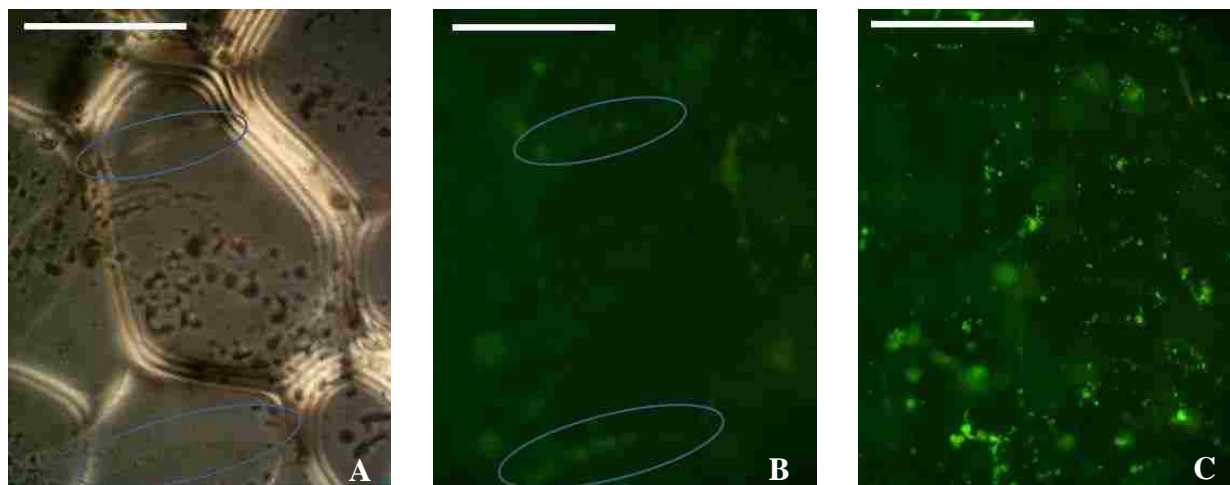
Figure 3.24 50-nm fluorescent, magnetic silica particles immersed in liquid crystalline PBLG (20 wt% in pyridine) after magnet has been applied. Images A and B are of the same position on the sample in crossed POM and fluorescence microscopy, respectively. Image C is fluorescence microscopy of the sample at a different position. Scale bar is 150 microns.

3.4 Thermal Phase Behavior of Poly(γ-stearyl-α-L-glutamate) (PSLG) Liquid Crystal

3.4.1 Introduction

PSLG liquid crystals were studied to understand their thermal behavior prior to the introduction of hybrid particles into the matrix, which will most likely lead to complex structures as observed in PBLG/hybrid particle systems. The most notable feature of PSLG, compared to other polypeptides, is the alkyl side group that adds functionality and structure to the polypeptide (Figure 3.25). The long, carbon side chains of PSLG increase the solubility of the polypeptide in nonpolar solvents and behave as solvating agents themselves when melted. PSLG displays both lyotropic and thermotropic properties, where liquid crystalline formation occurs upon increase in concentration or temperature, respectively. At low temperatures ordering occurs due to the side chains forming crystalline domains. As temperature increases, the entire polypeptide chain

orients into a crystalline structure.[91, 92] The α-helical nature of the backbone forces the side chains to fan outward in large spiral when the polypeptide is viewed axially. PSLG has a diameter of approximately 3.7 nm and the length varies according to molecular weight.[93]
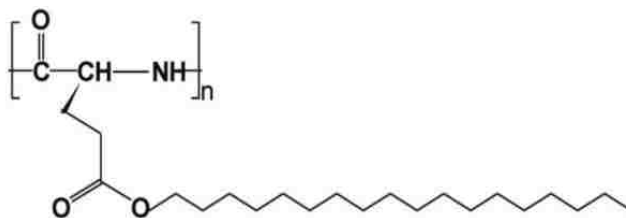
Figure 3.25 Chemical Structure of poly(γ-stearyl-α,L-glutamate).

3.4.2 Methods and Materials

PSLG (JP.1.9) with a molecular weight of 120k (L = 50 nm) was used for these studies. Toluene was purchased from Sigma-Aldrich and used as received. Liquid crystalline samples were prepared in Vitrodynamic cells and flame sealed, then viewed under polarized optical microscopy as previously described. Heating of the sample was performed using a Mettler (FP-80) microscopy hot stage equipped with a programmable thermostat.

3.4.3 Results and Discussion

Several concentrations of PSLG in toluene were prepared ranging from 17 to 31 wt%. Polarized optical microscopy of the sample, Figure 3.26, shows that cholesteric banding did not form immediately as in the case of PBLG/pyridine liquid crystals. It is not easy to discern which type of liquid crystal is present, but PSLG in toluene is expected to aggregate end to end, and may be exhibiting a smectic or nematic structure. As the sample was heated, it formed a cholesteric liquid crystal. Upon further heating of the sample to 111 °C, the boiling point of toluene, the cholesteric pitch decreased (Figure 3.27). This effect is opposite of what is observed in PBLG solutions.[94] Temperature was ramped down at a rate of a few degrees per minute, where
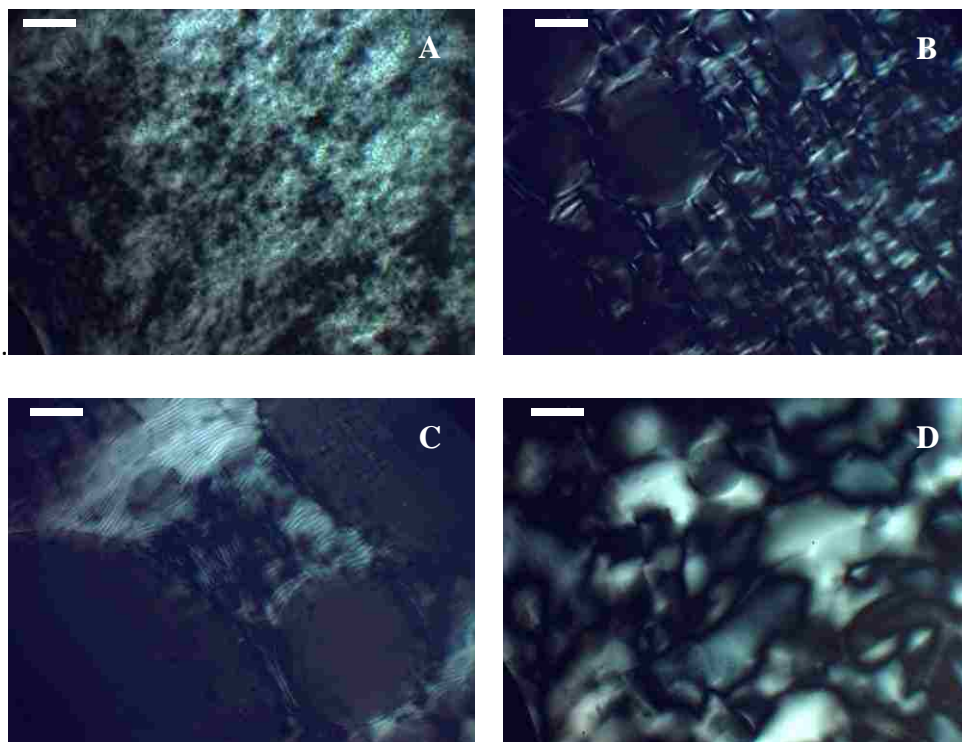
Figure 3.26 Polarized optical microscopy of PSLG in toluene at approximateely 25 wt% concentration. Sample temperature is inreased from room temperature to 120 °C, then allowed to cool. Pictures shown in this figure are of the LC at (a) 27 °C, (b) 93 °C, (c) 111 °C, then cooled down to (d) room temperature. Scale bar 200 microns.
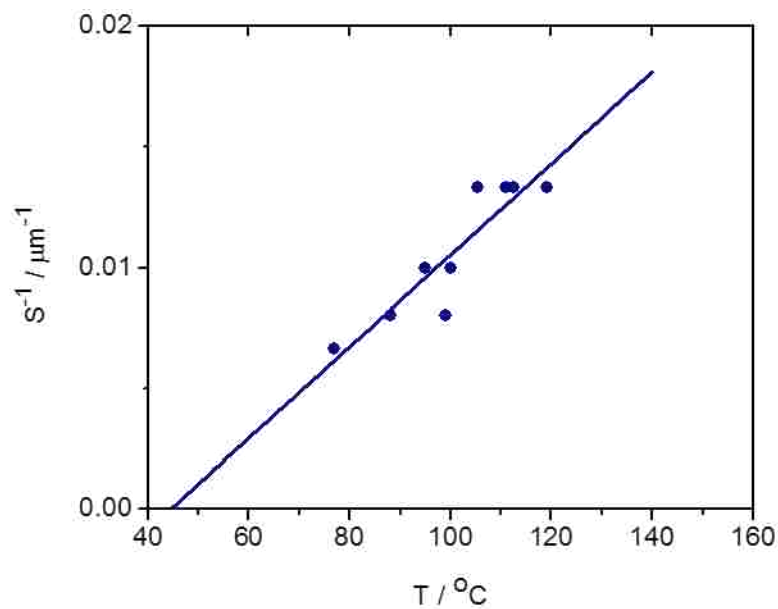
Figure 3.27 Pitch versus concentration for PSLG (MW 129k) in toluene.

increases in pitch were observed, then allowed to equilibrate to room temperature. The final structure of the liquid crystal closely resembles a nematic.

X-ray scattering shows that PSLG is hexagonally packed at room temperature. The peaks are spaced at the characteristic q-ratios of $1:\sqrt{3}:2:\sqrt{7}$, with the primary peak occurring at q=0.04 Å^{-1} (Figure 3.28). This corresponds to a hexagonal d-spacing ($d_{hex} = 2\pi/q \sin 60°$) of 180 Å, equivalent to the width of 5 PSLG chains. The position of the refections from the primary peak remain constant with each concentration. At q-values ranging from 0.15-0.2 Å (d = 36-48 Å) the peak height increases and shifts to higher q-values as the concentration increases indicating that the polymer rods are moving closer together. Change in d-spacing versus
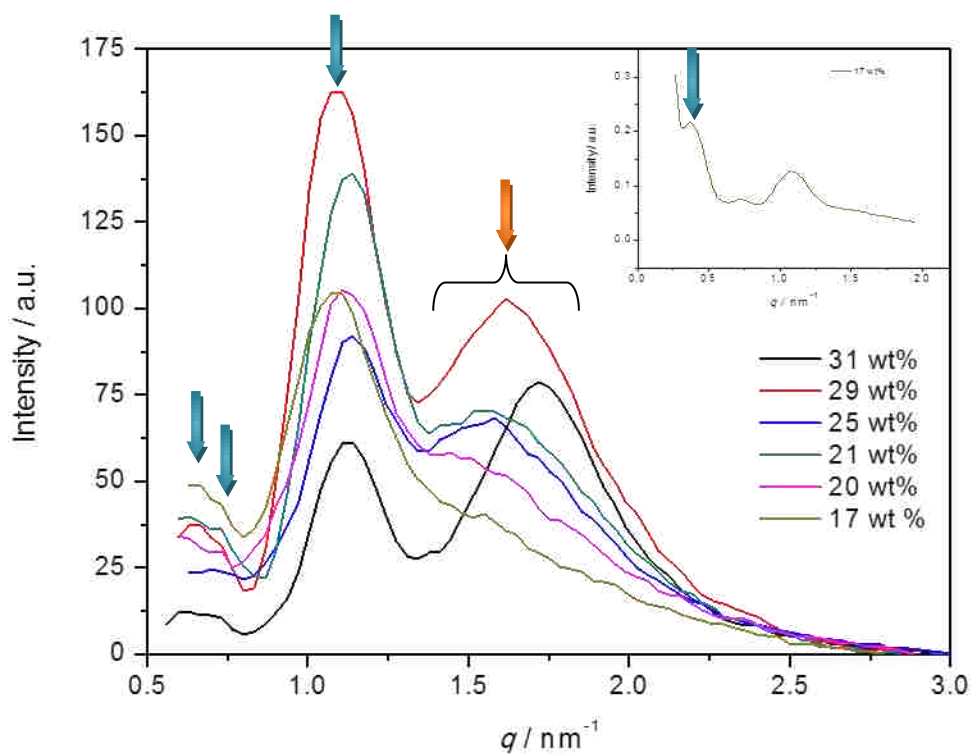
Figure 3.28 WAXS of PSLG (120k) in toluene at various concentrations. The inset shows the SAXS pattern with the primary peak at q = 0.04 nm^{-1}. The blue peaks identify the hexagonal packing of the rods in the ratio of $1:\sqrt{3}:2:\sqrt{7}$. The peaks in the range of 1.7-2.0 nm^{-1} ($d = 3.7$-4.2 nm) correspond to the center-to-center rod distance.

concentration gives a result that differs from PBLG. Robinson found that d $\propto$ c$^{-0.5}$ for PBLG in dioxane. In the case of PSLG in toluene the proportionality exponent is -0.3±0.05 (Figure 3.29).[95]
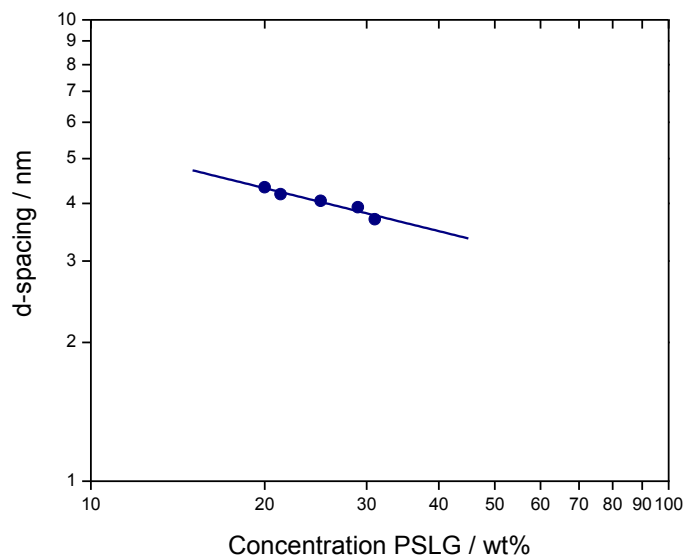
Figure 3.29 Log-log plot of *d*-spacing versus concentration for PSLG (120k) in toluene. The d-spacing is proportional to concentration to the power of -0.3±0.05.
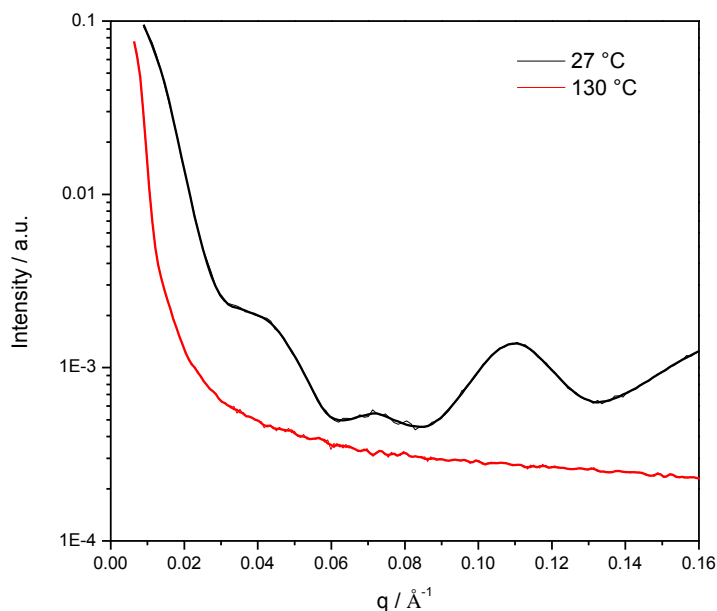
Figure 3.30 SAXS of PSLG-toluene (120k, L=51 nm) liquid crystal (29 wt%). The liquid crystal loses its original hexagonal packing features at high temperatures.

The change in structure of the liquid crystal is observed in SAXS. The sample was heated to approximately 130 °C in the sample chamber. The original hexagonal packing features of the room temperature sample disappear at temperature where the liquid crystal is known to be cholesteric. This scattering behavior is similar to that of cholesteric PBLG, which has no peaks in this q-range. This observation leads the possibility of aligning particles in a liquid crystal via changes in temperature.

3.5 Future Work

Several branches of this experiment can be explored, whether it is altering the hybrid particles in terms of size and surface functionality or changing the liquid crystalline media in which it is dispersed. Even the solvent choice affects the behavior of the liquid crystal and the particle. Eventually a range of phase behavior can be understood and targeted properties extracted as necessary for a desired outcome.

In this dissertation, hybrid particles were dispersed in a cholesteric liquid crystal. To gain information about the behavior of mesogens near a hybrid particle they can be immersed in a nematic crystalline phase. The chirality of the polypeptides on the surface should induce chirality in the surrounding media. Information regarding the extent of this deformation of the nematic would additionally shed some light on its exact behavior in a cholesteric, being that they are locally nematic.

Some of the particles used in this dissertation were magnetic, but not the hybrid particles themselves. Such particles do exist. Because of the dipole moment of the polypeptide it would be interesting to see the effects of a magnetic field (or electric field) on the magnetic particles in the liquid crystal. The coupled effect of both the magnetically oriented polypeptide and the oriented particle any produce a stronger response than either one individually.

Plans to develop Janus hybrid particles where one half of the particle is coated with polypeptides are underway. There exists the possibility that these particles will form liquid crystalline domains. Phase studies where the particles are immersed in liquid crystals should induce early formation of the liquid crystalline phase based on results presented in this dissertation. Additionally, these particles may have interesting features in a liquid crystalline matrix where one side of the particle displays a different type of LC interaction than the other.[96]

3.6 References

1.   Flory, P. J. Statistical Thermodynamics of Mixtures of Rodlike Particles. 5. Mixtures with Random Coils. *Macromolecules* 1978, 11, (6), 1138-1141.

2.   Flory, P., Molecular theory of liquid crystals. In *Liquid Crystal Polymers I*, 1984; pp 1-36.

3.   Onsager, L. The Effects of Shape on the Interaction of Colloidal Particles. *Annals of the New York Academy of Sciences* 1949, 51, (Molecular Interaction), 627-659.

4.   Dogic, Z.; Fraden, S., Phase Behavior of Rod-Like Viruses and Virus-Sphere Mixtures. In *Soft Matter: Complex Colloidal Suspensions*, Wiley-VCH: 2006; Vol. 2, pp 1-78.

5.   Khokhlov, A. R.; Semenov, A. N. On the theory of liquid-crystalline ordering of polymer chains with limited flexibility. *J Stat Phys* 1985, 38, (1-2), 161-182.

6.   Stroobants, A.; Lekkerkerker, H. N. W.; Odijk, T. Effect of electrostatic interaction on the liquid crystal phase transition in solutions of rodlike polyelectrolytes. *Macromolecules* 1986, 19, (8), 2232-2238.

7.   Dogic, Z.; Fraden, S., Phase behavior of rod-like virus and polymer mixtures. In *arXiv preprint cond-mat/0010269*, 2000; pp 1-21.

8.   Onsager, L. Minutes of the Meeting of the New England Section held at Hartford, Connecticut, October 24, 1942. *Physical Review* 1942, 62, (11-12), 558-559.

9.   Asakura, S.; Oosawa, F. On Interaction between Two Bodies Immersed in a Solution of Macromolecules. *The Journal of Chemical Physics* 1954, 22, (7), 1255-1256.

10.   Asakura, S.; Oosawa, F. Interaction between Particles Suspended in Solutions of Macromolecules. *J. Polym. Sci.* 1958, 33, 183-192.

11. Gogelein, C.; Nagele, G.; Buitenhuis, J.; Tuinier, R.; Dhont, J. K. G. Polymer depletion-driven cluster aggregation and initial phase separation in charged nanosized colloids. *The Journal of Chemical Physics* 2009, 130, (20), 204905-15.

12. Koenderink, G. H.; Vliegenthart, G. A.; Kluijtmans, S. G. J. M.; van Blaaderen, A.; Philipse, A. P.; Lekkerkerker, H. N. W. Depletion-Induced Crystallization in Colloidal Rod-Sphere Mixtures. *Langmuir* 1999, 15, (14), 4693-4696.

13. Mao, Y.; Cates, M. E.; Lekkerkerker, H. N. W. Depletion force in colloidal systems. *Physica A: Statistical and Theoretical Physics* 1995, 222, (1-4), 10-24.

14. Martınez-Ratón, Y.; Cinacchi, G.; Velasco, E.; Mederos, L. Depletion effects in smectic phases of hard-rod-hard-sphere mixtures. *The European Physical Journal E: Soft Matter and Biological Physics* 2006, 21, (2), 175-188.

15. Roth, R. Depletion potentials in colloidal mixtures of spheres and rods. *Journal of Physics: Condensed Matter* 2003, 15, (1), S277.

16. Roth, R.; König, P. The depletion potential in one, two and three dimensions. *Pramana* 2005, 64, (6), 971-980.

17. Seebergh, J. E.; Berg, J. C. Depletion flocculation of aqueous, electrosterically-stabilized latex dispersions. *Langmuir* 1994, 10, (2), 454-463.

18. Vliegenthart, G. A.; van der Schoot, P. Kinetics of depletion interactions. *Europhys. Lett.* 2003, 62, (4), 600-606.

19. Yaman, K.; Jeppesen, C.; Marques, C. M. Depletion forces between two spheres in a rod solution. *Europhys. Lett.* 1998, 42, (2), 221-226.

20. Ye, X.; Narayanan, T.; Tong, P.; Huang, J. S.; Lin, M. Y.; Carvalho, B. L.; Fetters, L. J. Depletion interactions in colloid-polymer mixtures. *Physical Review E* 1996, 54, (6), 6500.

21. Oversteegen, S. M.; Wijnhoven, J. G. E. J.; Vonk, C.; Lekkerkerker, H. N. W. Crystallization Kinetics and Morphology in Phase Separating and Sedimenting Mixtures of Colloidal Spheres and Rods. *The Journal of Physical Chemistry B* 2004, 108, (47), 18158-18163.

22. Lin, E. K.; Gast, A. P. Self Consistent Field Calculations of Interactions between Chains Tethered to Spherical Interfaces. *Macromolecules* 1996, 29, (1), 390-397.

23. Oversteegen, S. M.; Lekkerkerker, H. N. W. On the accuracy of the Derjaguin approximation for depletion potentials. *Physica A: Statistical Mechanics and its Applications* 2004, 341, 23-39.

24.   Purdy; et al. Nematic Phase Transitions in Mixtures of Thin and Thick Colloidal Rods. *Physical Review Letters* 2005, 94, (5).

25.   Fraden, S.; et al. Nematic-nematic phase separation in binary mixtures of thick and thin hard rods: Results from Onsager-like theories. *Physical Review E* 2005, 72, (5), 051704.

26.   Galindo, A.; Haslam, A. J.; Varga, S.; Jackson, G.; Vanakaras, A. G.; Photinos, D. J.; Dunmur, D. A. The phase behavior of a binary mixture of rodlike and disclike mesogens: Monte Carlo simulation, theory, and experiment. *The Journal of Chemical Physics* 2003, 119, (10), 5216-5225.

27.   Dogic, Z.; Fraden, S. Smectic Phase in a Colloidal Suspension of Semiflexible Virus Particles. *Physical Review Letters* 1997, 78, (12), 2417.

28.   Dogic, Z.; Fraden, S. Cholesteric Phase in Virus Suspensions. *Langmuir* 2000, 16, (20), 7820-7824.

29.   Dogic, Z.; Purdy, K. R.; Grelet, E.; Adams, M.; Fraden, S. Isotropic-nematic phase transition in suspensions of filamentous virus and the neutral polymer Dextran. *Physical Review E* 2004, 69, (5).

30.   Dogic, Z.; Fraden, S. Ordered phases of filamentous viruses. *Current Opinion in Colloid & Interface Science* 2006, 11, (1), 47-55.

31.   Adams, M.; Fraden, S. Phase Behavior of Mixtures of Rods (Tobacco Mosaic Virus) and Spheres (Polyethylene Oxide, Bovine Serum Albumin). *Biophysical Journal* 1998, 74, (1), 669-677.

32.   Grelet, E.; Fraden, S. What Is the Origin of Chirality in the Cholesteric Phase of Virus Suspensions? *Physical Review Letters* 2003, 90, (19), 198302.

33.   Purdy, K. R.; Fraden, S. Influence of charge and flexibility on smectic phase formation in filamentous virus suspensions. *Physical Review E* 2007, 76, (1), 011705.

34.   Tang, J.; Fraden, S. Isotropic-cholesteric phase transition in colloidal suspensions of filamentous bacteriophage. *Liquid Crystals* 1995, 19, (4), 459 - 467.

35.   Lang, P. R. Depletion interaction mediated by polydisperse rods. *The Journal of Chemical Physics* 2007, 127, (12), 124906-6.

36.   Adams, M.; Dogic, Z.; Keller, S. L.; Fraden, S. Entropically driven microphase transitions in mixtures of colloidal rods and spheres. *Nature* 1998, 393, (6683), 349.

37.   Zhou, J.; van Duijneveldt, J. S.; Vincent, B. The Phase Behavior of Dispersions of Silica Particles in Mixtures of Polystyrene and Dimethylformamide. *Langmuir* 2010.

38.   Monovoukas, Y.; Gast, A. P. The experimental phase diagram of charged colloidal suspensions. *Journal of Colloid and Interface Science* 1989, 128, (2), 533-548.

39.   Beck-Candanedo, S.; Viet, D.; Gray, D. G. Partitioning of charged and neutral dextran-dye derivatives in biphasic cellulose nanocrystal suspensions. *Canadian Journal of Chemistry* 2008, 86, (6), 503-511.

40.   Beck-Candanedo, S.; Viet, D.; Gray, D. G. Triphase Equilibria in Cellulose Nanocrystal Suspensions Containing Neutral and Charged Macromolecules. *Macromolecules* 2007, 40, (9), 3429-3436.

41.   Fasolo, M.; Sollich, P. Effects of polymer polydispersity on the phase behaviour of colloid-polymer mixtures. *Journal of Physics: Condensed Matter* 2005, 17, (6), 797.

42.   Cooke, D. M.; Shi, A.-C. Effects of Polydispersity on Phase Behavior of Diblock Copolymers. *Macromolecules* 2006, 39, (19), 6661-6671.

43.   Bladon, P.; Frenkel, D. Simulating polymer liquid crystals. *Journal of Physics: Condensed Matter* 1996, 8, (47), 9445.

44.   Dijkstra, M.; Frenkel, D. Simulation study of the isotropic-to-nematic transitions of semiflexible polymers. *Physical Review E* 1995, 51, (6), 5891.

45.   Dijkstra, M.; et al. Phase behaviour and structure of model colloid-polymer mixtures. *Journal of Physics: Condensed Matter* 1999, 11, (50), 10079.

46.   Antypov, D.; Cleaver, D. J. The role of attractive interactions in rod-sphere mixtures. *Journal of Chemical Physics* 2004, 120, (21), 10307-10316.

47.   van der Schoot, P.; Odijk, T. Statistical theory and structure factor of a semidilute solution of rodlike macromolecules interacting by van der Waals forces. *The Journal of Chemical Physics* 1992, 97, (1), 515-524.

48.   Lekkerkerker, H. N. W.; Stroobants, A. Phase behaviour of rod-like colloid+flexible polymer mixtures. *Il Nuovo Cimento D* 1994, 16, (8), 949-962.

49.   Dean, C. W.; Alice, P. G. Properties of crystallizing soft sphere systems. *Journal of Physics: Condensed Matter* 1999, 11, (50), 10133.

50.   Gast, A. P.; Hall, C. K.; Russel, W. B. Polymer-Induced Phase Separations in Nonaqueous Colloidal Suspensions. *J. Colloid Interface Sci.* 1983, 96, 251-267.

51.   Gast, A. P.; Russel, W. B.; Hall, C. K. An Experimental and Theoretical Study of Phase Transitions in the Polystyrene Latex and Hydroxyethylcellulose System. *J. Colloid Interface Sci.* 1986, 109, 161.

52. Gast, A. P.; Russel, W. B. Simple ordering in complex fluids. *Physics Today* 1998, 51, (12), 24.

53. Reznikov, Y.; Buchnev, O.; Tereshchenko, O.; Reshetnyak, V.; Glushchenko, A.; West, J. Ferroelectric nematic suspension. *Applied Physics Letters* 2003, 82, (12), 1917-1919.

54. Kurochkin, O.; Buchnev, O.; Iljin, A.; Park, S. K.; Kwon, S. B.; Grabar, O.; Yu, R. A colloid of ferroelectric nanoparticles in a cholesteric liquid crystal. *Journal of Optics A: Pure and Applied Optics* 2009, 11, (2), 024003.

55. Neeraj; Kumar, P.; Raina, K. K. Changes in the electro-optical behaviour of ferroelectric liquid crystal mixture via silica nanoparticles doping. *Optical Materials* 2012, 34, (11), 1878-1884.

56. Neeraj; Raina, K. Influence of silica nanoparticles on dielectric spectroscopy and polarization switching responses of novel ferroelectric liquid crystals. *Phase Transitions* 2010, 83, (8), 615-626.

57. Hu, W.; Zhao, H.; Shan, L.; Song, L.; Cao, H.; Yang, Z.; Cheng, Z.; Yan, C.; Li, S.; Yang, H. Magnetite nanoparticles/chiral nematic liquid crystal composites with magnetically addressable and magnetically erasable characteristics. *Liquid Crystals* 2010, 37, (5), 563-569.

58. Hung, F. R.; Bale, S. Faceted nanoparticles in a nematic liquid crystal: defect structures and potentials of mean force. *Molecular Simulation* 2009, 35, (10), 822 - 834.

59. Lagerwall, J. P. F.; Scalia, G. A new era for liquid crystal research: Applications of liquid crystals in soft matter nano-, bio- and microtechnology. *Current Applied Physics* 2012, 12, (6), 1387-1412.

60. Matsuyama, A.; Hirashima, R. Phase separations in liquid crystal-colloid mixtures. *The Journal of Chemical Physics* 2008, 128, (4), 044907-11.

61. Matsuyama, A. Phase separations in mixtures of a liquid crystal and a nanocolloidal particle. *Journal of Chemical Physics* 2009, 131, (20).

62. Shivakumar, U.; Mirzaei, J.; Feng, X.; Sharma, A.; Moreira, P.; Hegmann, T. Nanoparticles: complex and multifaceted additives for liquid crystals. *Liquid Crystals* 2011, 38, (11-12), 1495-1514.

63. Ravnik, M.; Alexander, G. P.; Yeomans, J. M.; Žumer, S. Three-dimensional colloidal crystals in liquid crystalline blue phases. *Proceedings of the National Academy of Sciences* 2011.

64. Jampani, V. S. R.; Škarabot, M.; Ravnik, M.; Čopar, S.; Žumer, S.; Muševič, I. Colloidal entanglement in highly twisted chiral nematic colloids: Twisted loops, Hopf links, and trefoil knots. *Physical Review E* 2011, 84, (3), 031703.

65. Ravnik, M.; Alexander, G. P.; Yeomans, J. M.; Zumer, S. Mesoscopic modelling of colloids in chiral nematics. *Faraday Discussions* 2010, 144, (0), 159-169.

66. Hijnen, N.; Wood, T. A.; Wilson, D.; Clegg, P. S. Self-Organization of Particles with Planar Surface Anchoring in a Cholesteric Liquid Crystal. *Langmuir* 2010, 26, (16), 13502-13510.

67. Zapotocky, M.; Ramos, L.; Poulin, P.; Lubensky, T. C.; Weitz, D. A. Particle-Stabilized Defect Gel in Cholesteric Liquid Crystals. *Science* 1999, 283, (5399), 209-212.

68. Chepikov, A.; Minenko, S.; Lisetski, L.; Lebovka, N. I.; U sol'tseva, N. V.; Soskin, M. S. Dispersions of carbon nanotubes and organomodified clay platelets in cholesteric liquid crystals. *Functional materials* 2012, 19, (3), 343-347.

69. Lintuvuori, J. S.; Stratford, K.; Cates, M. E.; Marenduzzo, D. Colloids in Cholesterics: Size-Dependent Defects and Non-Stokesian Microrheology. *Physical Review Letters* 2010, 105, (17), 178302.

70. Lintuvuori, J. S.; Marenduzzo, D.; Stratford, K.; Cates, M. E. Colloids in liquid crystals: a lattice Boltzmann study. *Journal of Materials Chemistry* 2010, 20, (46), 10547-10552.

71. Cleaver, J.; Poon, W. C. K. Network formation in colloid–liquid crystal mixtures studied by confocal microscopy. *Journal of Physics: Condensed Matter* 2004, 16, (19), S1901.

72. Meeker, S. P.; Poon, W. C. K.; Crain, J.; Terentjev, E. M. Colloid–liquid-crystal composites: An unusual soft solid. *Physical Review E* 2000, 61, (6), R6083-R6086.

73. West, J. L.; Zhang, K.; Glushchenko, A.; Andrienko, D.; Tasinkevych, M.; Reznikov, Y. Colloidal particles at a nematic-isotropic interface: Effects of confinement. *The European Physical Journal E* 2006, 20, (2), 237-242.

74. Venugopal, E.; Bhat, S. K.; Vallooran, J. J.; Mezzenga, R. Phase Behavior of Lipid–Based Lyotropic Liquid Crystals in Presence of Colloidal Nanoparticles. *Langmuir* 2011, 27, (16), 9792-9800.

75. Soto-Cantu, E. Synthesis and Surface Characterization of Silica-Polypeptide Composite Particles. Dissertation, Louisiana State University, Baton Rouge, 2008.

76. Soto-Cantu, E.; Turksen-Selcuk, S.; Qiu, J.; Zhou, Z.; Russo, P. S.; Henk, M. C. Silica−Polypeptide Composite Particles: Controlling Shell Growth. *Langmuir* 2010, 26, (19), 15604-15613.

77. Fong, B.; Russo, P. S. Organophilic Colloidal Particles with a Synthetic Polypeptide Coating. *Langmuir* 1999, 15, (13), 4421-4426.

78. Fong, B.; Turksen, S.; Russo, P. S.; Stryjewski, W. Colloidal Crystals of Silica-Homopolypeptide Composite Particles. *Langmuir* 2004, 20, (1), 266-269.

79. Stöber, W.; Fink, A.; Bohn, E. Controlled growth of monodisperse silica spheres in the micron size range. *Journal of Colloid and Interface Science* 1968, 26, (1), 62-69.

80. Balamurugan, S. S.; Soto-Cantu, E.; Cueto, R.; Russo, P. S. Preparation of Organosoluble Silica-Polypeptide Particles by "Click" Chemistry. *Macromolecules* 2010, 43, (1), 62-70.

81. Crocker, J. C.; Matteo, J. A.; Dinsmore, A. D.; Yodh, A. G. Entropic Attraction and Repulsion in Binary Colloids Probed with a Line Optical Tweezer. *Physical Review Letters* 1999, 82, (21), 4352-4355.

82. Mao, Y.; Cates, M. E.; Lekkerkerker, H. N. W. Theory of the depletion force due to rodlike polymers. *The Journal of Chemical Physics* 1997, 106, (9), 3721-3729.

83. Robinson, C. Liquid-crystalline structures in polypeptide solutions. *Tetrahedron* 1961, 13, (1-3), 219-234.

84. Kosmulski, M.; Eriksson, P.; Brancewicz, C.; Rosenholm, J. B. Zeta potentials of monodispersed, spherical silica particles in mixed solvents as a function of cesium chloride concentration. *Colloids and Surfaces A: Physicochemical and Engineering Aspects* 2000, 162, (1-3), 37-48.

85. Wakabayashi, N.; Yamanaka, J.; Murai, M.; Ito, K.; Sawada, T.; Yonese, M. Three-Dimensional Centimeter-Sized Colloidal Silica Crystals Formed by Addition of Base. *Langmuir* 2006, 22, (18), 7936-7941.

86. Bu, Z.; Russo, P. S.; Tipton, D. L.; Negulescu, I. I. Self-Diffusion of Rodlike Polymers in Isotropic Solutions. *Macromolecules* 1994, 27, (23), 6871-6882.

87. Brochard, F.; De Gennes, P. G. Theory of magnetic suspensions in liquid crystals. *Journal de Physique* 1970, 31, (7), 691-708.

88. Buluy, O.; Ouskova, E.; Reznikov, Y.; Glushchenko, A.; West, J.; Reshetnyak, V. Magnetically induced alignment of FNS. *Journal of Magnetism and Magnetic Materials* 2002, 252, (0), 159-161.

89. Pawsey, A. C.; Lintuvuori, J. S.; Wood, T. A.; Thijssen, J. H. J.; Marenduzzo, D.; Clegg, P. S. Colloidal particles at the interface between an isotropic liquid and a chiral liquid crystal. *Soft Matter* 2012, 8, (32), 8422-8428.

90. Robinson, C. Liquid-crystalline structures in solutions of a polypeptide. *Transactions of the Faraday Society* 1956, 52, 571-592.

91. Daly William, H.; Negulescu Ioan, I.; Russo Paul, S.; Poche Drew, S., Side-Chain Crystallinity and Thermal Transitions in Thermotropic Liquid-Crystalline Poly(γ-alkyl-α,L-glutamate)s. In *Macromolecular Assemblies in Polymeric Systems*, American Chemical Society: 1992; Vol. 493, pp 292-299.

92. Poche, D. S.; Daly, W. H.; Russo, P. S. Synthesis and Some Solution Properties of Poly(γ-stearyl-α,L-glutamate). *Macromolecules* 1995, 28, (20), 6745-6753.

93. Jamil, T.; Russo, P. S.; Negulescu, I.; Daly, W. H.; Schaefer, D. W.; Beaucage, G. Light scattering from random coils dispersed in a solution of rodlike polymers. *Macromolecules* 1994, 27, (1), 171-178.

94. Uematsu, I.; Uematsu, Y., Polypeptide liquid crystals. In *Liquid Crystal Polymers I*, 1984; pp 37-73.

95. Robinson, C.; Ward, J. C.; Beevers, R. B. Liquid crystalline structure in polypeptide solutions. Part 2. *Discussions of the Faraday Society* 1958, 25, 29-42.

96. Conradi, M.; Ravnik, M.; Bele, M.; Zorko, M.; Žumer, S.; Muševič, I. Janus nematic colloids. *Soft Matter* 2009, 5, (20), 3905-3912.

97. Papadopoulos, P.; Floudas, G.; Klok, H. A.; Schnell, I.; Pakula, T. Self-Assembly and Dynamics of Poly(γ-benzyl-L-glutamate) Peptides. *Biomacromolecules* 2003, 5, (1), 81-91.

98. Tang, H.; Zhang, D. Poly(γ-benzyl-L-glutamate)-functionalized single-walled carbon nanotubes from surface-initiated ring-opening polymerizations of N-carboxylanhydride. *Journal of Polymer Science Part A: Polymer Chemistry* 2010, 48, (11), 2340-2350.

CHAPTER 4. MODELING OF CORE-SHELL PARTICLES

4.1 Introduction

Overcoming the challenge of having to synthesize every possible sample needed to understand a phenomenon is typically accomplished using simulation techniques. In developing a model some assumptions must be made to simplify the system. The surface density of a core-shell particle in a real system varies depending on both the size of the core and the amount of polymer included in the shell, but can be approximated assuming the spacing of the polypeptide chains is equidistant.[1, 2] Another important assumption is that the polypeptide chains extend outward normal to the surface of the silica core.

The HYDRO++ Program (Version 10, 2011)[3, 4] uses a bead model to calculate the hydrodynamic properties of a particle or molecule. Several programs have been developed by Garcia de la Torre,[5] but this program seemed most suitable to generate a model of a unique structure such as a hybrid particle. The user constructs a model of the particle and inputs a set of coordinates and bead radii to the program. Solution properties such as solvent viscosity, density and temperature are entered. Particle or polymer specifications are required as well, including molecular weight and specific volume. The bead model can be visualized using a free VRML (Virtual Reality Modeling Language) viewing program produced by Cortona3D (Dublin, Ireland), which has been integrated into HYDRO++. The Cortona3D viewer operates inside of an internet browser window such as Firefox.

There are two options for running the program: the first uses a DOS console and the second is a graphic user interface (GUI), WinHydro, recently developed by Garcia de la Torre.[3] In the DOS window, the HYDRO++ program is called and requires input of a .txt file that contains the parameters of the model being studied. WinHydro (Figure 4.1) inputs the same

information as the text file and comparison of its output results to the DOS version leads to no discernible difference.
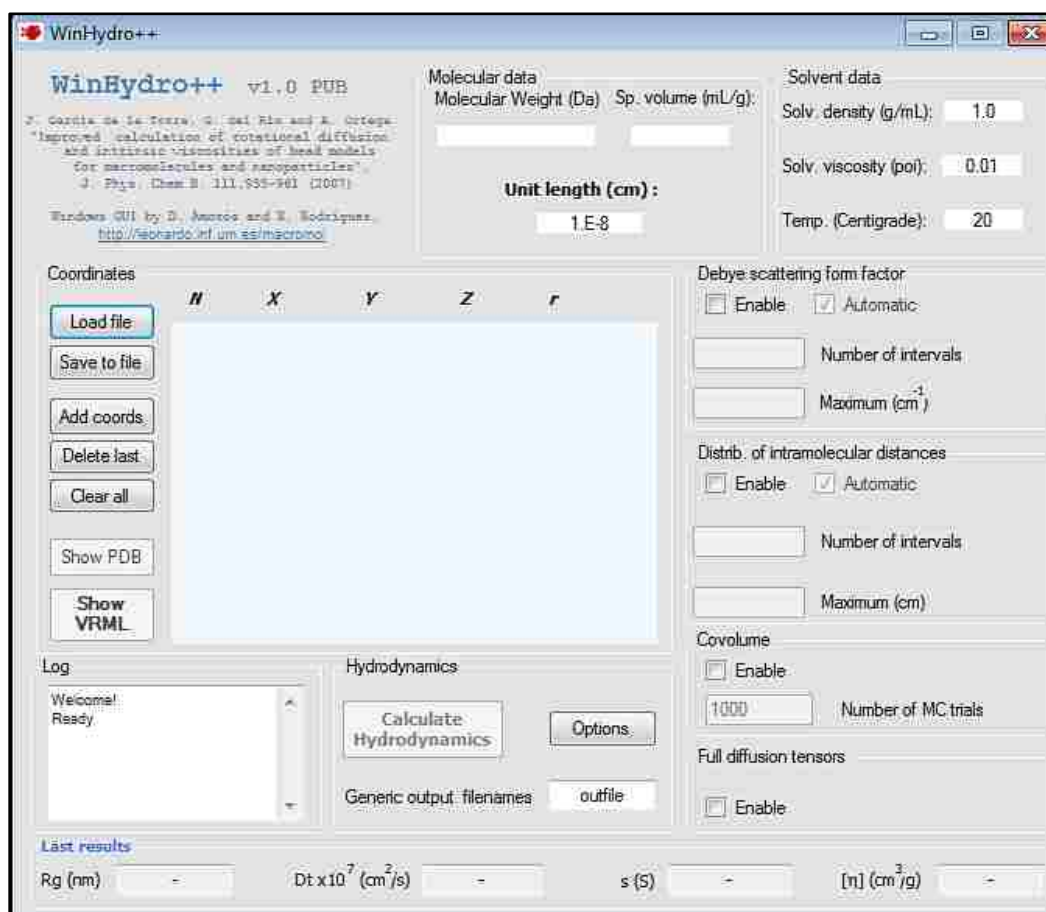

Figure 4.1 WinHydro user interface screen. Information is entered into the boxes and the results are displayed at the bottom of the window.

The HYDRO++ program employs three types of hydrodynamic calculations, referred to as "ICASE", that can be chosen by the user. The least demanding in terms of computing time is the Kirkwood-Riseman (ICASE 12) method which employs a modified Oseen tensor and volume correction for rotational properties, R_g, and intrinsic viscosity.[6-8] Third-order hydrodynamic interactions (ICASE 20) replace the Oseen tensor with one developed Garcia de la Torre and Bloomfield, but this calculation method has some limitations and is not capable of accurate determination of intrinsic viscosity. The most computationally demanding and the most accurate,

according to Garcia de la Torre, is the cubic substitution method which does not require any type of corrective measures. This method substitutes each bead with a cubic array of 4 beads, which provides better characterization of the friction forces felt by the surface of the bead.[3]

The user selects the range of q-values to be calculated for the form factor and the number of points desired for the pair distribution function. A series of output files are generated including a text file containing the results and a VRML file to visualize the bead model. A protein data bank file and ASCII file are also available, but are not used here. A default option is available where the program selects a q-range, but this range did not provide a range large enough to see core-shell effects.

4.2 Results and Discussion

4.2.1 Linear PBLG Chain

A simple PBLG chain was chosen as the first polymer to characterize given that its hydrodynamic properties were previously determined by this group.[9, 10] The values taken from publication are the molecular weight of the chain at 232k, giving a length of 160 nm, and the

Table 4.1 Input text for HYDRO++. The column on the left contains the changeable parameters and the column on the right contains the corresponding description.

PBLG chain	Title
12-PBLGchain	Filename for output files
PBLGchaincoo.txt	Structural (bead coordinates) file
12	ICASE
20	Temperature, centigrade
0.00879	Solvent viscosity
232000	Molecular weight
0.791	Specific volume of macromolecule
0.98	Solution density
51	Number of values of H
2×10^{7}	HMAX
30	Number of intervals for the distance distribution
8.0×10^{-7}	RMAX
10000	(only if ISCA is not zero) NTRIALS

diameter of the chain at 1.6 nm. The remainder of the information from the input file is listed in Table 4.1. A list of bead coordinates is also required for input and they were given using 3-dimensional Cartesian coordinates.
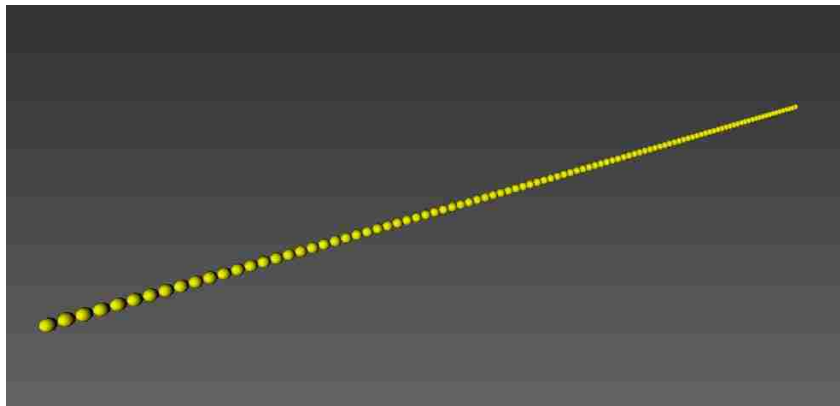

Figure 4.2 Cortona3D rendering of bead model for the PBLG chain. Diameter: 1.6 nm, Length 160 nm.

The run time for the program is only a few seconds for a few hundred beads, but if the number of beads is increased to the thousands then the time increases to a few minutes. The output files include the visualized bead model (Figure 4.1), and a text file containing the calculated results (Table 4.2). The translational diffusion coefficient determined by HYDRO++ is 1.562×10^{-7} cm^2/s (R_h = 15.6 nm), which is close to the reported value of $1.46 \pm 0.03 \times 10^{-7}$ cm^2/s (R_h = 16.7 nm). The difference may be due to assumption of a perfectly rigid rod in HYDRO++ or the small amount of polydispersity in laboratory measurements.

A bead model for calculation of hydrodynamic properties was developed by Broersma and later modified by Tirado and Garcia de la Torre. The equations derived from these models are discussed further in Chapter 5. Using Broersma's equations, translational diffusion is calculated to be 1.446×10^{-7} cm^2/s (R_h = 16.9 nm). The high axial ratio of the polymer chain is well within the range over which these equations are valid.

97

Table 4.2 Summary of data and results for PBLG (MW 232k, L = 160 nm); parameters selected for solvent pyridine.

This file:	12-PBLGchain-res.txt
Case:	PBLG chain
Structural file:	PBLGchaincoo.txt
Temperature:	20.0 centigrade
Solvent viscosity:	0.00879 poise
Molecular weight:	232000. Da
Solute partial specific volume:	0.79 cm^3/g
Solution density:	0.980 g/cm^3
Translational diffusion coefficient:	1.562 x 10^{-7} cm^2/s
Radius of gyration:	4.619 x 10^{-6} cm
Volume:	2.145 x 10^{-19} cm^3
Rotational diffusion coefficient:	1.196 x 10^6 s^{-1}
Relaxation time (1):	3.630 x 10^{-5} s
Relaxation time (2):	2.777 x 10^{-7} s
Relaxation time (3):	2.777 x 10^{-7} s
Relaxation time (4):	6.983 x 10^{-8} s
Relaxation time (5):	6.983 x 10^{-8} s
Harmonic mean (correlation) time:	1.394 x 10^{-7} s
Intrinsic viscosity:	377.5 cm^3/g
Sedimentation coefficient:	3.342 Svedberg
Longest distance:	1.600 x 10^{-5} cm

4.2.2 Core-Shell Particles

Input of the x, y, z coordinates is a simple task for the linear model, but becomes much more complex when trying to place several polypeptide chains on a spherical core. To generate these coordinates a simple MATLAB program was written with the capability of adjusting the length of the chain and the number of chains that are placed around the core bead. The advantage of this program is obvious in that it becomes simple to mimic changes to real hybrid particles in terms of chain length of the polypeptide on the surface and the grafting density.

To evenly distribute the beads over the surface of the core sphere, a code that creates a spiral pattern around a sphere was used.[11] Initially, the idea to use uniform longitudinal and latitudinal lines as a guideline was considered, but as the surface density is increased crowding would occur at the "poles," which is not an accurate representation of the distribution of polypeptides on the surface. Spiral coordinates provided the simplest route toward evenly spacing points on the surface of the spherical core. From the initial spiral coordinates, more beads were added to create linear chains extending from the surface. The code used to generate the coordinates of the bead model is given in Appendix B.

The limitations of this approach are apparent when trying to model the core-shell particles to scale. The small radius of the beads representing the monomers of the polypeptide chain requires that hundreds are used to create a single chain. An accurate surface density for a sphere with a 100-nm radius would include upwards of 50,000 chains. This exceeds either the program capabilities or that of the computer used. The designers of the HYDRO++ program are aware of its computational demand and suggest that for 4GB of RAM a maximum of 7,000 beads can be used in the model. Adjustments to the computer can be made to accommodate 7,500 beads, but error messages resulted when the number was increased to 8,000.

Listed in Table 4.3 are the shell thickness t_{shell} (length of the PBLG chain), the number of chains on the surface σ and the total number of beads N_{beads} input into the program for each calculation. The translational and rotational diffusion coefficients were computed by HYDRO++ and the hydrodynamic radius was determined using the Stokes-Einstein equation. Above each set of numbers is the corresponding bead model as imaged using the Cortona3D software. All of the bead models were constructed using a core radius of 100 nm to compare the effect changes in the

size of the shell have on the overall size of the particle. The results obtained from the program are consistent over multiple runs for each model.
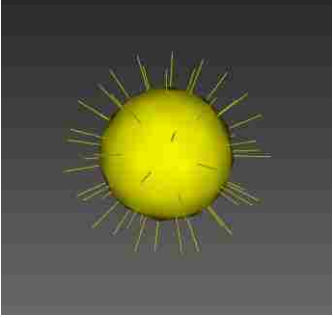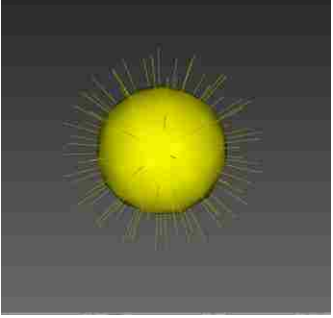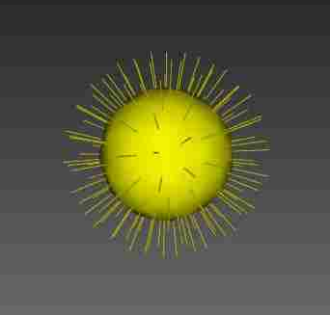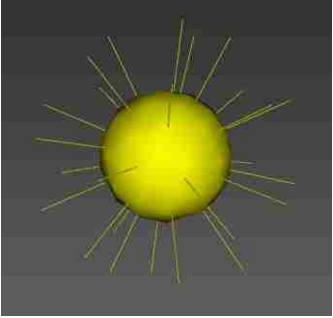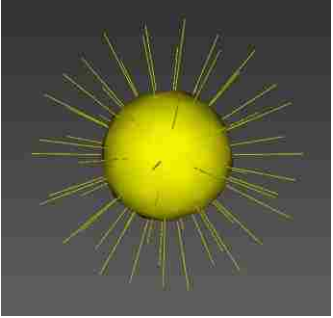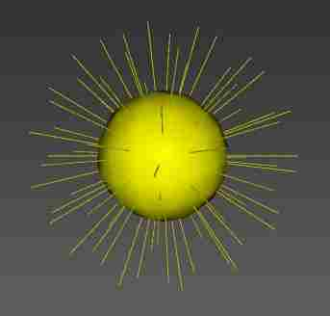
Analysis of a core bead with no shell provides a starting point for analysis. A small obstacle in the modeling of the core particle is that HYDRO++ requires at least two beads are input into the system. To circumvent this, the core bead information was input and the second bead was given a location on the surface of the core bead with an insignificant radius of 0.01 nm. Below a radius of 0.05 nm values given in the output file did not change.

The bare core has a translational diffusion coefficient of 2.44×10^{-8} giving an R_h of 100 nm, equivalent to the radius input into the program. The rotational diffusion coefficient was 183 s^{-1}, which is 2-5 times faster than the core-shell particles. Radius of gyration was 77.5 nm for the core, but the maximum R_g obtained for any core-shell particle is 78 nm. This small variation in R_g most likely results from the low surface density of the chains.

In Table 4.3 changes in the surface density, increasing from left to right, at two different shell lengths are shown. On the first row, the shell thickness is less than the radius of the core and on the second row it is longer. In both cases as surface density increases $R_{h,t}$ increases even though the shell thickness does not change. At the lowest surface density and t_{shell} of 80 nm, determination of the shell thickness from $R_{h,t}$ would measure it as only 19 nm. Experimentally, this effect is seen in a well-solvated shell with a low surface density where correlations between shell thickness from hydrodynamic measurements and length of the polypeptide chain on the surface are not easily correlated.

A series of core-shell particles having the same surface density, but differing in shell thickness, are displayed in Table 4.4. Again, low surface densities are simulated and shell thickness cannot be determined by subtracting the core radius from the particle radius. Based
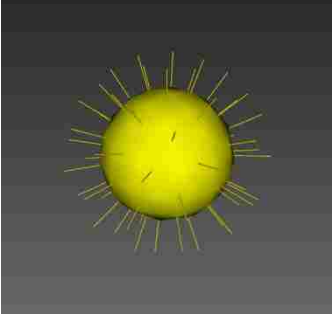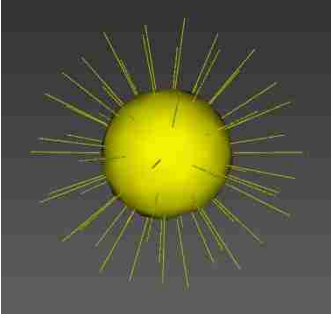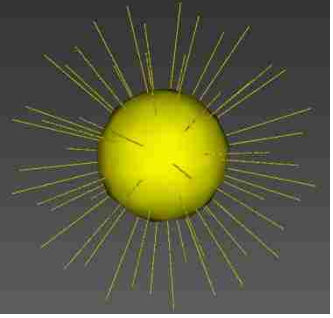
Table 4.3 Simulation results for various shell sizes and surface densities. All cores have a radius of 100 nm.

t_{shell} (nm)	80	80	80
R_{total}	180	180	180
σ	60	100	140
N_{beads}	3000	5000	7000
D_t (cm^2/s)	2.05×10^{-8}	2.00×10^{-8}	1.93×10^{-8}
D_r (1/s)	67.0	60.5	55.7
$R_{h,t}$ (nm)	119	122	127
$R_{h,r}$ (nm)	140	145	149
t_{shell} (nm)	160	160	160
R_{total}	260	260	260
σ	30	60	70
N_{beads}	3000	6000	7000
D_t (cm^2/s)	1.77×10^{-8}	1.56×10^{-8}	1.51×10^{-8}
D_r (1/s)	46.0	36.6	34.9
$R_{h,t}$ (nm)	138	157	162
$R_{h,r}$ (nm)	159	171	174

on the core-shell $R_{h,t}$, the smallest shell is only 23% of its actual thickness and for the largest it is 42%. Figure 4.3 shows the change in $R_{h,t}$ as shell thickness is increased. The increase is not linear and begins to turn upward at a thickness of approximately 75 nm. The two surface

101

densities included in the graph do not differ by much, but it is discernible that the denser shell has a faster growth rate.

Table 4.4 Simulation results for shell thickness of 80, 160 and 200 nm at a constant surface density, σ = 60. All cores have a radius of 100 nm.

t_{shell} (nm)	80	160	200
R_{total}	180	260	300
σ	60	60	60
N_{beads}	3000	6000	7500
D_t (cm^2/s)	2.05×10^{-8}	1.56×10^{-8}	1.33×10^{-8}
D_r (1/s)	67.0	36.6	27.6
$R_{h,t}$ (nm)	119	157	183
$R_{h,r}$ (nm)	140	171	188

Results from both tables show that increasing both the surface density and the shell thickness increases the hydrodynamic radii of the particles, but there is a bigger increase in $R_{h,t}$ for the thicker shell. In Table 4.3 the surface density is increased by a factor of 2.33 for both shell lengths, but for the larger shell this results in a 15% increase in thickness, whereas for the shorter chains the increase in t_{shell} is only 10%. Changes in radius are not an artifact of the quantity of beads in the model. When comparing core-shell particles containing 7000 beads (Table 4.3, column three), the resulting diffusion coefficients are not similar indicating that results are truly based on the bead positions.

Two radii are considered for core-shell particles, the core radius and the outer radius (core + shell). The larger increase in $R_{h,t}$ for the thicker shell indicates that it will approach a

value equivalent to the outer radius at a lower surface density. Figure 4.4 compares $R_{h,t}$ to surface density at two different shell thicknesses. The core is known to have an $R_{h,t}$ of 100 nm and that
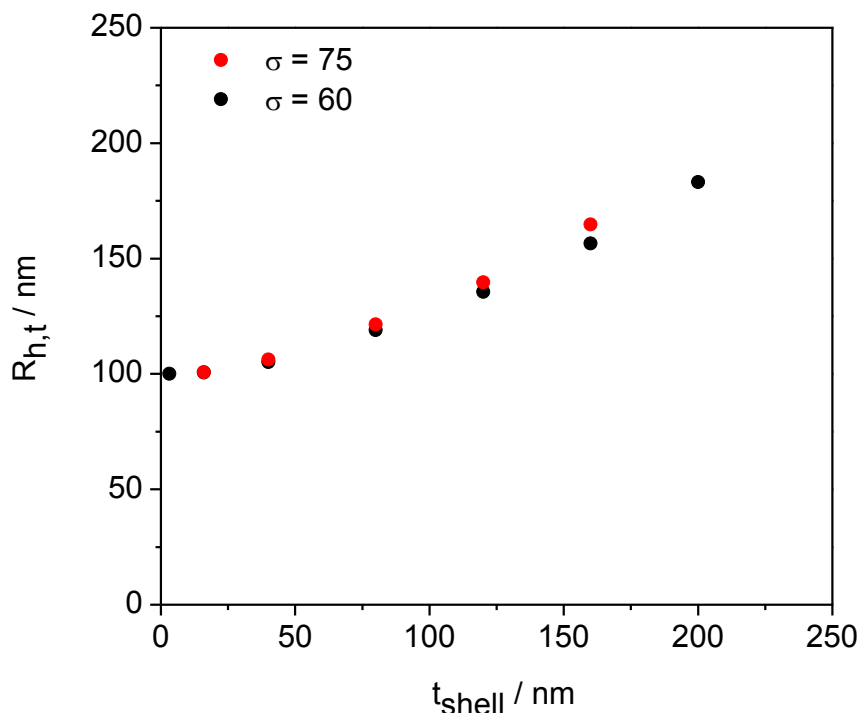

Figure 4.3 $R_{h,t}$ vs. surface density for a shell thickness of 75 nm and 60 nm. Core radius is 100 nm. As shell thickness increases the hydrodynamic radius increases more quickly for higher surface density of rodlike chains.

number becomes an asymptote for the calculated radii, but as the surface density is increased the rate becomes more linear. The points shown in the figure are at the computational limit of the current system, but future work would include extending these plots until $R_{h,t}$ coincides with the length of the chain where the numbers are expected to plateau. This would indicate a minimum surface density for the ability to consider the core-shell particles as non-draining spheres.

Several spherical core-shell particles can be cataloged in terms of shell thickness and surface density, but potentially more interesting are the comparisons that can be made between the spherical and more exotically structured particles. Table 4.5 shows two types of core-shell particles where the shell arises from polypeptide chains placed around the equatorial position on

the sphere (top row) and at the poles (bottom row). The bead model was constructed using the same spiral coordinate program at a fixed surface density. For equatorial core-shell (ECS)
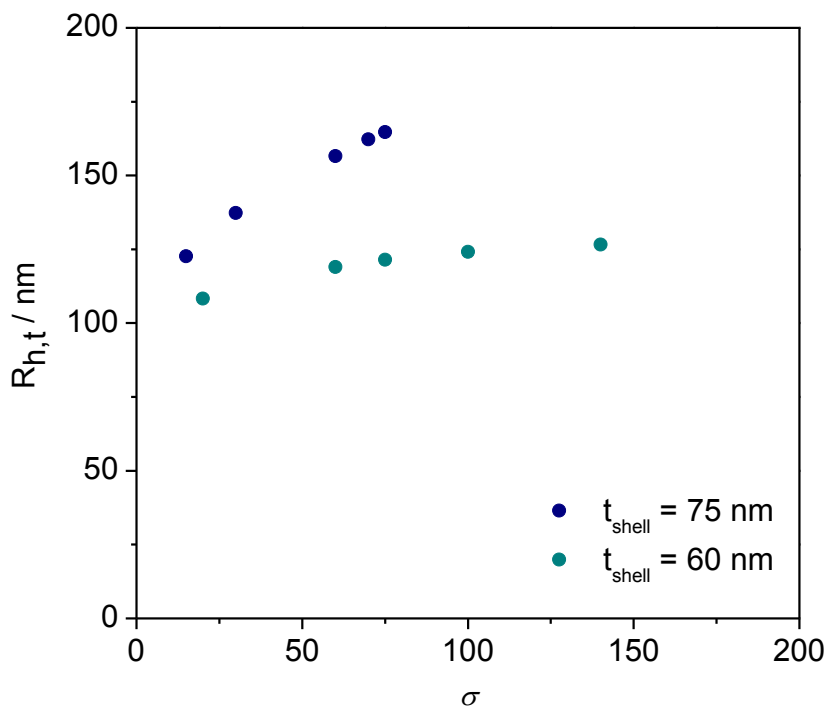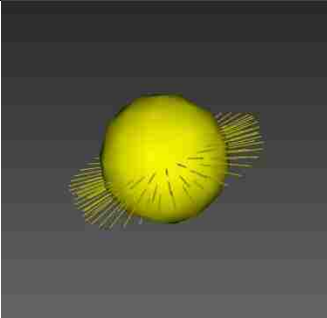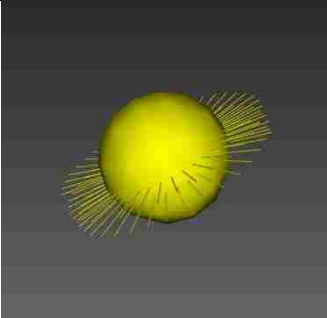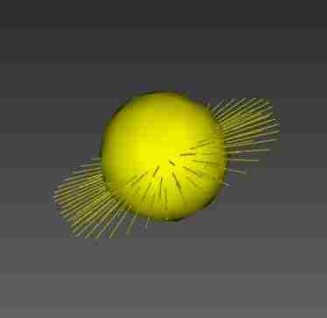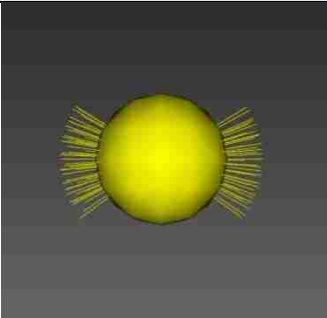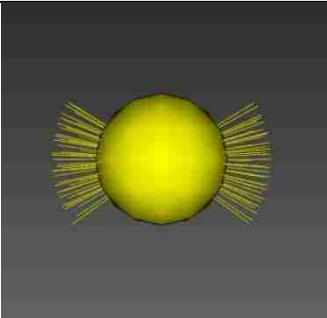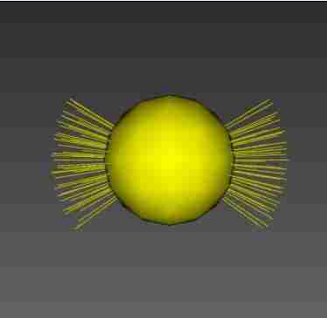

Figure 4.4 $R_{h,t}$ vs. surface density for a shell thickness of 75 nm and 60 nm. As surface density increases the hydrodynamic radius increases more quickly for the greater shell thickness.

particles equal amounts of coordinates were removed from the polar regions of the sphere until only coordinates around the greatest circumference remained. The opposite is the case for polar core-shell (PCS) particles in that the first and last 50 coordinates were used to generate the shell. Ideally, these models would mimic synthesized particles and changes to the surface density in these isolated regions are potentially variable as well.

For all particles in Table 4.5 the core bead has a radius of 100 nm and three different shell thicknesses are given and were chosen specifically to coincide with the shell thickness and surface density of the spherical particles. Increasing the shell thickness, which was expected have the greatest effect, based on results from spherical particles, had very little effect on the hydrodynamic radius. In general, polar core-shell particles are seen as smaller than the equatorial

ones even though t_{shell} and σ are equal. A spherical particle with the same surface density ($\sigma = 100$) and shell thickness ($t_{shell} = 80$ nm) has a slightly larger $R_{h,t}$. This presents surface density location as a new variable to consider.

Table 4.5 ECS and PCS models with a core radius of 100 nm. The shell thickness is varied equally for both particles.

t_{shell} (nm)	80	99.2	120
σ	100	100	100
N_{beads}	5000	6200	7500
D_t (cm^2/s)	2.24×10^{-8}	2.19×10^{-8}	2.01×10^{-8}
D_r (1/s)	74.7	64.6	55.3
$R_{h,t}$ (nm)	109	111	122
$R_{h,r}$ (nm)	135	142	149

t_{shell} (nm)	80	99.2	120
σ	100	100	100
N_{beads}	5000	6200	7500
D_t (cm^2/s)	2.30×10^{-8}	2.27×10^{-8}	2.20×10^{-8}
D_r (1/s)	87	76.9	67.1
$R_{h,t}$ (nm)	106	107	111
$R_{h,r}$ (nm)	128	134	140

The results also call into question the direction of rotation considered for the particles as two planes of symmetry exist for each. Polar core-shell particles, for instance, may have two

different rotational diffusion coefficients depending on whether spinning is about the shortest axis or the longest. The largest PCS particle simulated so far has an axial ratio of 2.2. Although technically anisotropic, it may still be low enough for the particle to be accommodated by spherical modeling. This is corroborated by the ratio of translational to rotational hydrodynamic radius being approximately 0.8 for all particles with a shell thickness of 80 nm. The caveat, however, is that at low surface densities the shell is barely "seen." Higher surface densities may result in rotational diffusion coefficients that reflect the elongation of the particle.
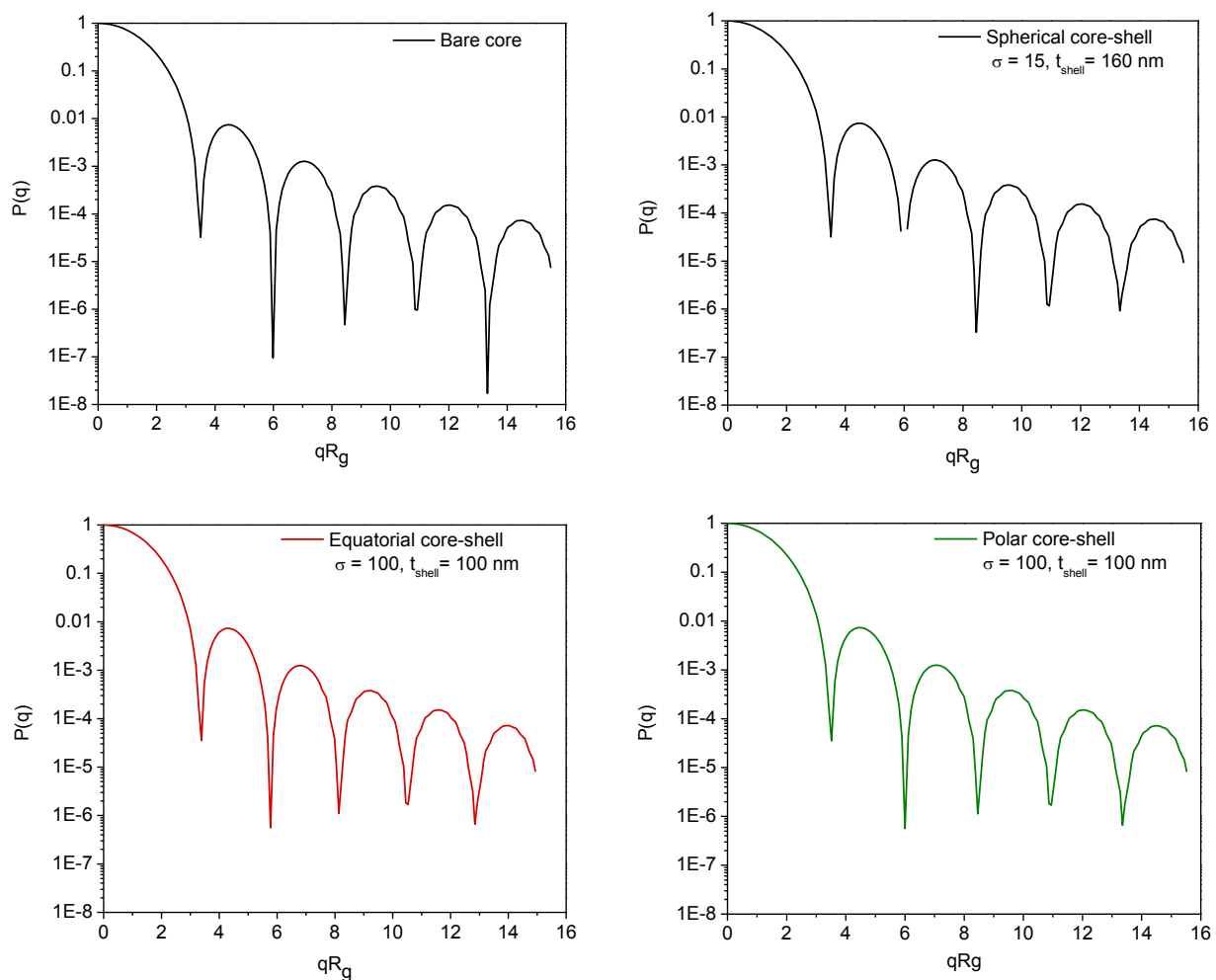

Figure 4.5 Form factors of the bare core particle along with the three types of core-shell particles: spherical, equatorial, and polar. The core radius is 100 nm for all particles; t_{shell} and σ are displayed on the graph.

Form factors and pair distribution functions are optional output from the program. Figures 4.5 and 4.6 contain these plots for the bare sphere and each type of core-shell particle. The differences are small and may not be easily noticeable from the plot, but there are slight differences in the depth of the "bounce." The form factor for the bare core reaches depths an order of magnitude lower than the core-shell particles, which is expected for a smooth surface. The polar and equatorial particles have similar form factor plots that are also similar to the spherical particle, which is not shown in this figure. Similarities are most likely due to their having the same shell thickness and surface density. Also shown in Figure 4.5 (top, right) is the result from a spherical particle with a t_{shell} of 160 nm and $\sigma = 15$. Immediately noticeable are the differences where qR_g is equal to approximately 6 and 8 indicating that even at very low surface densities overall the calculation of form factor is sensitive to these changes. The pair distribution functions for all three cases are practically identical as the sizes of the particles do not vary by much (Figure 4.6).
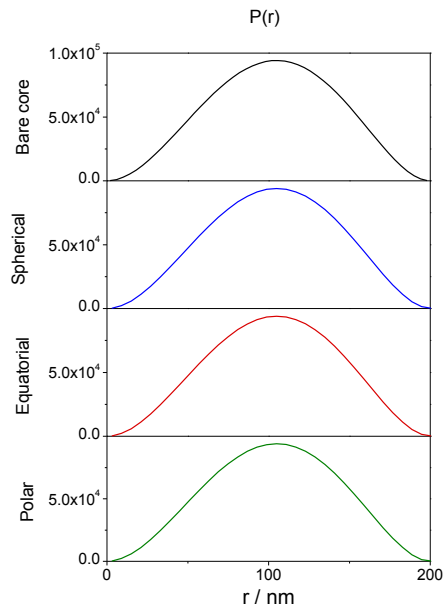

Figure 4.6 Pair distribution functions of the bare core particle along with the three types of core-shell particles: spherical, equatorial, and polar. The core radius is 100 nm, t_{shell} is 80 nm, and $\sigma = 100$.

4.3 Conclusions and Future Work

The HYDRO++ program is a quick and easy tool for determining the hydrodynamic properties of a particle or rigid polymer. The results may be compared to experimental DLS measurements, but more particle sizes and polypeptide grafting densities to get a true sense of how well the programs compares to experimental results. New structures can also be input into the system to get an estimate of the properties expected from lab analysis.

4.4 References

1.   Cerda, J. J.; Sintes, T.; Toral, R. Spherical brushes within spherical cavities: A self-consistent field and Monte Carlo study. *The Journal of Chemical Physics* 2009, 131, (13), 134901-8.

2.   Balamurugan, S. S.; Soto-Cantu, E.; Cueto, R.; Russo, P. S. Preparation of Organosoluble Silica-Polypeptide Particles by "Click" Chemistry. *Macromolecules* 2010, 43, (1), 62-70.

3.   Garcia de la Torre, J.; del Rio Echenique, G.; Ortega, A. Improved Calculation of Rotational Diffusion and Intrinsic Viscosity of Bead Models for Macromolecules and Nanoparticles. *The Journal of Physical Chemistry B* 2007, 111, (5), 955-961.

4.   García de la Torre, J.; Amorós, D.; Ortega, A. Intrinsic viscosity of bead models for macromolecules and nanoparticles. *European Biophysics Journal*, 2010, 39, (3), 381-388.

5.   Garcia de la Torre, J. Computer Programs.
        http://leonardo.inf.um.es/macromol/programs/programs.htm

6.   Garcia de la Torre, J.; Bloomfield, V. A. Hydrodynamics of macromolecular complexes. III. Bacterial viruses. *Biopolymers* 1977, 16, (8), 1779-1793.

7.   De La Torre, J. G.; Bloomfield, V. A. Hydrodynamics of macromolecular complexes. II. Rotation. *Biopolymers* 1977, 16, (8), 1765-1778.

8.   De La Torre, J. G.; Bloomfield, V. A. Hydrodynamic properties of macromolecular complexes. I. Translation. *Biopolymers* 1977, 16, (8), 1747-1763.

9.   Bu, Z.; Russo, P. S.; Tipton, D. L.; Negulescu, I. I. Self-Diffusion of Rodlike Polymers in Isotropic Solutions. *Macromolecules* 1994, 27, (23), 6871-6882.

10.   Russo, P. S.; Baylis, M.; Bu, Z.; Stryjewski, W.; Doucet, G.; Temyanko, E.; Tipton, D. Self-diffusion of a semiflexible polymer measured across the lyotropic liquid-crystalline-phase. *Journal of Chemical Physics* 1999, 111, (4), 1746.

11. Burkardt, J. Spiral points on an implicit sphere in 3D. http://www.oifii.org/ns-org/nsd/ar/me/geometry-m/html/sphere_imp_spiralpoints_3d.html#_subfunctions

CHAPTER 5. DEPOLARIZED DYNAMIC LIGHT SCATTERING OF PARTICLES

5.1 Introduction

Polytetrafluoroethylene (PTFE) is a fluorinated polymer mostly noted for its "nonstick" properties. Developed and trademarked as Teflon in the 1960's by DuPont it remains one of the most commonly used polymers in production. PTFE is not easily processed in the melt, instead techniques to manipulate PTFE are often based on its powdered form to create molded objects,[1] but it is not limited to use in this state. Currently, DuPont uses aqueous dispersions in a dip-coating method where several coatings are applied for the desired thickness.[2] Beyond molded objects, hydrophobic properties[3] have increased its popularity as a coating material with applications in biomedical materials and engineering.[4, 5] Also useful as a substrate, Cui synthesized PTFE-acrylate core-shell nanoparticles by emulsion polymerization for the purpose of improving PTFE's adhesive capabilities.[6] Research laboratories all over the world have PTFE membrane filters in common as they fulfill the requirements necessary for a successful filter material being chemically resistant, allowing pore size control and low friction coefficient at the surface of the polymer.[7] The commercial applications of the specific version of latex used in these studies are fabric impregnation, coatings, film casting, cookware and industrial.[8]

Preparation of PTFE latex is accomplished by suspension polymerization of tetrafluoroethylene where nonpolar monomers react within droplets suspended in an aqueous media. As an optional component surfactant, having a polar head and nonpolar tail, surround the droplets and aid in the maintenance of the dispersion. Additives may be included in the polymerization process to generate the desired characteristics of the polymer. PTFE is available for purchase usually in the form of a small particle or as a fine powder with the particle sizes available in the range of 5 nm to 1 micron.[9]

The structure of PTFE is a linear polymer chain made of simply carbon and fluorine (Figure 5.1). The long chains are capable of packing closely enough to create crystalline domains. The content of crystallinity for PTFE is very high at approximately 95%, if it has not been previously exposed to extreme heat.
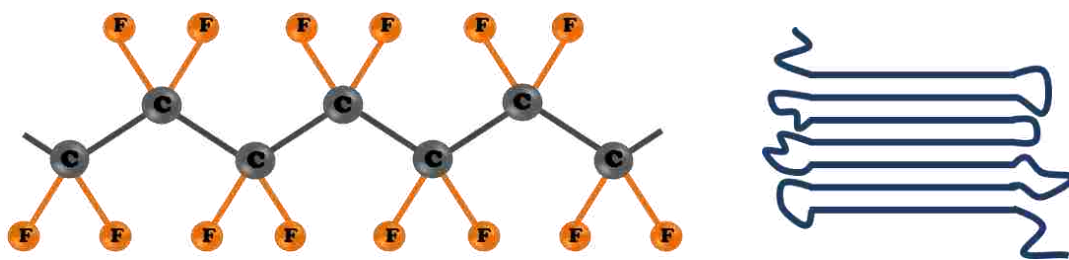

Figure 5.1 PTFE linear polymer chain and crystalline domain.

Rod-shaped PTFE latex particles prepared by emulsion polymerization often possess crystalline properties and are usually polydisperse. Emulsion polymerization requires a surfactant to stabilize the latex particles as they form, but once the emulsifier is removed by dialysis they are prone to coagulation. Charges on the surface of PTFE particles may be the cause of this effect and studies have been conducted that relate surface charge to pH.[10]

Depolarized dynamic light scattering (DDLS) has a wide range of applications.[11-16] Particularly in probe diffusion experiments where changes in the rotational diffusion calculated for the probe particle depend on changes in the surrounding media.[13] Koenderink studied latex probes immersed in a xanthan polymer solution where particle diffusion deviated from Stokes-Einstein behavior indicating the solution could not be viewed as a continuous fluid.[17, 18] Changes in phase behavior are also monitored this way as the particle diffuses differently when the polymer concentration in solution was increased.[19, 20] Besides concentration changes, other variables are explored as well. Changes in molecular weight, which can have an effect on viscosity, may also alter the diffusion coefficient. Information about more complex interactions may be sought by studying the ionic interactions of polyelectrolytes with the addition of salt.[21-23]

Still another option for probe diffusion studies is to modify the probe itself, by using a colloidal particle with metallic inclusions that provide a depolarized signal.[24]

With knowledge that latex particles having a crystalline nature are prime candidates for use as probe particles in a DDLS experiment, this chapter focuses on the separation PTFE latex particles according to size for potential use as monodisperse probes eliminating the variables associated with polydisperse samples. It further evaluates the separation ability of asymmetric flow field flow fractionation by comparison with results from polarized and depolarized dynamic light scattering.

PTFE latex particles have been fractionated by size using asymmetric flow field flow fractionation (AF4) coupled to multiple-angle light scattering (MALS). The particles are characterized by traditional and depolarized dynamic light scattering to confirm that smaller particles elute first. Elution order is opposite that of size exclusion chromatography, where large polymers elute first, due to the unique flow profile that retards the flow of large particles as they travel down the channel. While the fractions collected from the AF4 are not monodisperse, the uniformity is slightly increased improving their quality for use as diffusion probes. Interest in accurate particle sizing is also useful for applications in nanomaterials. Recently, Kato studied the accuracy of size determination of AF4 and DLS for spherical polystyrene latex particles.[25]

PTFE latex particles are well suited for DLS analysis even though its refractive index (RI=1.37) does not vary greatly from that of water (RI=1.33). AF4 instrumentation used is not designed for high throughput, so reasonable concentrations must be injected for analysis. One of the most challenging aspects of this analysis was obtaining a concentration sufficiently high enough for particle scattering in the polarized and depolarized modes. This is particularly

important for depolarized scattering as the horizontal filter significantly reduces the amount of signal.

5.2 Experimemtal

5.2.1 Materials

Polytetrafluoroethylene (PTFE) latex particles suspended in water were supplied by Ausimont (Algoflon #D60 V). Few details were provided about the dispersion, but information about similar latex particles in Ausimont's D60 series may provide some insight into the composition of this sample. It might be inferred that the dispersion is 60% solids by weight with the addition of 3-4 wt% nonionic surfactant. Also based on patent information from inventions using similar particles[26, 27] the nonionic surfactant used in the storage of the particles may be Triton X-100 (Figure 5.2), a non-ionic surfactant with the polyethylene glycol component having a degree of polymerization of approximately ten units. Typical particle size was recorded to be 240 nm with a density of 1.5 g/mL.[8, 28]
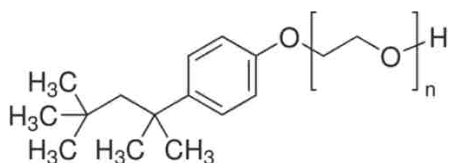
Figure 5.2 Structure of Triton X-100 surfactant used in the storage of PTFE latex.

For analysis by AF4 further dilutions were made with purified water from a Barnstead Nanopure system. The stock solution was a 100 μL in 10 mL dilution of latex particles with 0.1% v/v FL-70 surfactant and 200 ppm sodium azide. FL-70 detergent added to the stock solution served to prevent particles from aggregating during separation in the AF4 channel, but the percentage is insufficient for micelle formation.[29] The detergent mixture is nearly 90% water, but the surfactant properties arise from small amounts of ionic compounds and long side chain

complexes: triethanoleamine oleate (4%), sodium carbonate (3%), alcohols (2%), tetrasodium ethylenediaminetetraacetate (1%), sodium oleate (<1%) and polyethylene glycol (<1%).

Fractions from four injections were collected at one minute intervals. Prior to injection the sample was agitated to resuspend the particles that would often settle over time due to the density of PTFE being heavier than water. Collecting a single set of fractions per injection was not sufficient to accurately measure scattering by DLS. To solve this problem multiple fractions were collected, in their respective vials, taking care not to "cross-contaminate" them. For example, the fraction occurring at 39 minutes into the separation was collected in the same vial four times.

Once multiple fractions were collected in one vial, the sample was concentrated by rotary evaporation, an instrument that centrifuges the sample to keep particles near the bottom of the vial while the solvent is evaporated. The evaporation time required 2 hours at peak instrument performance. The samples were then sonicated to break up any aggregates formed in the concentration step. Finally, the samples were filtered for dust and possible aggregates in preparation for analysis.

5.2.2 Asymmetric Flow Field Flow Fractionation (AF4)

Separation of the colloidal particles was achieved using an Eclipse 2 AF4 by Wyatt Technology Corp. (Santa Barbara, CA) equipped with a Dawn Heleos 18-angle light scattering detector, dynamic light scattering detector and a 658-nm GaAs (50 mW) laser. The samples were injected using an Agilent 1100 HPLC system (model 1100 isocratic pump, 1100 degasser and 1100 autosampler, Agilent Technologies, Palo Alto, CA). The same method of delivery was also used to transport the mobile phase to the AF4 system. The AF4 channel fitted with a 490-micron thick Mylar spacer and the membrane, made of regenerated cellulose, had a 10 kDa molecular

weight limit (Wyatt). The channel dimensions were: length, 24 cm; inlet channel width, 2.15 cm; outlet channel width, 0.6 cm; flow rate through channel, 1 mL/min; cross flow through channel, 0.3 mL/min; ramp 40 minutes to 0 mL/min; focus flow, 3 mL/min, 5 minutes. Concentration detection was achieved using a Wyatt Optilab rEX Differential Refractive Index detector at 658 nm. Wyatt Astra software (version 5.3) was used to acquire and analyze data. For fraction collection, 100 μL of the diluted Algoflon suspension was injected; fractions were collected at one-minute intervals.

5.2.3 Dynamic Light Scattering (DLS)

The DLS instrument used in this experiment was designed and constructed at Louisiana State University and has been described previously in detail.[30] The light source is a JDS Uniphase air-cooled Argon ion laser with a wavelength of 488 nm (blue light). The scattered light is detected with an ALV/SO-SIPD Single Photon Detector (ALV, Langen, Germany). The design is referred to as pseudo cross correlation detection due to the use of an optical beam splitter, two PMTs and decoupled electronics. This detector is equipped for use with a fiber optic to receive scattered light; however, this attachment is not a necessity. Instead a light-absorbing adapter was fitted to the fiber optic port and attached to the detector support. Photon counts from the detector were monitored using a Pacific Precision Instruments photometer (Model 126) and the intensity signal is correlated by an ALV-5000 multiple τ digital correlator (ALV, Langen, Germany).

Six angles ranging from 30 to 90 degrees were used in measuring the latex particles. Multiple runs, varying between 3 and 20, were completed for each angle. The accompanying software, ALVAN, was used to inspect each correlation function and its corresponding intensity trace. Averaged results were analyzed using the ALV-5000 software to determine decay rates.

Sample cells were prepared by cleaning glass Pyrex tubes by sonication with soap and water and then repeated rinses with nanopure water. All solutions were filtered with Whatman 0.45-µm pore size PVDF filters (13mm disc, polypropylene housing). The cells were checked for dust by viewing then in the path of the laser at an angle between 20 and 30 degrees.

5.2.4 Depolarized Dynamic Light Scattering (DDLS)

DDLS was performed on the same DLS instrument as described in the previous section, but with the addition of two Glan-Thompson crystals (Karl Lambrecht) for H_V scattering. One placed in the vertical position before the sample to insure vertical polarization of laser light and the second after the sample oriented in a horizontal position, perpendicular to the first polarizer. Some samples were measured in U_V scattering mode in which only the vertical polarizer is placed before the sample and the scattered light is left unfiltered. Cross-polarization was verified by viewing an isotropic sample at 90 degrees, where horizontally polarized light should not occur.

5.2.5 Transmission Electron Microscopy (TEM)

Electron microscopy was conducted at the LSU Socolofsky Microscopy Center through the department of Biological Sciences. The TEM is a JEOL 100CX with magnification capabilities up to 250,000X. For this experiment images were taken at magnifications of 50X and 100X. TEM samples were prepared by placing a single droplet on a 400-mesh, carbon-coated, copper grid from Electron Microscopy Sciences and allowed to dry in ambient air overnight. The grids were stored in a petri dish lined with filter paper. Prior to imaging, the samples were stained with a phosphotungstic acid (PTA) solution and air dried for approximately 5 hours.

5.3 Results and Discussion

5.3.1 Analysis of PTFE Fractionation by U_V Scattering

A total of three sets of fractions were collected for this study since its inception. The first set was analyzed by Dr. Erick Soto-Cantu, a former graduate student from this research group. Subsequent collections were obtained, with the help of Dr. Rafael Cueto, to confirm initial results. The first set was separated by AF4 and captured fractions were measured by DLS. AF4 elutes smaller particles first and increasingly larger particles thereafter leading to the expected result of increasing radius as a function of elution time. Figure 5.3A shows both the intensity trace with elution volume at 90 degrees. Overlain is the radius of gyration (R_g) calculated from the light scattering data coupled to the AF4/MALS instrument and hydrodynamic radius from Malvern's ZetaPALS instrument at a single angle of 174 degrees (632.8-nm wavelength).
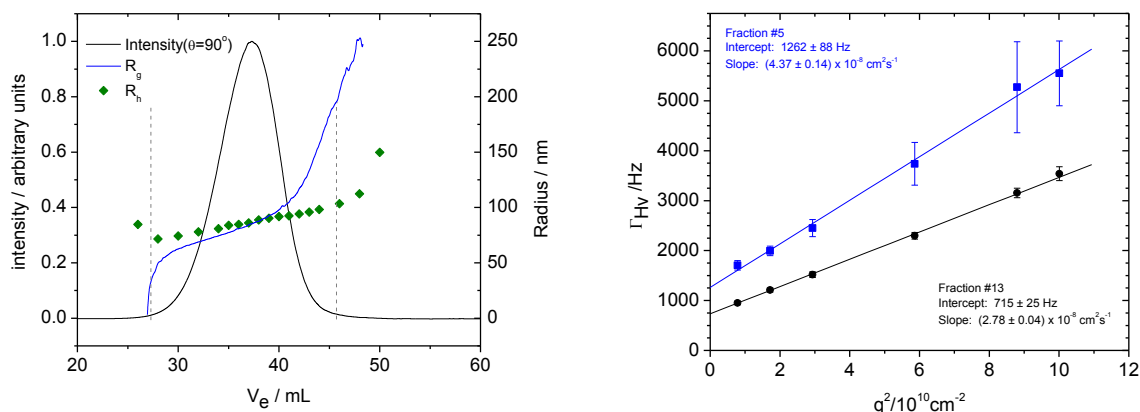
Figure 5.3 (A) Intensity trace vs. elution volume for AF4 separation of PTFE latex particles. (B) Decay rates for two fractions, one early and one late eluting in H_V scattering.

The tail ends of the peak are not easily analyzed due to the lack of signal and the values become unreliable in those regions. Figure 5.3B compares the decay rates for two fractions on opposite sides of the intensity peak. R_g surpasses R_h for later-eluting species and for fraction 5, the error increases at high angles. Combined, these observations indicate that the larger particles may be more extended or even aggregated.

117
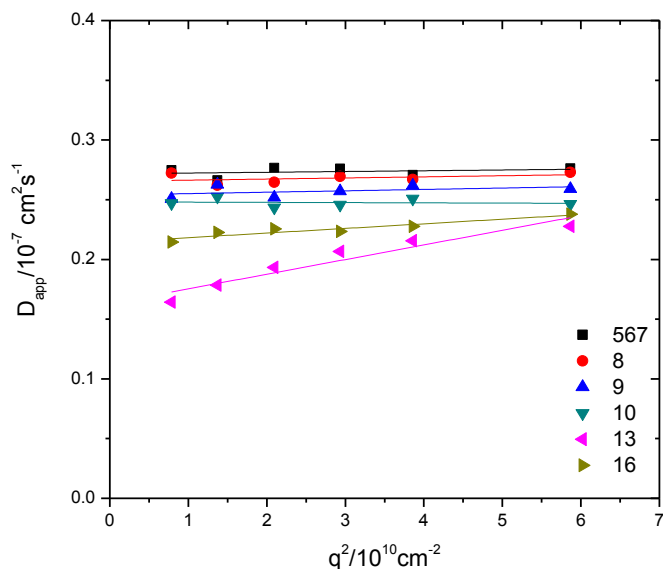
Figure 5.4 Apparent diffusion coefficient as a function of q^2 for PTFE latex particles collected at different elution times from AF4.

A repeat experiment was conducted to confirm that fractions differed on either side of the peak. A new set of fractions were collected with approximately the same AF4 conditions and were prepared for analysis by polarized and depolarized scattering. Figure 5.4 shows the apparent diffusion coefficient for selected fractions. Light scattering analysis for these samples were challenging due to what was perceived as dust, but actually may have been insufficient particle concentration. Earliest eluting fractions were not concentrated enough to scatter and they were abandoned for fractions at the top of the peak where the intensity was greatest. To include fractions at approximately half of the peak height three fractions (referred to as "567") were combined and analyzed as a single sample.

The diffusion coefficients appeared to decrease with increasing elution time for the fractions as expected, except for the transposition of fractions 13 and 16. The most noticeable observation is that the later-eluting particles produced a D_{app} vs. q^2 plot with a significant slope, while the others remained near zero. It was deemed necessary to further investigate this situation

118

for possible end over end tumbling effects, which could be a potential explanation for the rising slope in the D_{app} vs. q^2 plot.

It was hypothesized that the increase in depolarized scattering for later eluting fractions was due to an increase in the amount of crystallinity in the particles. Depolarization ratios were calculated for fractions corresponding to the peak of the intensity trace, where signal is greatest. Measurements were made in triplicate and the standard deviation is taken as the error. Figure 5.5 reveals that there is virtually no relationship between elution time and depolarization ability.
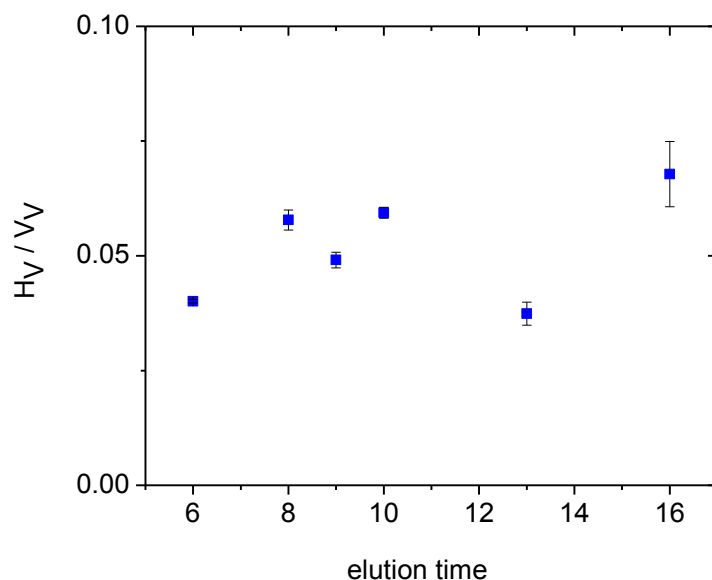
Figure 5.5 Depolarization ratios for PTFE fractions 5-10, 13, and 16. Fractions 5, 6, and 7 were combined and labeled as 6 in this plot.

Based on the previous experiment where the sample concentrations were too low, requiring the elimination of certain samples, it was determined that multiple runs should be collected for each time interval. The trace of intensity vs. time (synonymous with elution volume for 1 mL/min flow rate) is shown in Figure 5.7. The size range spans approximately 20 nm ranging from about 95 to 115 nm using a spherical approximation model that calculates the geometric radius. DLS provides a slightly different size determination, the hydrodynamic radius (R_h), which is also included in the plot. Three hydrodynamic radii are presented: one based on

119

calculations from the translational diffusion coefficient, determined from DLS, and two based on the translational and rotational diffusion coefficients determined from depolarized DLS.

Static light scattering (SLS) measurements are possible based on the intensity traces obtained from software accompanying the AF4. The Guinier equation below describes the relationship of scattered intensity to R_g, where I_s is scattered intensity, I_0 is initial intensity, and q is the scattering angle. This approximation is valid only at low angles and should only represent the linear region of the curve.

$$\ln I_s(q) = \ln I_0(q) - \frac{q^2 R_g^2}{3} \tag{5.1}$$

Several points are generated by the AF4 software for the intensity trace, but nine slices were extracted to correspond with the fractions analyzed by DLS (Figure 5.6). Fifteen angles were available for use, but to achieve a linear plot only five angles were chosen ranging from 42.8 to 79.7 degrees. Excel's LINEST function, which uses least squares fitting, provided a linear slope of the curves and R_g was calculated according to Equation 5.1. The resulting values and error bars are plotted along with the other radii in Figure 5.7, although the error bars are not easily visible due to their small size.
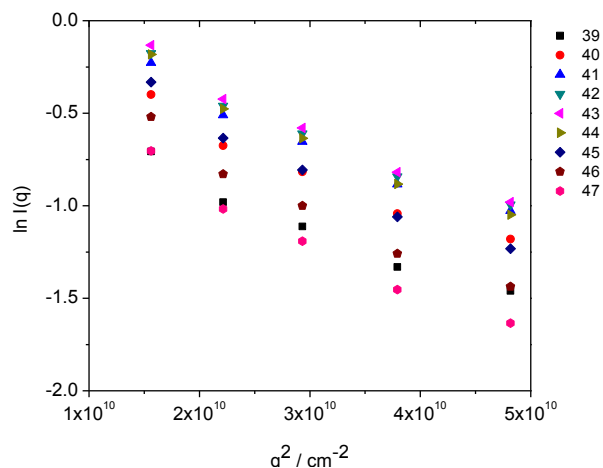
Figure 5.6 Guinier plot with intensity slices chosen for the same elution time of samples analyzed by DLS.

120
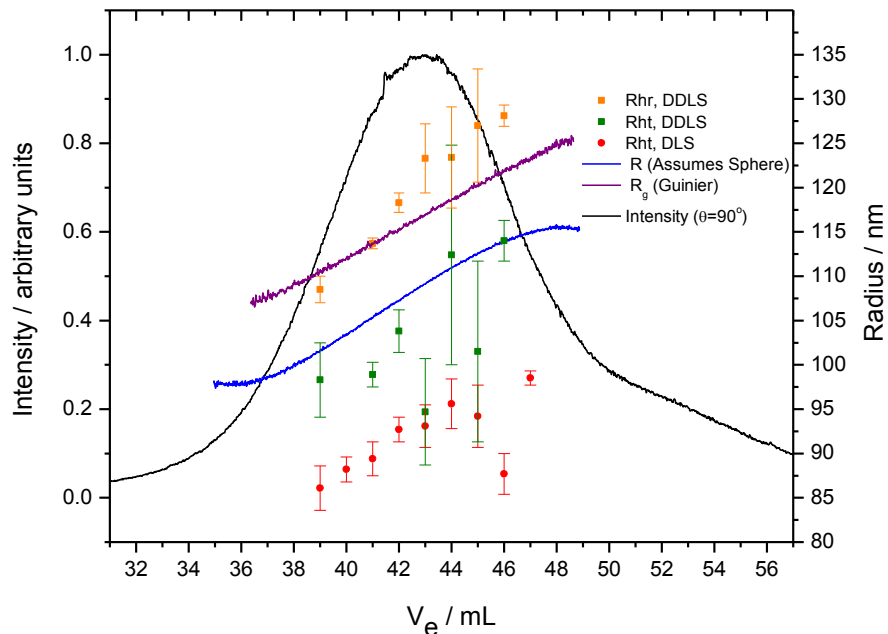
Figure 5.7 Overlay of intensity trace from AF4 (black) with various calculations of radius. R_{geom} determined by AF4 software (blue). Translational R_h calculated from both DLS (red) and DDLS (green). Rotational R_h was determined by DDLS (orange). R_g is based on Guinier approximation (purple).

A detailed description of the method used to calculate R_h is given in Chapter 2 and the results of these calculations are summarized in Table 5.1. The overall trend is an increase in particle radius from the beginning of the elution to the end. For $R_{h,t}$ (DLS), one anomalous data point exists for the fraction collected at 46 minutes. Despite analysis of multiple runs, it is not clear why this particular fraction has a smaller calculated radius than expected. Further investigation would be needed to discover what is causing the disparity, but the focus of this study is to highlight the depolarization effect.

The apparent diffusion coefficients are calculated the new set of data (Figure 5.8) and it is immediately noticeable that the diffusion coefficients do not differ by very much, which is consistent with findings from AF4 that the particle sizes only vary by about 20 nm. The slopes are somewhat linear initially and gradually increase with elution fraction. This behavior is

Table 5.1 Hydrodynamic radii based on calculations from the diffusion coefficients obtained from both translational and rotational DLS. "Un" corresponds to the measurement of an unfractionated sample from the stock solution.

Fraction	39	40	41	42	43
$R_{h,t, DLS}$/nm	86.1 ± 2.5	88.2 ± 1.4	89.4 ± 1.9	92.7 ± 1.4	93.1 ± 2.4
$R_{h,t, DDLS}$/nm	98.3 ± 4.2	n/a	98.9 ± 1.4	103.8 ± 2.4	94.7 ± 6
$R_{h,r, DDLS}$/nm	108.5 ± 1.5	n/a	113.7 ± 0.6	118.3 ± 1.1	123.3 ± 3.9
Fraction	44	45	46	47	Un
$R_{h,t, DLS}$/nm	95.6 ± 2.8	94.2 ± 3.5	87.7 ± 2.3	98.5 ± 0.8	104.0 ± 0.6
$R_{h,t, DDLS}$/nm	112.4 ± 12.4	101.5 ± 10.2	114.0 ± 2.3	n/a	n/a
$R_{h,r, DDLS}$/nm	123.4 ± 5.7	127.0 ± 6.4	128.1 ± 1.2	n/a	n/a
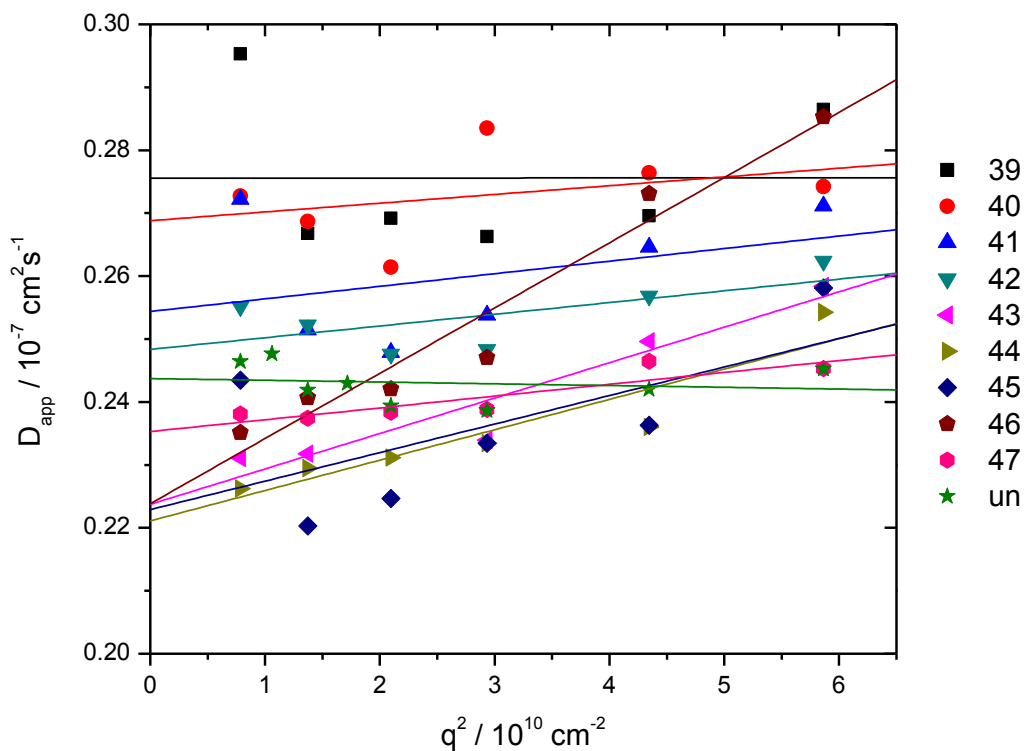
Figure 5.8 D_{app} vs. q^2 from DLS for each fraction collected from the AF4 including the unfractionated sample.
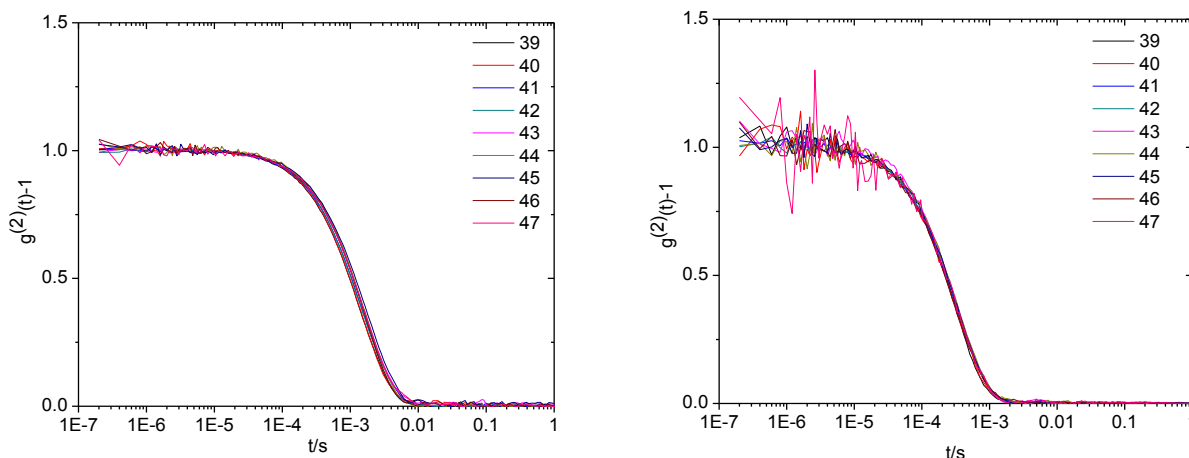
Figure 5.9 Normalized correlation function for UV scattering of each fraction at angles 40 and 90 degrees.

similar to what was observed in the previous set of data. In fraction 46 the diffusion coefficients calculated for angles 75 and 90 are considerably higher than the lower angles giving the largest slope of all of the fractions. This may account for the strong deviation from linearity this fraction presents in the plot of hydrodynamic radius vs. elution time.

Correlation functions from U_V scattering for all fractions (at angles 40 and 90 degrees) were plotted on the same graph (Figure 5.9). They were normalized by dividing the entire curve by a constant to attain an initial value of one. Differences between the curves are barely noticeable and it could be argued that particles were not adequately separated, but cumulant and single exponential analyses produced decay rates with enough contrast between fractions that resulting radii were not within error; however, this does not imply that the fractions were monodisperse.

Polydispersity, quantified by the ratio of the second cumulant to the square of the average gamma (μ_2/Γ^2), is plotted as a function of q^2 on a single graph for each fraction (Figure 5.10). Most of these decrease with angle initially, which indicates polydispersity. In some cases there is

also a gradual increase at the highest angle which may be the result of problems with noise due to low scattered signal.

There was no true correlation between the noise level of the correlation function and the fraction number, so no trend could be established in terms of increased monodispersity or polydispersity with each fraction. In terms of the quality of the correlation function with fraction number, the samples that were more concentrated (showing a higher signal in the intensity vs elution plot) scattered more light and were less noisy.
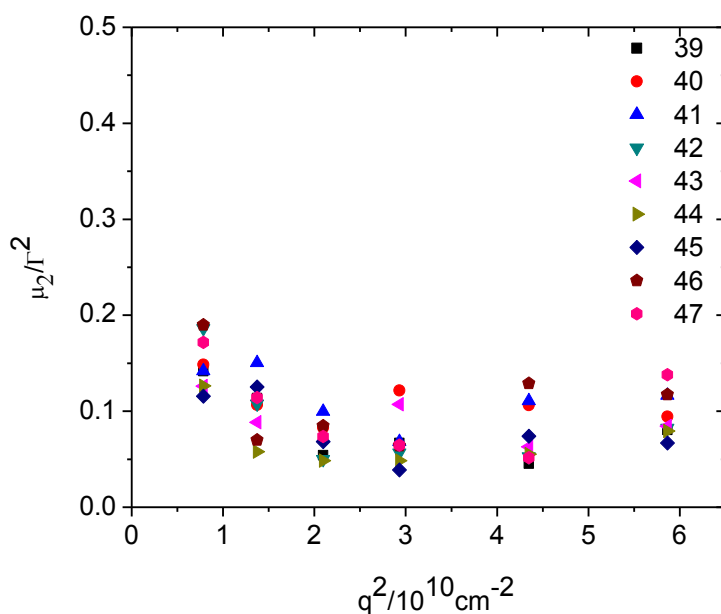
Figure 5.10 Polydispersity index for all fractions based on cumulant analysis from DLS.

Each fraction was analyzed using both single and two exponential analyses. The results are plotted in Figure 5.11 below. The green line shows the single exponential fit where the blue line shows both the slow and fast modes of the two exponential fit. In each fraction the single exponential fit is fairly linear, but the double exponential fit shows some changes with each fraction. The blue line corresponds to the slower mode and the red line to the faster mode. The slower mode in this case would correspond to the actual translational motion of the colloidal particles and is expected to follow that of the single exponential decay. The red line which

follows the faster mode may correspond to a rotation of the particle about its shortest axis resembling a tumbling motion. Spinning of the particle about the longest axis would have a decay rate that is faster than what our equipment could detect and is not visible here. No appreciable difference is visible between the modes, except for the large spikes, which are arguably due to noise.
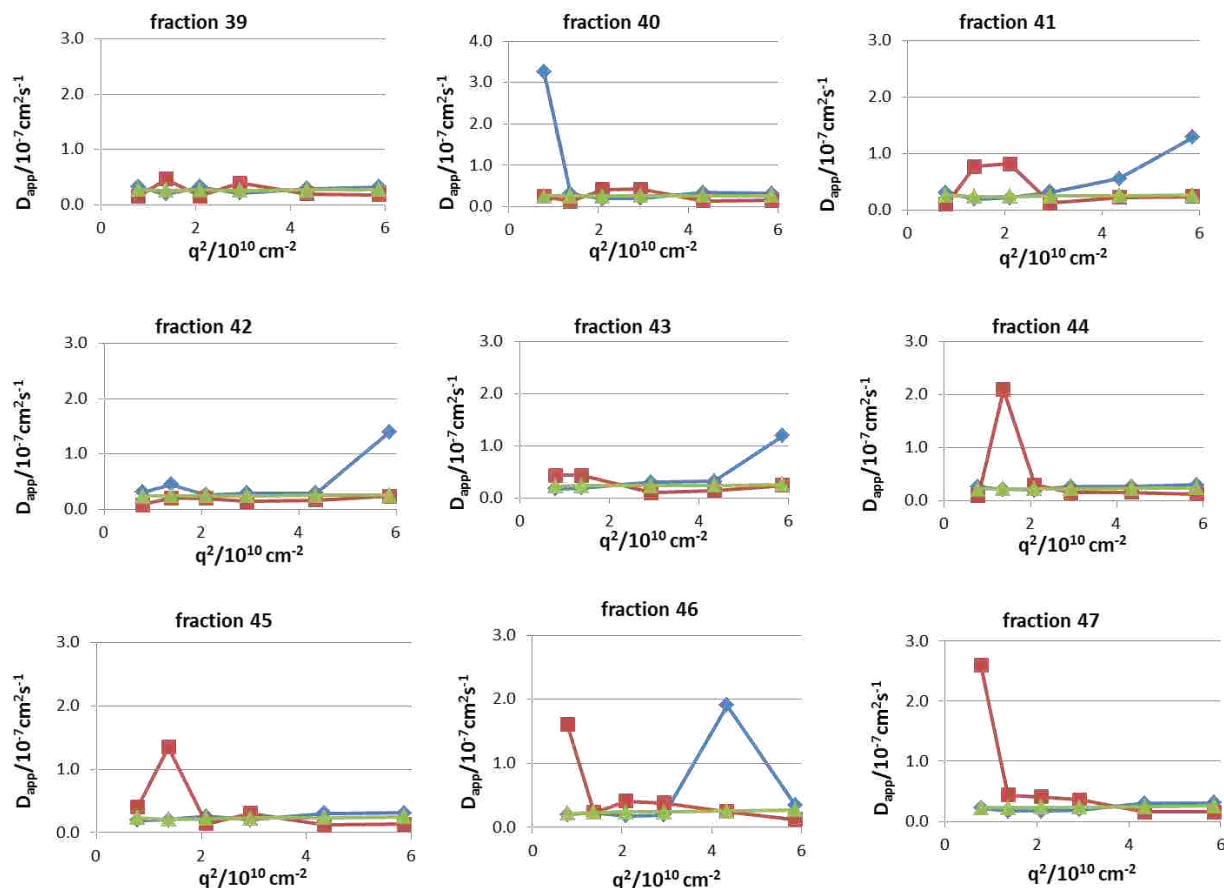
Figure 5.11 Comparison of single and double exponential fits for all fractions. Single exponential fit is in green. The blue line is the first coefficient of the 2-Exponential fit and the red line is the second.

5.3.2 Analysis of PTFE fractionation by H_V scattering

Correlation functions generated in H_V mode were analyzed by the same methods as in U_V mode and gamma vs. q^2 plots were constructed (Figure 5.12). The translational diffusion is calculated from the slope of the curve, but reliability appears to be an issue for $R_{h,t}$ as evidenced

by comparatively low values at certain elution times and large error bars. The rotational diffusion coefficient calculated from the intercept is in agreement with DLS results that display an upward trend over time. Referring back to Figure 5.7 it is obvious that the numbers from DDLS are much larger than those from DLS by an average of 15%. This additional size may be an overestimation from approximating the shape of the particle as a sphere.
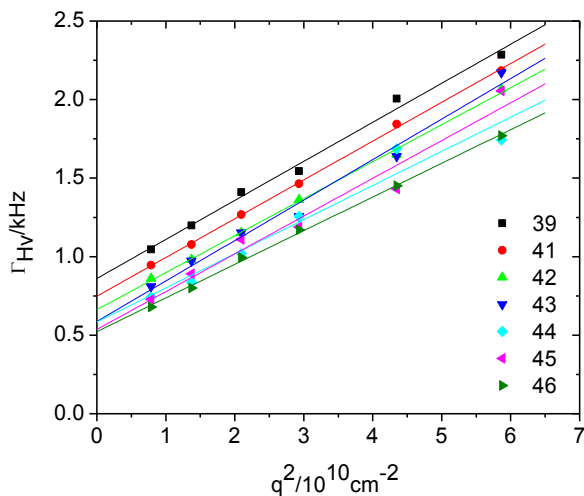
Figure 5.12 Gamma vs. q^2 plots for selected fractions in H_V scattering.

Selected fractions were viewed by TEM and their sizes were measured using ImageJ software (National Institutes of Health, USA). The shape of the particles appear to be similar to a spherocylinder due to its cylindrical body and rounded ends, a characteristic detail that may not be obvious from AF4 or DLS alone. During the process of drying particles for TEM, it is common for them to bunch together. Some of them are obviously lying flat along the longest axis, but others appear to be standing on its edge or tilted slightly upward. TEM provides a 2-D picture of the sample, and features related to depth are typically not discernible, but the shading and highlights on the particles hint that the body may not be cylindrical. It is possible that they are slightly flattened, introducing a third axis, but this has not been confirmed by other analysis methods.

126

Fractions eluting at 40 and 46 minutes were chosen because they fall on opposite ends of the intensity peak. It is not obvious by eye, but there are slight differences in the average length
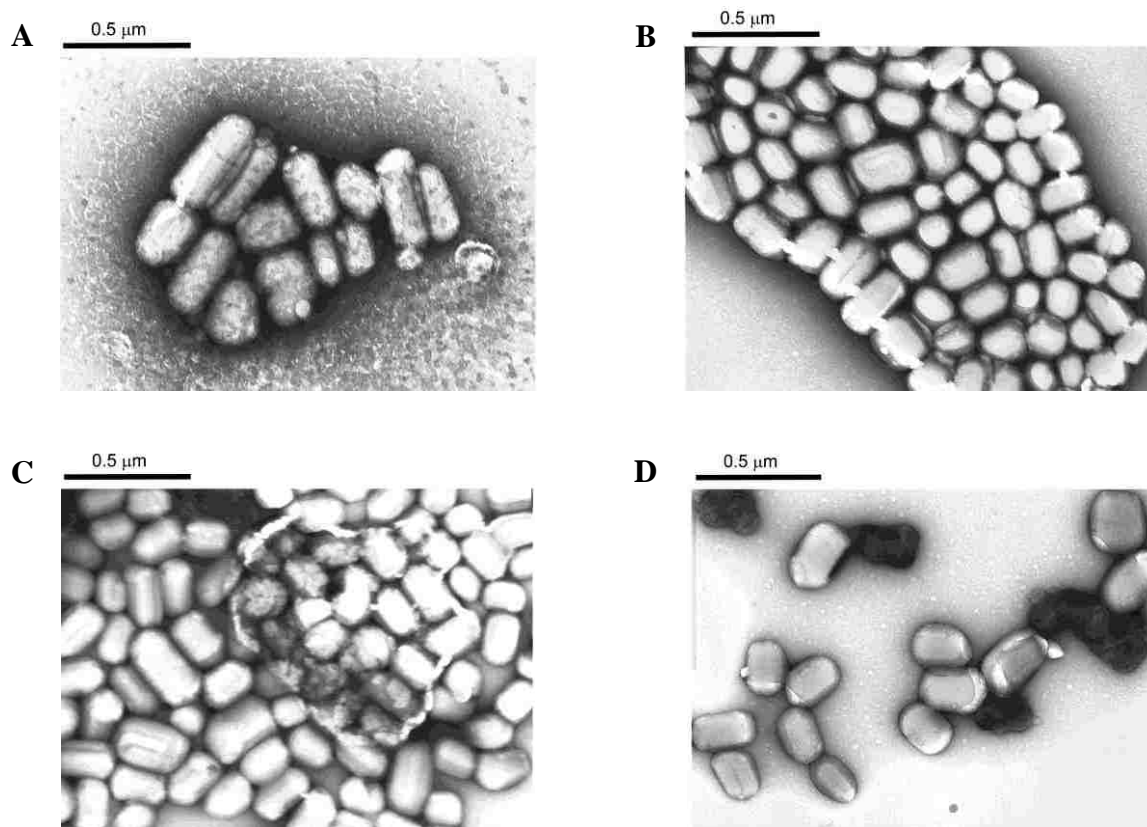
Figure 5.13 TEM pictures of PTFE latex particles (A) directly from the bottle, unaltered by sample preparation, (B) After sample preparation, but prior to separation, (C) fractions 40 and (D) 46 after separation by AF4.

and width of the particles. Fewer than twenty were sized which is certainly not enough to determine an accurate average of the entire sample, but the results were consistent with previous sizing done in the same manner for an earlier set of fractions where hundreds of particles were measured. The result for fraction 40 was an average length of 233 nm and width of 172 nm (axial ratio of 1.36). For fraction 46, the average length was 248 nm and the width 173 nm (axial ratio of 1.44). Interestingly, the median length of fraction 40 is 239 nm and width is 174 nm, while for fraction 46 the median length is 241 and the width is 164 nm. Outliers affect averages more than

medians and fraction 40's averages are lower than their respective median values, while fraction 46's average is higher. This resembles information already outlined that the particles are being separated according to size, but that each fraction possesses some degree of polydispersity.

5.3.3 Theoretical Modeling of Particle Size

Diffusion of long, thin rods was modeled several years ago by Kirkwood and Riseman using a bead model to represent a cylindrical particle.[31] Broersma sought to adjust this model to include the hydrodynamic behavior of hard cylinders. Retaining Equations (5.2) and (5.3), which are based on the Stokes-Einstein relation, adaptations derived from experimental data were made resulting in a new set of equations where L is the length, d is the diameter of the particle, and D and D_R are translational and rotational diffusion coefficients.[32, 33]

$$x = \frac{L}{d} \tag{5.2}$$

$$D' = \frac{k_B T}{3\pi\eta_0 L} \tag{5.3}$$

$$D'_R = \frac{3k_B T}{\pi\eta_0 L^3} \tag{5.4}$$

$$\delta = \ln{(2x)} \tag{5.5}$$

$$\gamma_\parallel = 1.27 - 7.4(\delta^{-1} - 0.34)^2 \tag{5.6}$$

$$\gamma_\perp = 0.19 - 4.2(\delta^{-1} - 0.39)^2 \tag{5.7}$$

$$\zeta = 1.45 - 7.5(\delta^{-1} - 0.27)^2 \tag{5.8}$$

$$D = D'[\delta - \frac{1}{2}(\gamma_\parallel + \gamma_\perp)] \tag{5.9}$$

$$D_R = D'_R(\delta - \zeta) \tag{5.10}$$

Broersma's equations lose accuracy at low axial ratios below 4.0 and are not suitable for modeling these latex particles. Tirado introduced an exception to these equations that specified a

spherocylinder shape over a simply cylindrical one. It targets axial ratios between 2 and 20. Although axial ratios for particles in this experiment were below 2, the equations are close to what is obtained experimentally.

$$v = 0.312 + \frac{0.565}{x} - \frac{0.100}{x^2} \tag{5.11}$$

$$v_R = -0.662 + \frac{0.917}{x} - \frac{0.050}{x^2} \tag{5.12}$$

$$D = D'(\ln(x) + v) \tag{5.13}$$

$$D_R = D'_R(\ln(x) + v_R) \tag{5.14}$$

A similar study conducted on gold nanorods with low aspect ratios compaed DLS results to theoretical results based on sizes measured from TEM.[34] They observed a bimodal correlation function and the fast and slow modes were attributed to the translational and rotational decays. Fitting the amplitudes led to size determination as opposed to using the relation: $\Gamma = q^2D + 6D_r$. Theoretical results from Ortega and Garcia de la Torre[35] differed from experimental by approximately 20% for rotational diffusion and 15% for translational.

Table 5.2 below shows the results calculated from the Broersma and Tirado equations based on an average length and width of fractions 40 and 46 measured from TEM. The model

Table 5.2 Comparison of translational and rotational diffusion coefficients and their corresponding radii calculated from the Stokes-Einstein relationship. Calculations are based on a TEM average (from fractions 40 and 46) length of 240 nm and width of 172 nm (axial ratio of 1.4).

	D_t (cm^2/s)	$R_{h,t}$ (nm)	D_r (s^{-1})	$R_{h,r}$ (nm)
Broersma	5.1×10^{-08}	48	1039	56
Tirado	2.0×10^{-08}	120	96	124

overestimates $R_{h,t}$ from DLS by 30%, but only by 16% for $R_{h,t}$ extracted from DDLS. In both cases it is large compared to $R_{h,r}$ which is only 3% higher than experimental values.

5.4 Depolarized Scattering from Metallic Particles

Magnetic hybrid particles with inclusions of either cobalt or iron oxide have been synthesized in this group and by others.[36-38] Investigations of whether these particles are capable of depolarizing light have begun by looking at the depolarization signal from the core metals alone. Particles suspended in ethanol were sonicated prior to analysis by polarized and depolarized scattering. A PTFE latex sample was created from a stock solution for comparison and all samples were measured at a single angle of 45°.

As expected, the latex curves have scattering well above the baseline for DLS/DDLS with a minimal amount of noise. In both U_V and H_V modes there are secondary decays from what is most likely aggregation even with brief sonication of the sample. The coherence of iron is similar to that of PTFE and, although it is noisy, the correlation function is capable of being fit by standard methods. The same could not be said for cobalt, whose signal is extremely noisy throughout. The log-lin plot has no distinct decay.

The decay rate of the PTFE particles is faster than for the metallic particles in U_V mode indicating that the metallic particles are larger in size. Based on the knowledge that PTFE particles have a hydrodynamic diameter of nearly 200 nm, it can be assumed that these aggregates are even larger. Magnetic inclusions in hybrid particles are much smaller, closer to 10 nm,[36] and it begs the question of whether particles a fraction of the size would depolarize light in the same capacity.
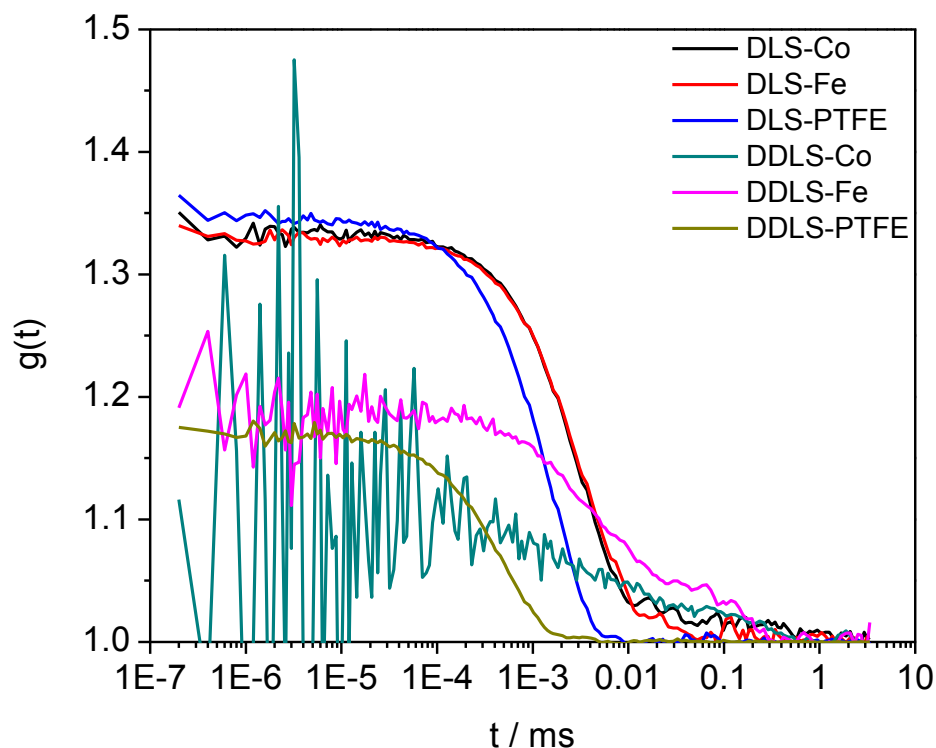
Figure 5.14 Correlation functions of polarized and depolarized light scattering for Cobalt and Iron particles with PTFE for comparison.

5.5 Conclusions and Future Work

Dynamic light scattering is sensitive enough to see small differences in average particle size even if the sample is polydisperse. Additionally, what appears to be end over end tumbling of colloidal PTFE is visible in DLS as indicated by the increasing slope with angle. AF4 is a quick and efficient size separation technique for improving the uniformity of PTFE particles prior to their use as diffusion probes of various complex fluids, but complexities arise in the computation of size. Spherical models are not well suited for rodlike particles, even at very low axial ratios, but neither are models intended for use with anisotropic particles that are typically only useful for axial ratios of two and above. Future work would include analysis of these particles by a method designed for particles of this type such as the zeno algorithm developed for particles of arbitrary shape.[39]

131

All experiments were conducted with surfactant in the stock solution. To determine the effects of surfactant on the separation the sample could be dialyzed with pure water then separated by AF4. Results from Sedimentation FFF showed that surfactant affected the separation ability. This proposed experiment may introduce additional complexities if it is not discernible whether a surfactant-free sample is not separated due to aggregation. If surfactant has a negative effect on the separation, then perhaps it would improve. Variation in surfactant type could also be explored.

Continued studies of hybrid particles with a depolarizing magnetic core would be recommended as this shows promise as interesting new probes in diffusion studies in a polypeptide matrix potentially gaining more information about the hybrid particle itself. Magnetite particles would be the most suitable candidate for these studies because of its high scattering signal. Comparisons could also be made about whether the thickness of the silica or polypeptide shell affects signal.

5.6 References

1.   Tervoort, T.; Visjager, J.; Graf, B.; Smith, P. Melt-Processable Poly(tetrafluoroethylene). *Macromolecules* 2000, 33, (17), 6460-6465.

2.   DuPont Aqueous Dispersions. http://www2.dupont.com/Teflon_Industrial/en_US/products/product_by_name/teflon_ptf p/aqueous.html.

3.   Nakajima, A.; Hashimoto, K.; Watanabe, T. Recent Studies on Super-Hydrophobic Films. *Monatshefte fuer Chemie* 2001, 132, (1), 31-41.

4.   Pu, F. R.; Williams, R. L.; Markkula, T. K.; Hunt, J. A. Effects of plasma treated PET and PTFE on expression of adhesion molecules by human endothelial cells in vitro. *Biomaterials* 2002, 23, (11), 2411-2428.

5.   Goessi, M.; Tervoort, T.; Smith, P. Melt-spun poly(tetrafluoroethylene) fibers. *J Mater Sci* 2007, 42, (19), 7983-7990.

6.   Cui, X.; Zhong, S.; Xu, J.; Wang, H. Synthesis of polytetrafluoroethylene/polyacrylate core-shell nanoparticles via emulsifier-free seeded emulsion polymerization. *Colloid & Polymer Science* 2007, 285, (8), 935-940.

7.   Huang, Q.; Xiao, C.; Hu, X. A novel method to prepare hydrophobic poly(tetrafluoroethylene) membrane, and its properties. *J Mater Sci* 2010, 45, (24), 6569-6573.

8.   Bashford, D. P., *Thermoplastics Directory and Databook*. Chapman & Hall: London, UK, 1997.

9.   Noda, Y.; Hosokawa, K.; Mizuno, T.; Ihara, K.; Shimizu, T. Polytetrafluoroethylene fine particles and powder. 5,324,785, June 28, 1994, 1994.

10.   Ottewill, R.; Rance, D. Studies on polytetrafluoroethylene latices Part 3. Electrophoretic mobility in univalent electrolytes. *Colloid & Polymer Science* 1986, 264, (11), 982-991.

11.   Eimer, W.; Williamson, J. R.; Boxer, S. G.; Pecora, R. Characterization of the overall and internal dynamics of short oligonucleotides by depolarized dynamic light scattering and NMR relaxation measurements. *Biochemistry* 1990, 29, (3), 799-811.

12.   Schillen, K.; Brown, W.; Johnsen, R. M. Micellar Sphere-to-Rod Transition in an Aqueous Triblock Copolymer System. A Dynamic Light Scattering Study of Translational and Rotational Diffusion. *Macromolecules* 1994, 27, (17), 4825-4832.

13.   Camins, B.; Russo, P. S. Following Polymer Gelation by Depolarized Dynamic Light Scattering from Optically and Geometrically Anisotropic Latex Particles. *Langmuir* 1994, 10, (11), 4053-4059.

14.   Bolisetty, S.; Harnau, L.; Jung, J.-m.; Mezzenga, R. Gelation, Phase Behavior, and Dynamics of β-Lactoglobulin Amyloid Fibrils at Varying Concentrations and Ionic Strengths. *Biomacromolecules* 2012, 13, (10), 3241-3252.

15.   Cavicchi, R. E.; Meier, D. C.; Presser, C.; Prabhu, V. M.; Guha, S. Single Laser Pulse Effects on Suspended-Au-Nanoparticle size Distributions and Morphology. *The Journal of Physical Chemistry C* 2013.

16.   Eitoku, T.; Tange, M.; Kato, H.; Okazaki, T. Depolarized dynamic light scattering study of multi-walled carbon nanotubes in solution. *Materials Express* 2013, 3, (1), 37-42.

17.   Koenderink, G. H.; Philipse, A. P. Rotational and Translational Self-Diffusion in Colloidal Sphere Suspensions and the Applicability of Generalized Stokes-Einstein Relations. *Langmuir* 2000, 16, (13), 5631-5638.

18. Koenderink, G. H.; Sacanna, S.; Aarts, D. G. A. L.; Philipse, A. P. Rotational and translational diffusion of fluorocarbon tracer spheres in semidilute xanthan solutions. *Physical Review E* 2004, 69, (2), 021804.

19. Koenderink, G. H.; Aarts, D. G. A. L.; de Villeneuve, V. W. A.; Philipse, A. P.; Tuinier, R.; Lekkerkerker, H. N. W. Morphology and Kinetics of Phase Separating Transparent Xanthan-Colloid Mixtures. *Biomacromolecules* 2003, 4, (1), 129-136.

20. Piazza, R.; Iacopini, S.; Pierno, M.; Vignati, E. Depletion-induced fractionation of optically anisotropic particles. *Journal of Physics: Condensed Matter* 2002, 14, (33), 7563.

21. Phillies, G. D. J.; Pirnat, T.; Kiss, M.; Teasdale, N.; Maclung, D.; Inglefield, H.; Malone, C.; Rau, A.; Yu, L. P.; Rollings, J. Probe diffusion in solutions of low-molecular-weight polyelectrolytes. *Macromolecules* 1989, 22, (10), 4068-4075.

22. Phillies, G. D. J.; Gong, J.; Li, L.; Rau, A.; Zhang, K.; Yu, L. P.; Rollings, J. Macroparticle diffusion in dextran solutions. *The Journal of Physical Chemistry* 1989, 93, (16), 6219-6223.

23. Choi, Y. W.; Lee, S.; Kim, K.; Russo, P. S.; Sohn, D. Probe diffusion from dilute to concentrated in polyelectrolyte solution: Salt effect. *Journal of colloid and interface science* 2007, 313, (2), 469-475.

24. Sohn, D.; Russo, P. S.; Dávila, A.; Poche, D. S.; McLaughlin, M. L. Light Scattering Study of Magnetic Latex Particles and Their Interaction with Polyelectrolytes. *Journal of Colloid and Interface Science* 1996, 177, (1), 31-44.

25. Kato, H.; Nakamura, A.; Takahashi, K.; Kinugasa, S. Accurate Size and Size-Distribution Determination of Polystyrene Latex Nanoparticles in Aqueous Medium Using Dynamic Light Scattering and Asymmetrical Flow Field Flow Fractionation with Multi-Angle Light Scattering. *Nanomaterials* 2012, 2, 15-30.

26. Lenti, D.; Carignano, G. Lubricant compositions based on PTFE. 2001.

27. Visca, M.; Lenti, D.; Malvasi, M.; Marchese, E. Fluoropolymer dispersions. 2006.

28. Ebnesajjad, S., *Fluoroplastics, Volume 1: Non-Melt Processible Fluoroplastics*. William Andrew: 2000; Vol. 1.

29. Atta, K. R.; Gavril, D.; Loukopoulos, V.; Karaiskakis, G. Study of the influence of surfactants on the transfer of gases into liquids by inverse gas chromatography. *Journal of Chromatography A* 2004, 1023, (2), 287-296.

30. Russo, P. S.; Saunders, M. J.; DeLong, L. M.; Kuehl, S.; Langley, K. H.; Detenbeck, R. W. Zero-angle depolarized light scattering of a colloidal polymer. *Analytica Chimica Acta* 1986, 189, 69-87.

31. Riseman, J.; Kirkwood, J. G. The Intrinsic Viscosity, Translational and Rotatory Diffusion Constants of Rod-Like Macromolecules in Solution. *The Journal of Chemical Physics* 1950, 18, (4), 512-516.

32. Russo Paul, S., Dynamic light scatering from rigid and nearly rigid rods. In *Dynamic Light Scattering, the Method and Some Applications*, Brown, W., Ed. Oxford: New York, 1993; pp 512-553.

33. Broersma, S. Rotational Diffusion Constant of a Cylindrical Particle. *Journal of Chemical Physics* 1960, 32, (6), 1626-1631.

34. Rodríguez-Fernández, J.; Pérez−Juste, J.; Liz−Marzán, L. M.; Lang, P. R. Dynamic Light Scattering of Short Au Rods with Low Aspect Ratios. *The Journal of Physical Chemistry C* 2007, 111, (13), 5020-5025.

35. Ortega, A.; Garcia de la Torre, J. Hydrodynamic properties of rodlike and disklike particles in dilute solution. *The Journal of Chemical Physics* 2003, 119, (18), 9914-9919.

36. Turksen, S. Synthesis and Characterization of Superparamagnetic Silica-Homopolypeptide Composite Particles. Louisiana State University, Baton Rouge, LA, 2004.

37. Nagao, D.; Yokoyama, M.; Saeki, S.; Kobayashi, Y.; Konno, M. Preparation of composite particles with magnetic silica core and fluorescent polymer shell. *Colloid & Polymer Science* 2008, 286, (8), 959-964.

38. Li, G.; Zeng, D. L.; Wang, L.; Baoyu; Zong; Neoh, K. G.; Kang, E. T. Hairy Hybrid Nanoparticles of Magnetic Core, Fluorescent Silica Shell, and Functional Polymer Brushes. *Macromolecules* 2009, 42, (21), 8561-8565.

39. Kang, E.-H.; Mansfield, M. L.; Douglas, J. F. Numerical path integration technique for the calculation of transport properties of proteins. *Physical Review E* 2004, 69, (3), 031918.

APPENDIX A. POLARIZED OPTICAL MICROSCOPY FOR PHASE DIAGRAMS

A.1 Fluorescent, magnetic silica (50 nm diameter)/PBLG/Pyridine
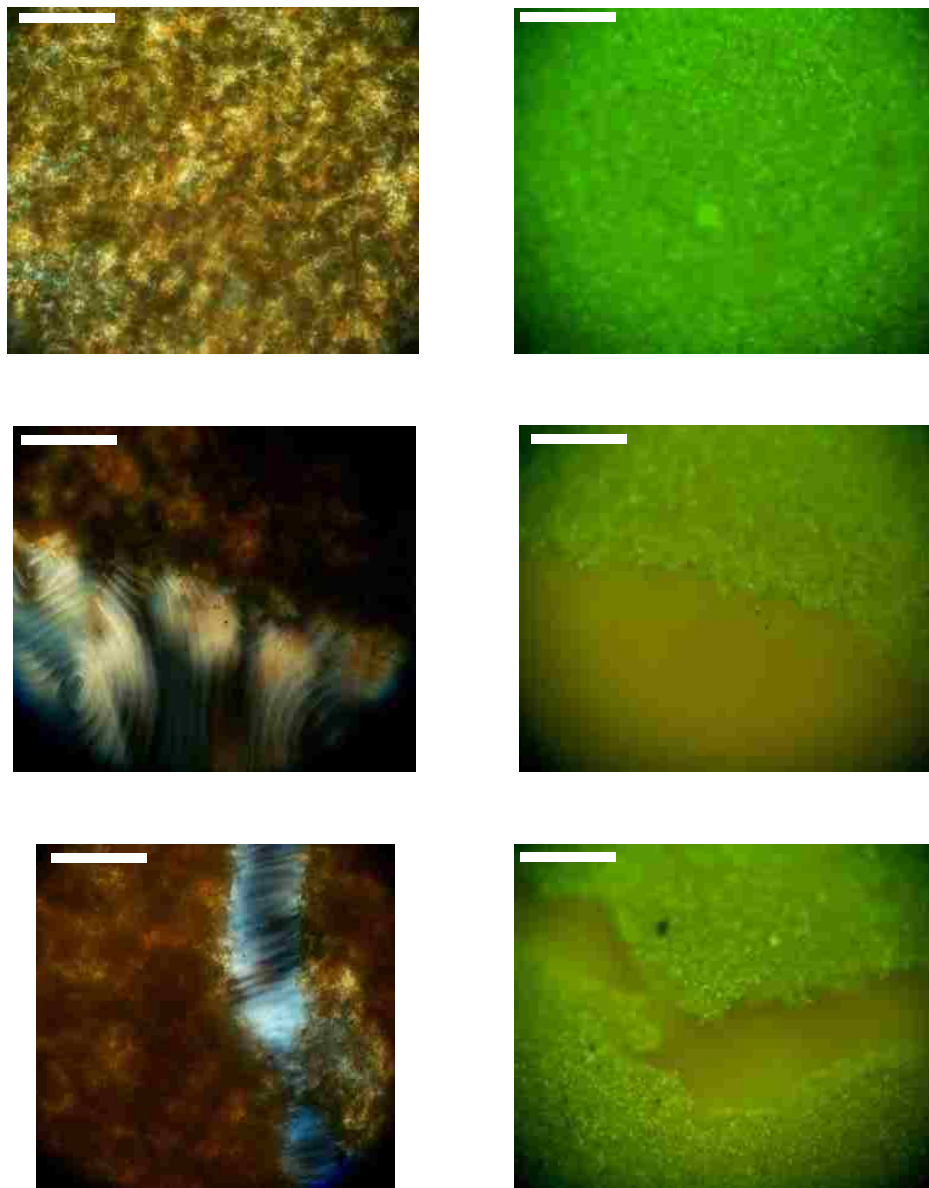
Figure A1.1 Composition: 26 wt% PBLG, 7 wt% silica, 67 wt% pyridine. (MC.1.5A) Photographs on the right are of fluorescent microscopy. Scale bar is 100 microns.
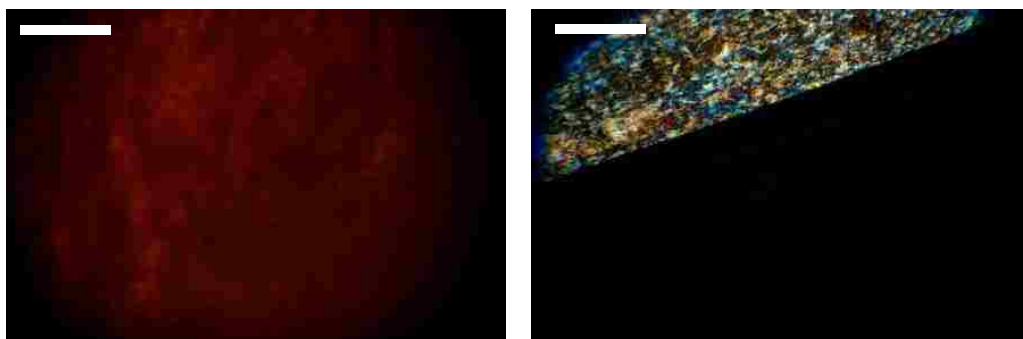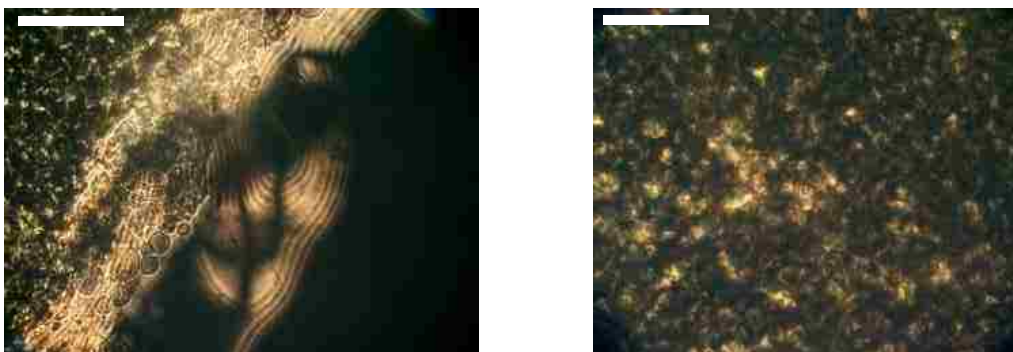
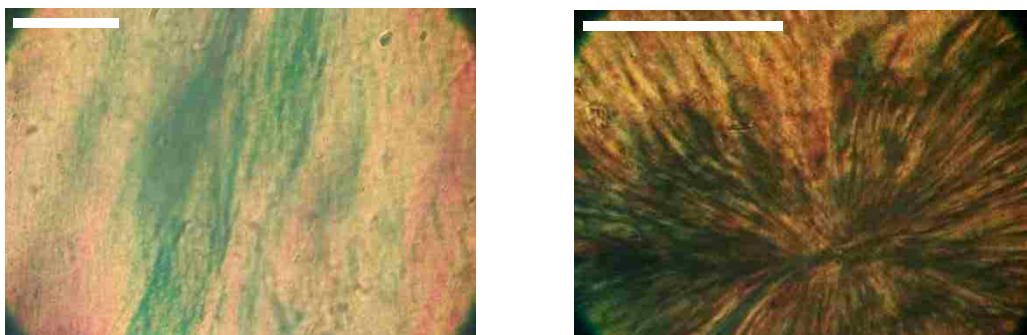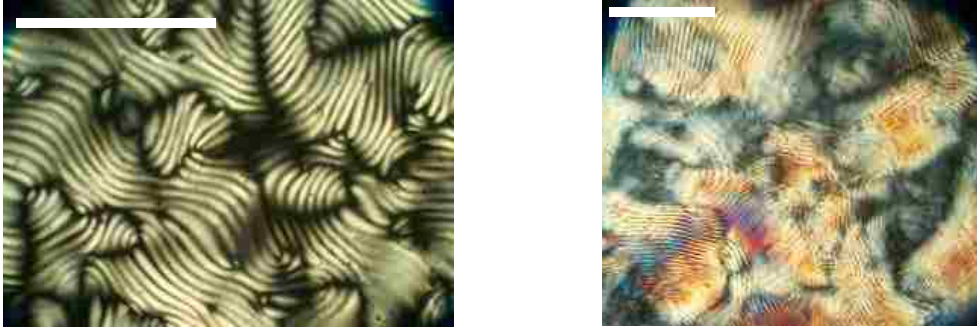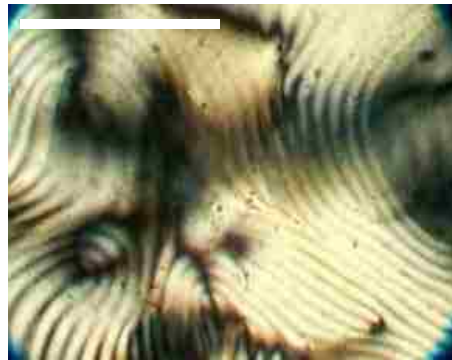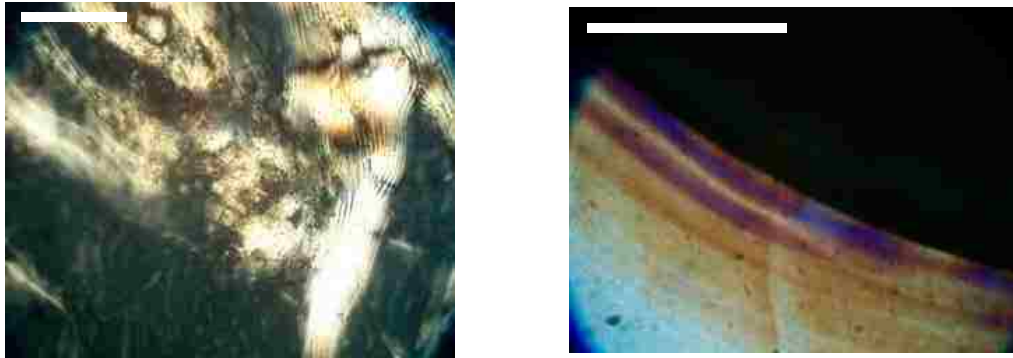Figure A1.2 Composition: 22 wt% PBLG, 6 wt% silica, 72 wt% pyridine. (MC.1.5B) Scale bar is 100 microns.
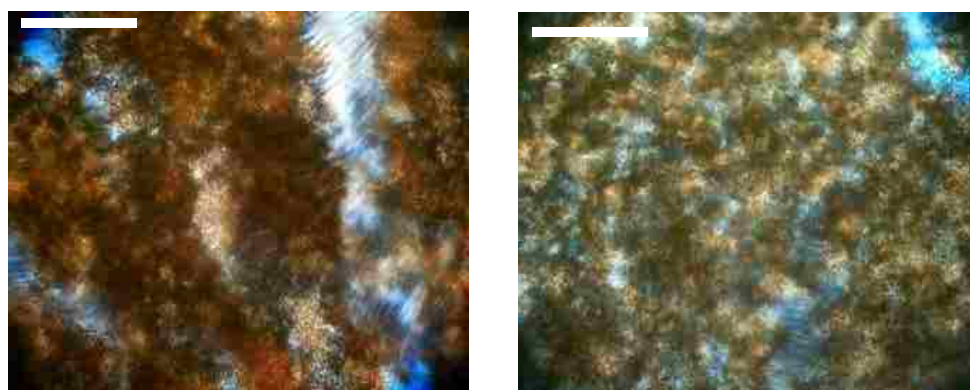
Figure A1.3 Composition: 19 wt% PBLG, 5 wt% silica, 76 wt% pyridine. (MC.1.15C) Scale bar is 100 microns.
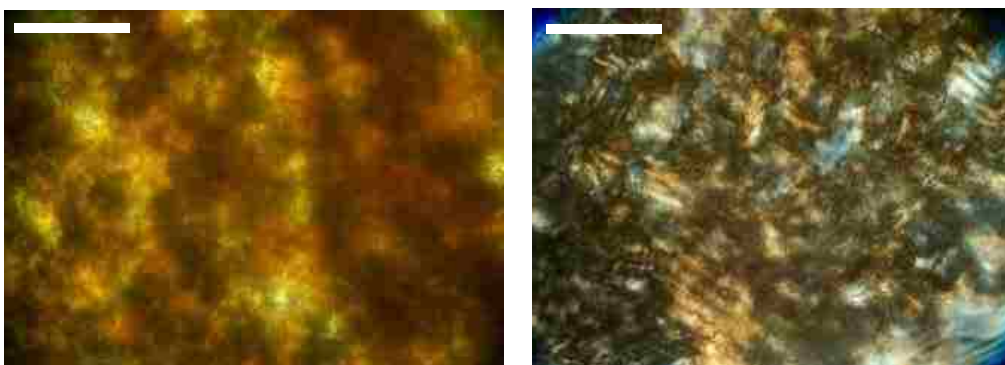
Figure A1.4 Composition: 16 wt% PBLG, 4 wt% silica, 80 wt% pyridine. (MC.1.5D) Scale bar is 100 microns.
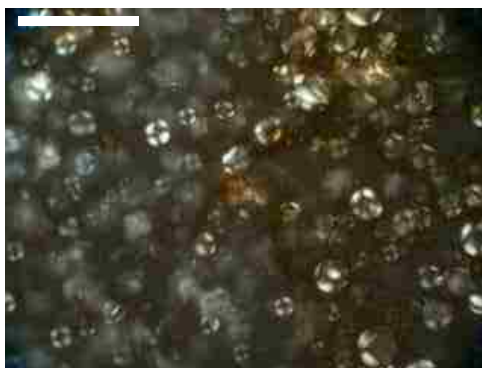
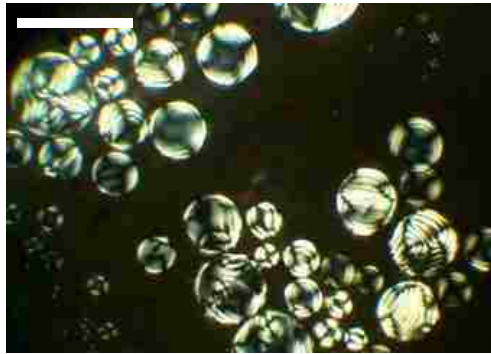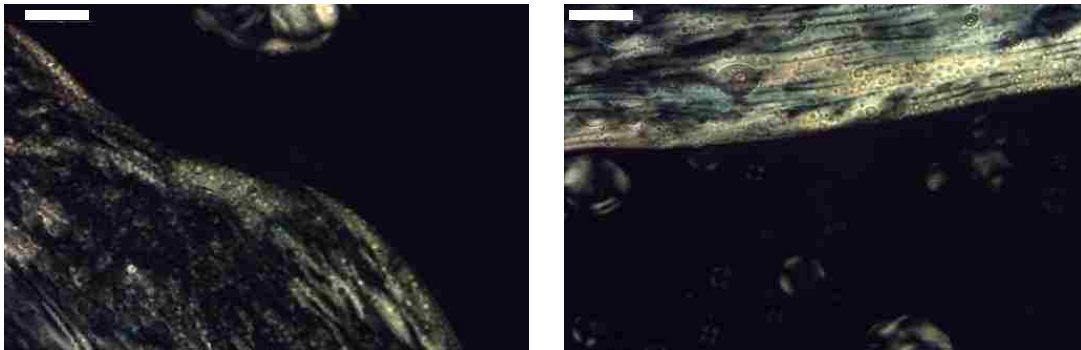Figure A1.5 Composition: 14 wt% PBLG, 4 wt% silica, 82 wt% pyridine. (MC.1.5E) Scale bar is 100 microns.
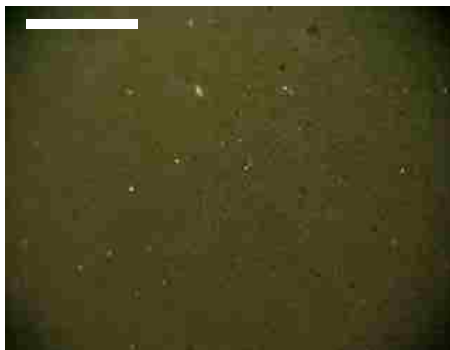
Figure A1.6 Composition: 12 wt% PBLG, 3 wt% silica, 85 wt% pyridine. (MC.1.5F) Scale bar is 100 microns.
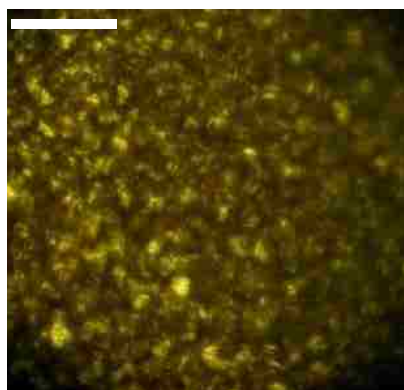
Figure A1.7 Composition: 11.6 wt% PBLG, 8 wt% silica, 80.4 wt% pyridine. (MC.1.7A) Scale bar is 100 microns.

Figure A1.8 Composition: 10.5 wt% PBLG, 7.3 wt% silica, 82.2 wt% pyridine. (MC.1.7B) All other isotropic samples look similar to this one. See table A1.1 below. Scale bar is 100 microns.

Table A1.1 Compositions for isotropic samples in phase diagram for 50 nm (diameter) silica.

| Sample Name	wt% PBLG	wt% Silica	wt% Pyridine
MC.1.7C	9.5	6.5	84
MC.1.7D	8.1	5.6	86.3
MC.1.7E	6.6	4.6	88.8
MC.1.8A	5.1	10.6	84.3
MC.1.8B	6	12.3	81.7
MC.1.8C	6.3	12.9	80.8
MC.1.21A	4.2	26.7	69.1
MC.1.21B	4.5	28.8	66.7
MC.1.21C	4.8	30.4	64.8

A.2 Silica (150 nm diameter)/PBLG/Pyridine
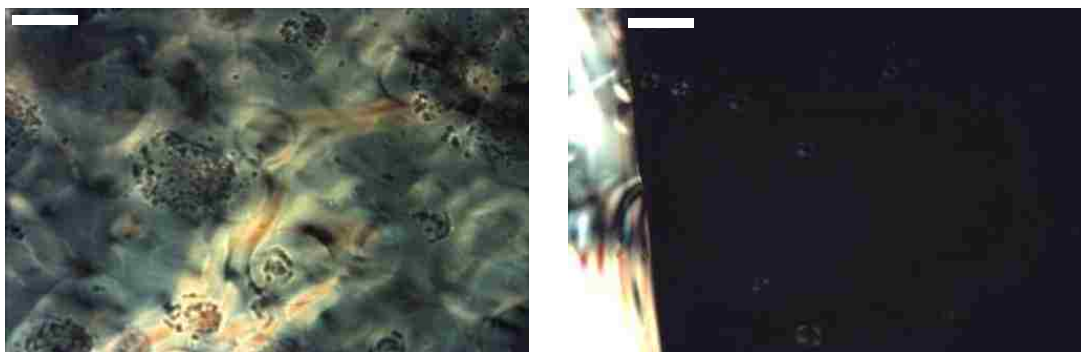
Figure A2.1 Composition: 15.6 wt% PBLG, 6.8 wt% silica, 77.6 wt% pyridine. (MC.1.6A) Scale bar is 100 microns.
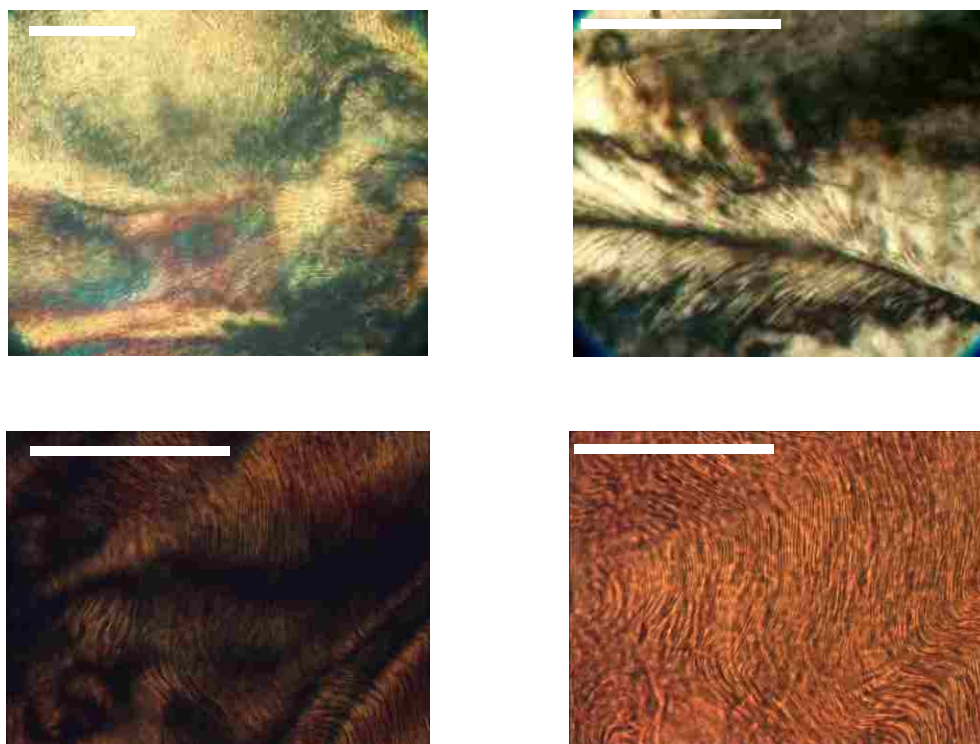
Figure A2.2 Composition: 20.7 wt% PBLG, 21.0 wt% silica, 58.3 wt% pyridine. (MC.1.15D) Photographs on the bottom row are of the same spot on the sample, with and without crossed polarizers. Scale bar is 100 microns.

Figure A2.3 Composition: 15.3 wt% PBLG, 15.6 wt% silica, 69.1 wt% pyridine. (MC.1.15C) Scale bar is 100 microns.

Figure A2.4 Composition: 21.7 wt% PBLG, 22.1 wt% silica, 56.2 wt% pyridine. (MC.1.15E) Scale bar is 100 microns.

Figure A2.5 Composition: 31.9 wt% silica, 68.1 wt% pyridine. (MC.1.16A) Scale bar is 100 microns.

Figure A2.6 Composition: 26.9 wt% PBLG, 2.9 wt% silica, 70.2 wt% pyridine. (MC.1.17A) Scale bar is 100 microns.

Figure A2.7 Composition: 24.0 wt% PBLG, 2.6 wt% silica, 73.4 wt% pyridine. (MC.1.17B) Scale bar is 100 microns.
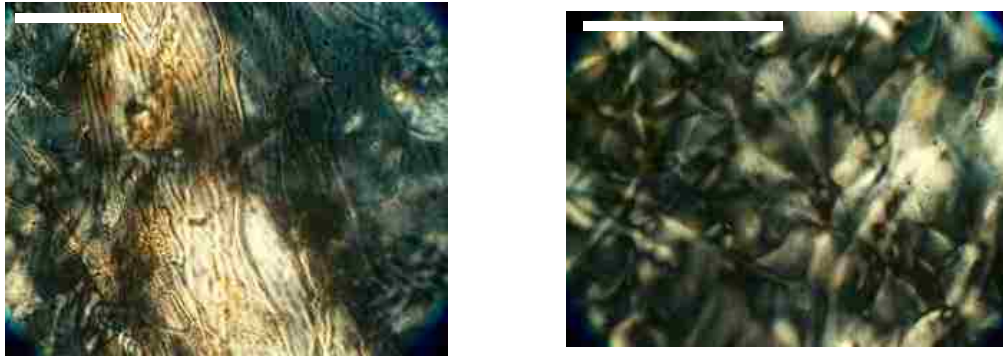
Figure A2.8 Composition: 19.4 wt% PBLG, 2.1 wt% silica, 78.4 wt% pyridine. (MC.1.17D) Scale bar is 100 microns.


Figure A2.9 Composition: 17.2 wt% PBLG, 1.9 wt% silica, 80.9 wt% pyridine. (MC.1.17E) Scale bar is 100 microns.

Figure A2.10 Composition: 14.6 wt% PBLG, 14.4 wt% silica, 71.0 wt% pyridine. (MC.1.18B) Scale bar is 100 microns.
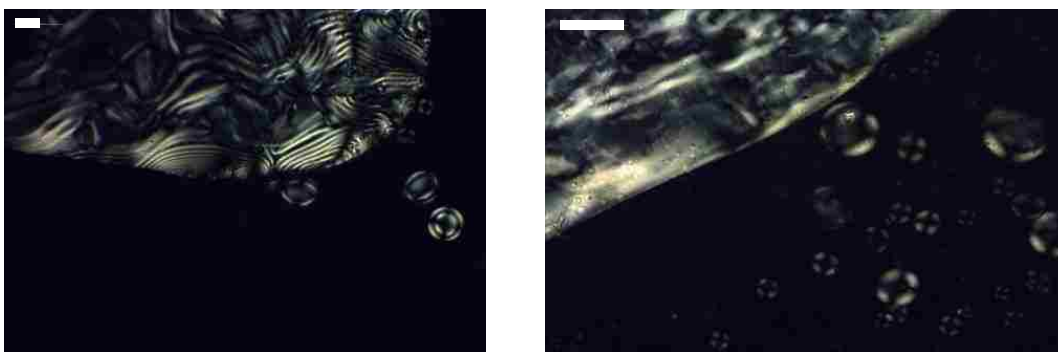
Figure A2.11 Composition: 13.9 wt% PBLG, 13.7 wt% silica, 72.4 wt% pyridine. (MC.1.18C) Scale bar is 100 microns.

Table A2.1 Compositions for isotropic samples in phase diagram for 150 nm (diameter) silica.

Sample Name	wt% PBLG	wt% Silica	wt% Pyridine
MC.1.6B	13.6	5.9	80.5
MC.1.6C	11.8	5.1	83.1
MC.1.6D	10.8	4.7	84.5
MC.1.15A	11.0	11.1	77.9
MC.1.15B	13.3	13.5	73.2
MC.1.17F	14.8	1.6	83.6
MC.1.17G	12.9	1.4	85.7
MC.1.18D	13.3	13.1	73.6
MC.1.18E	12.6	12.4	75.0
MC.1.18F	11.9	11.8	76.3
MC.1.18G	11.3	11.1	77.6
MC.1.19A	5.2	9.5	85.3
MC.1.19B	5.8	10.6	83.6
MC.1.19C	5.8	10.7	83.5
MC.1.19E	6.5	11.9	81.5
MC.1.20A	3.1	25.1	71.8

A.3 400 nm diameter silica-PBLG/PBLG/Pyridine
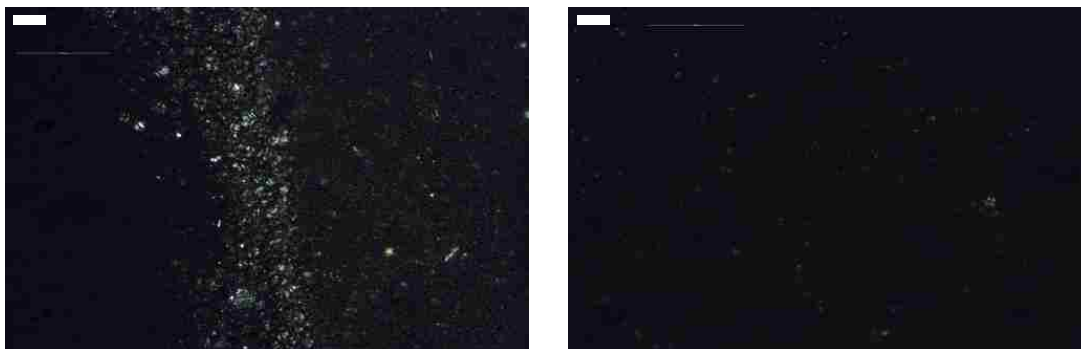
Figure A3.1 Composition: 16.7 wt% PBLG, 16.5 wt% silica, 66.8 wt% pyridine. (MC.1.41D) Scale bar is 100 microns.
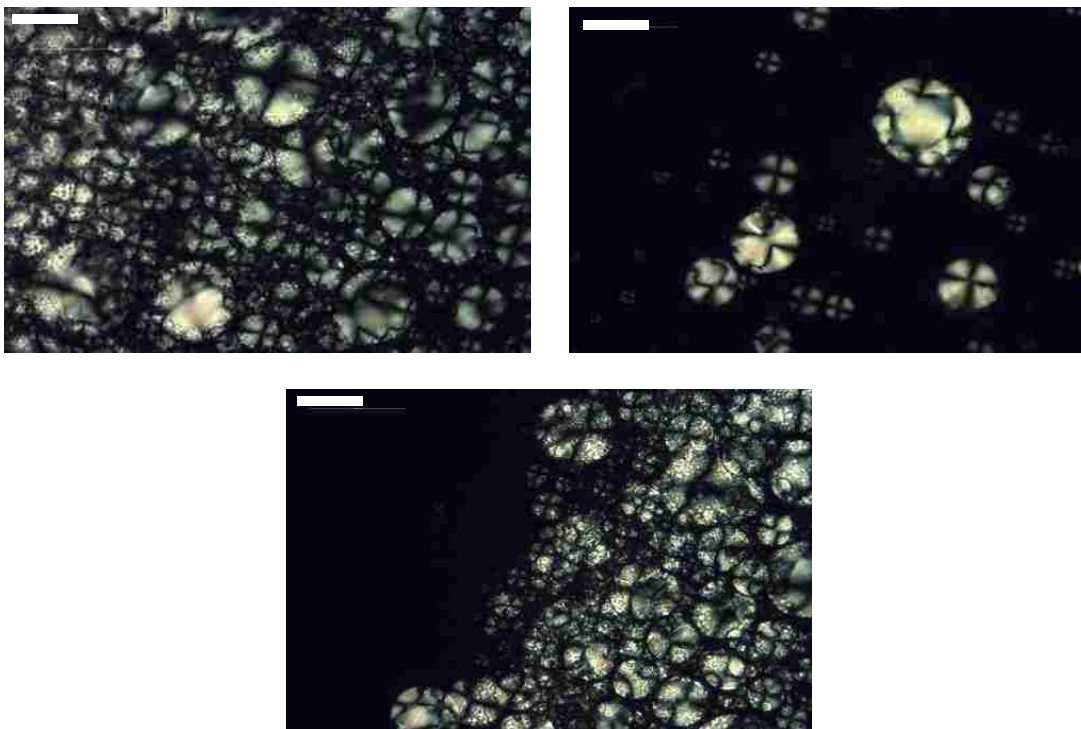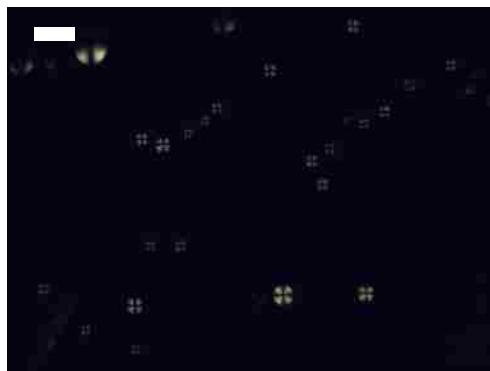

Figure A3.2 Composition: 17.2 wt% PBLG, 16.9 wt% silica, 65.9 wt% pyridine. (MC.1.41E) Scale bar is 100 microns.
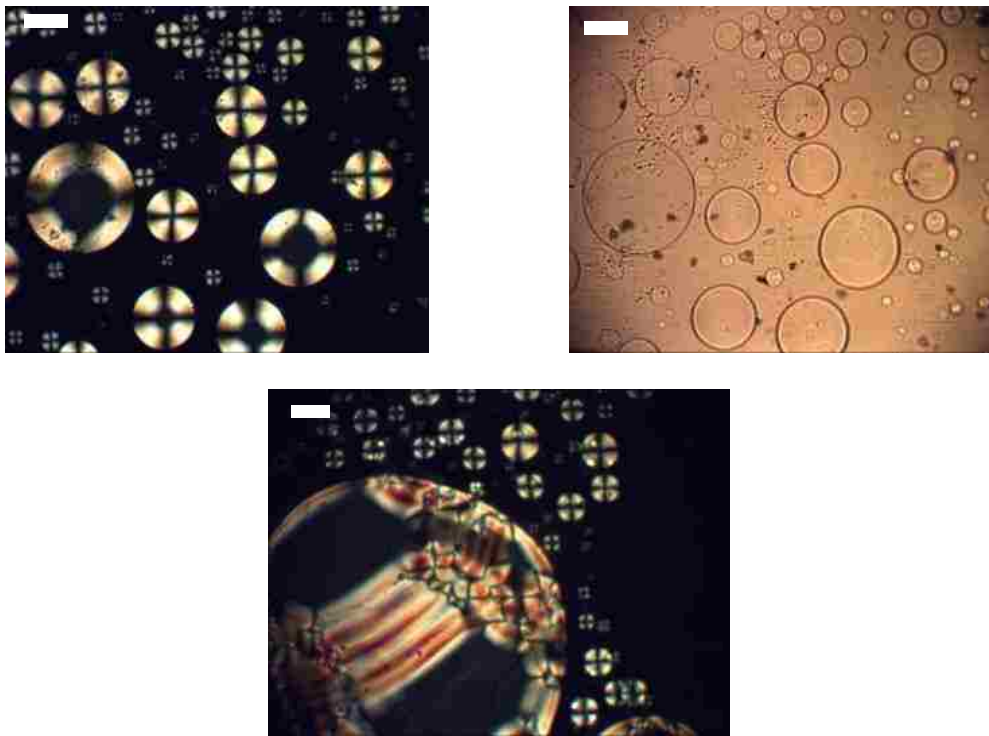
Figure A3.3 Composition: 23.0 wt% PBLG, 22.6 wt% silica, 54.4 wt% pyridine. (MC.1.41F) Photograph on the right is the same spot in the sample as on the left, but without crossed polarizers. Scale bar is 100 microns.

Figure A3.4 Composition: 4.7 wt% PBLG, 29.4 wt% silica, 65.9 wt% pyridine. (MC.1.44A) Scale bar is 100 microns.
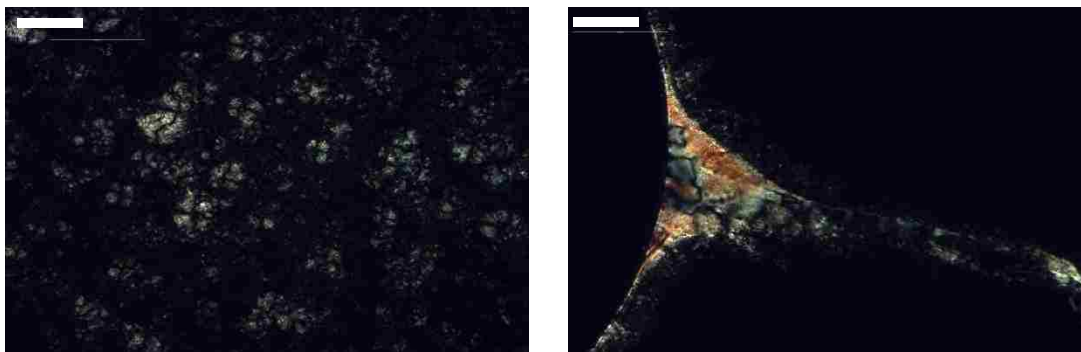
Figure A3.5 Composition: 5.3 wt% PBLG, 33.5 wt% silica, 61.2 wt% pyridine. (MC.1.44B) Scale bar is 100 microns.
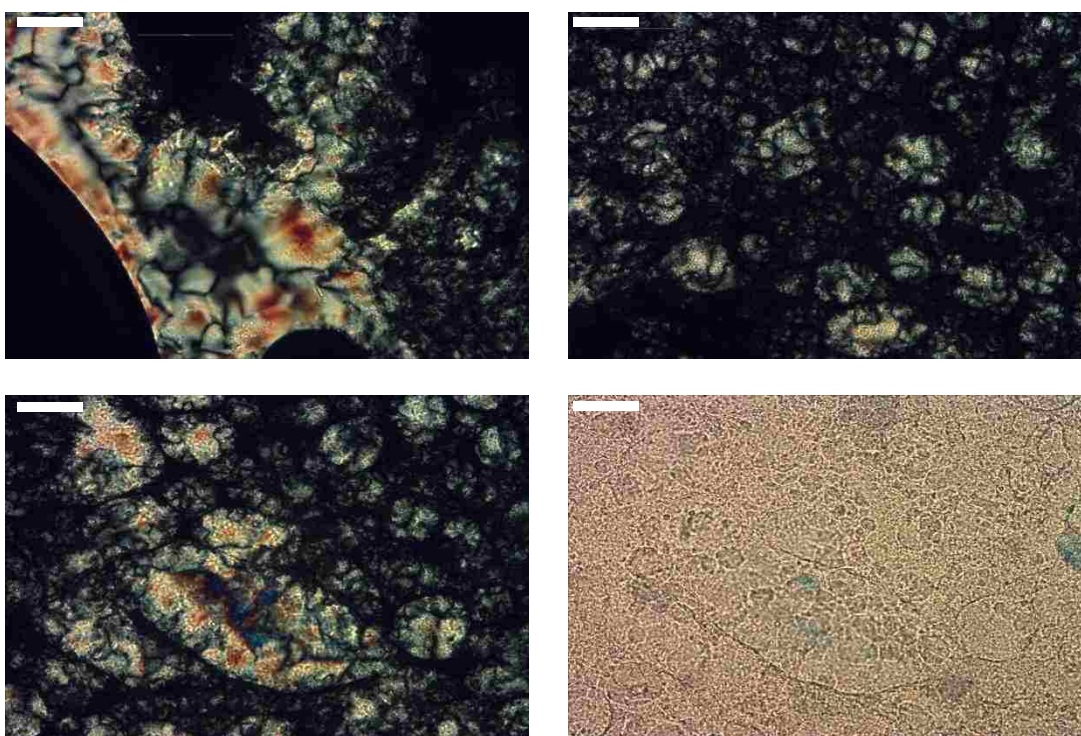
Figure A3.6 Composition: 5.9 wt% PBLG, 37.3 wt% silica, 56.8 wt% pyridine. (MC.1.44C) Photographs on the bottom row are of the same spot on the sample, with and without crossed polarizers. Scale bar is 100 microns.

147
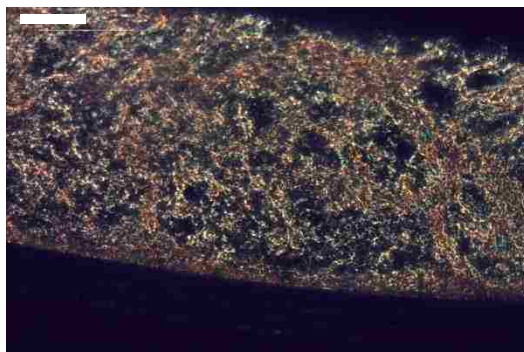
Figure A3.7 Composition: 6.4 wt% PBLG, 40.3 wt% silica, 53.3 wt% pyridine. (MC.1.44D) Scale bar is 100 microns.
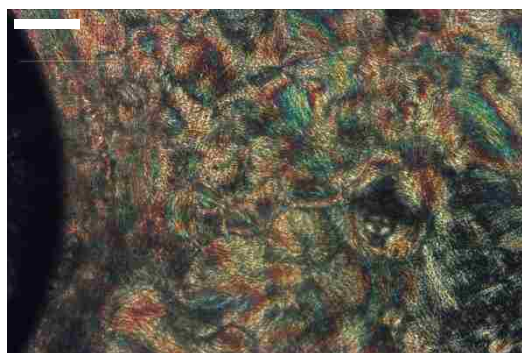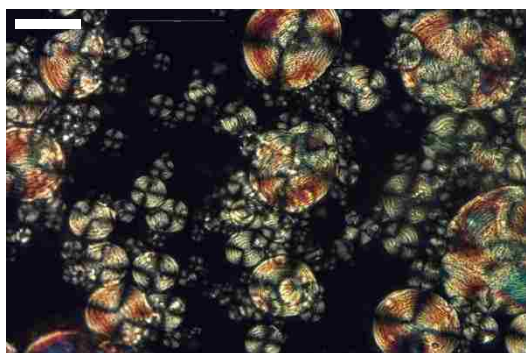
Figure A3.8 Composition: unknown. (MC.1.44E) Scale bar is 100 microns.

Figure A3.9 Composition: 8.9 wt% PBLG, 16.1 wt% silica, 75.0 wt% pyridine. (MC.1.45B) Scale bar is 150 microns.
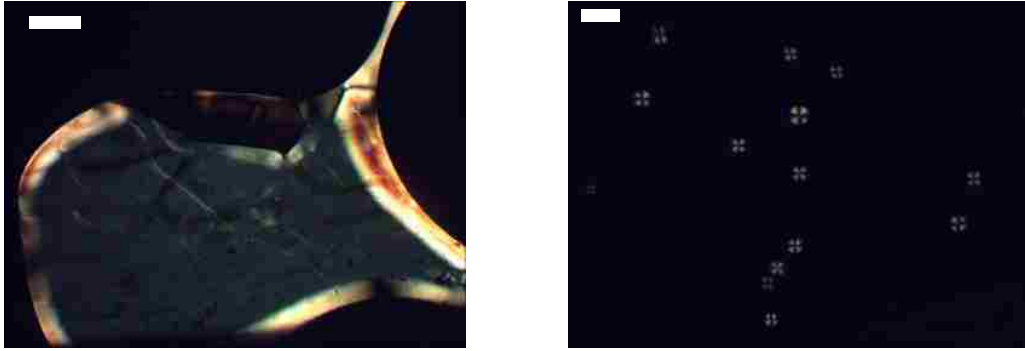
Figure A3.10 Composition: 9.7 wt% PBLG, 17.5 wt% silica, 772.8 wt% pyridine. (MC.1.45C) Scale bar is 150 microns.


Figure A3.11 Composition: 10.5 wt% PBLG, 18.9 wt% silica, 70.6 wt% pyridine. (MC.1.45D) Photographs on the top row are of the same spot on the sample, with and without crossed polarizers. Scale bar is 150 microns.
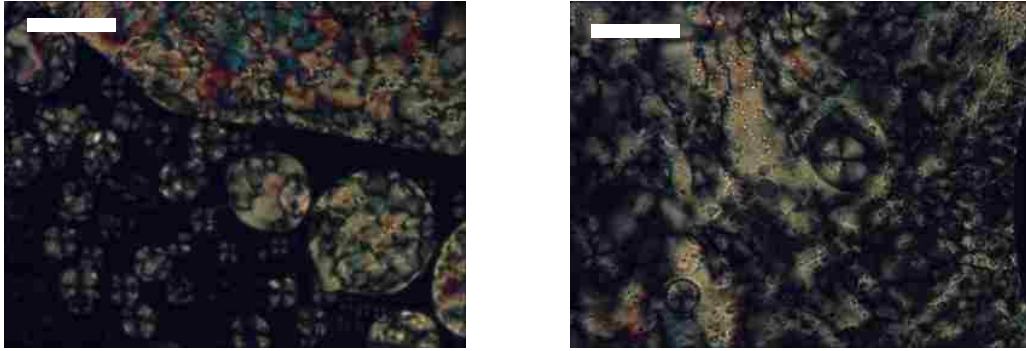
Figure A3.12 Composition: 14.2 wt% PBLG, 25.6 wt% silica, 60.2 wt% pyridine. (MC.1.45F) Scale bar is 150 microns.
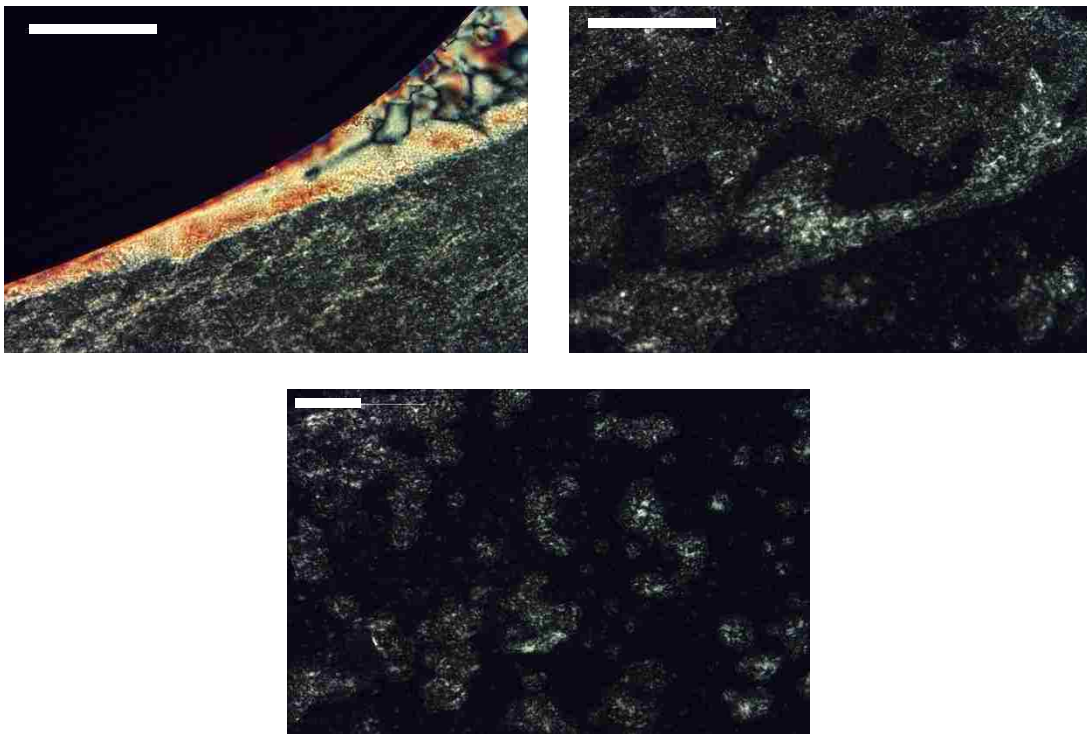
Figure A3.13 Composition: 14.2 wt% PBLG, 25.6 wt% silica, 60.2 wt% pyridine. (MC.1.46F) Scale bar is 100 microns.
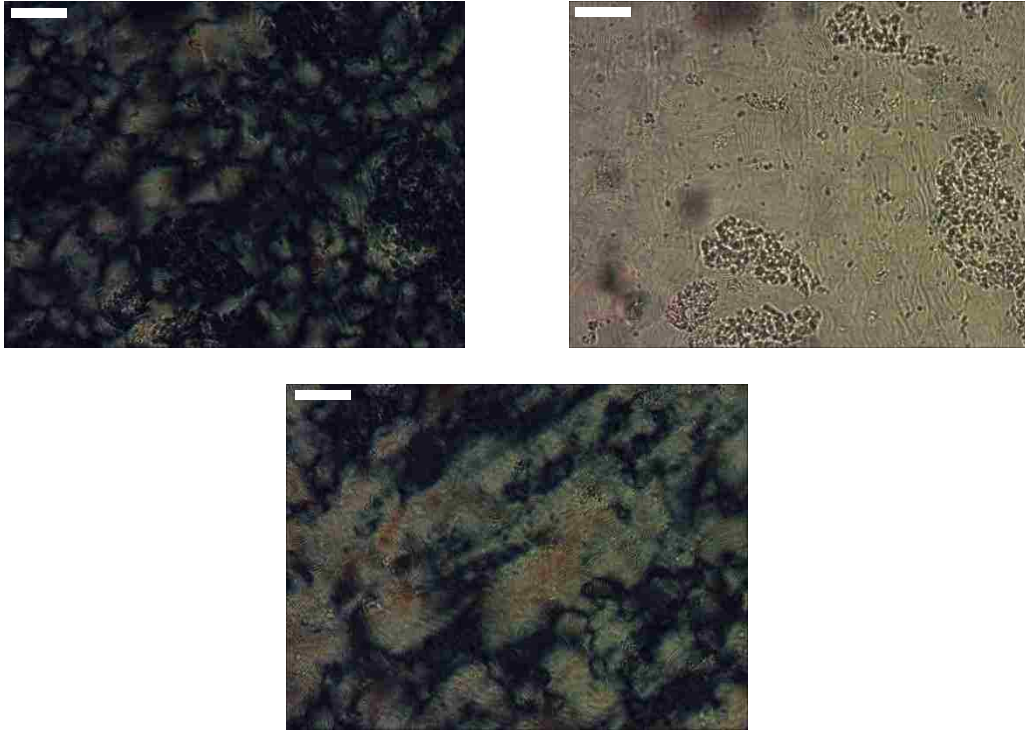
Figure A3.14 Composition: 30.8 wt% PBLG, 6.4 wt% silica, 62.8 wt% pyridine. (MC.1.51A) Top row is the same position with and without crossed polars. Scale bar is 100 microns.
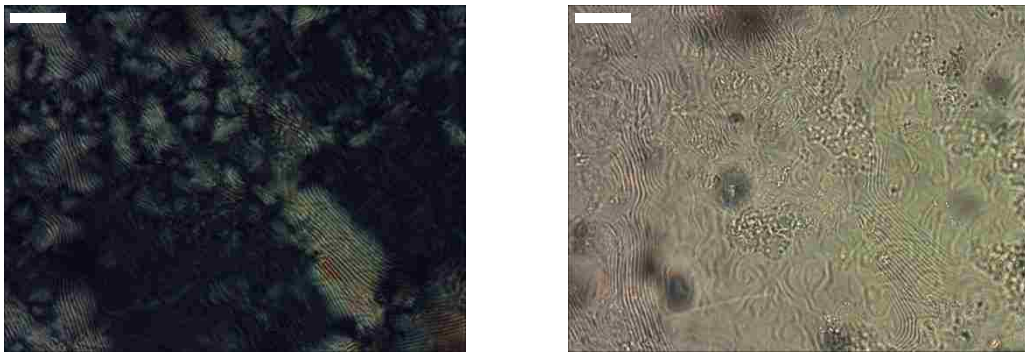

Figure A3.15 Composition: 26.8 wt% PBLG, 5.6 wt% silica, 67.6 wt% pyridine. (MC.1.51B) Scale bar is 100 microns.
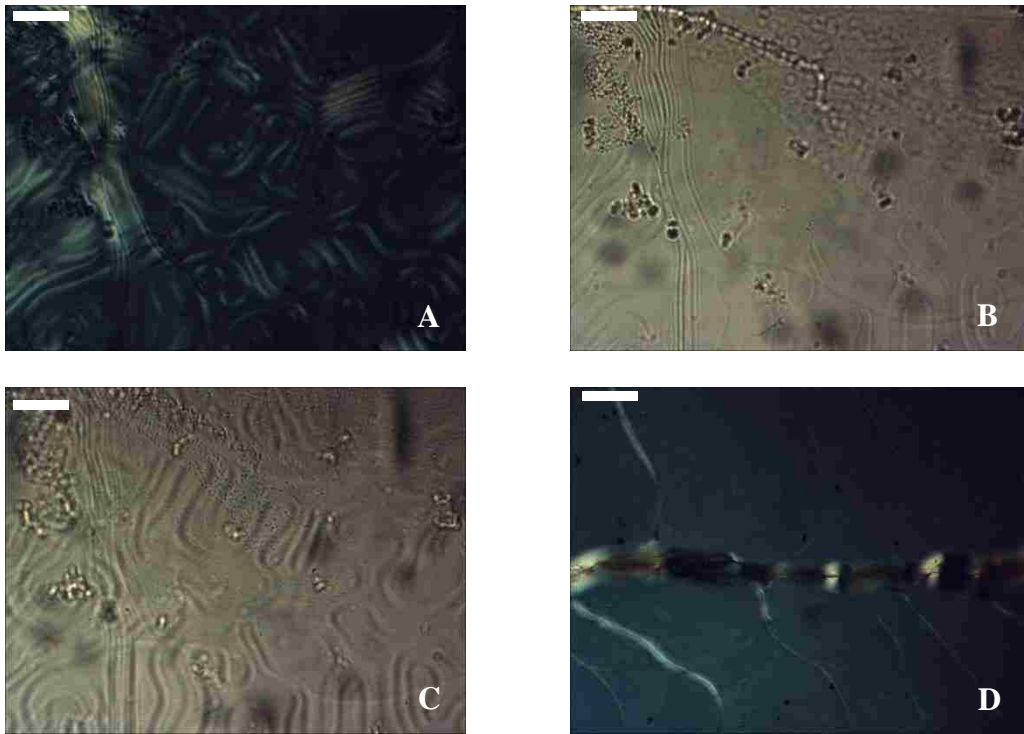
Figure A3.16 Composition: 23.2 wt% PBLG, 4.8 wt% silica, 72.0 wt% pyridine. (MC.1.51C) A, B and C are all at the same position. B and C are without crossed polars and differ by focusing depth. Scale bar is 100 microns.
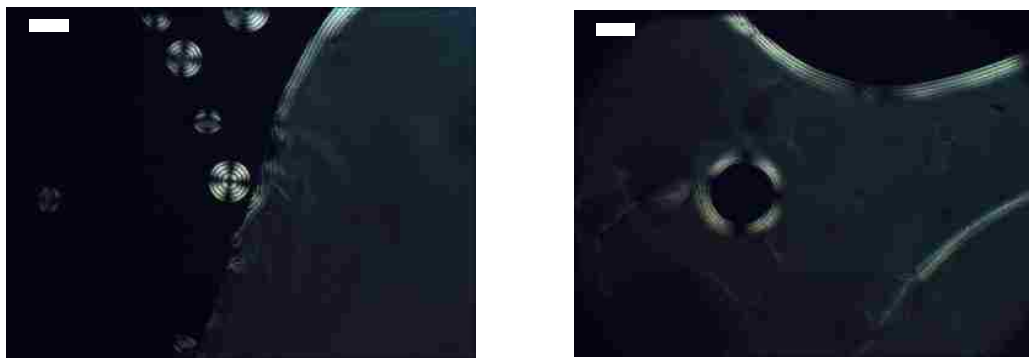

Figure A3.17 Composition: 18.0 wt% PBLG, 3.8 wt% silica, 78.2 wt% pyridine. (MC.1.51D) Scale bar is 100 microns.
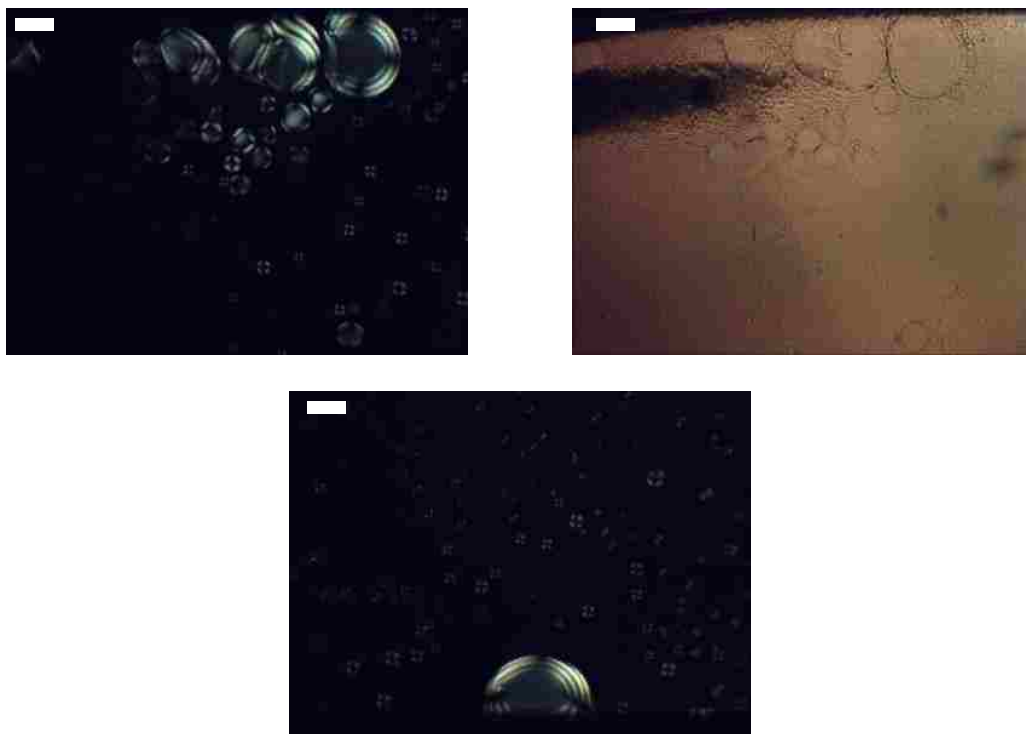
Figure A3.18 Composition: 14.5 wt% PBLG, 3.0 wt% silica, 82.5 wt% pyridine. (MC.1.51E) Scale bar is 100 microns.
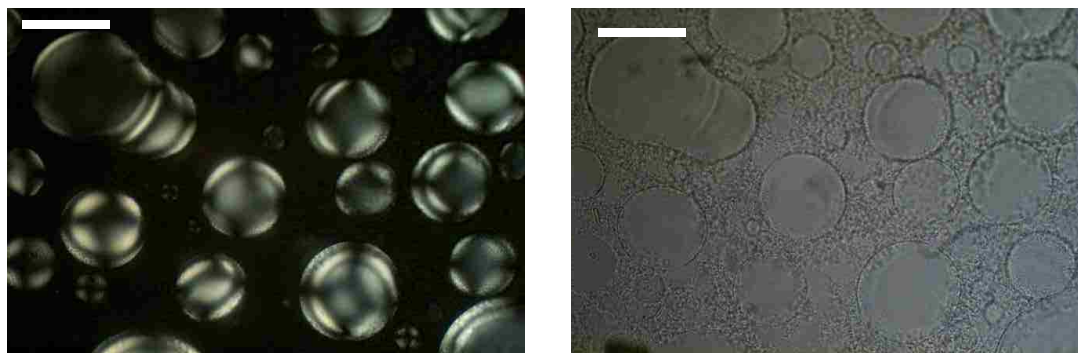

Figure A3.19 Composition: 12.1 wt% PBLG, 7.8 wt% silica, 80.1 wt% pyridine. (MC.1.52A) Same position on the sample with and without crossed polars. Scale bar is 100 microns.
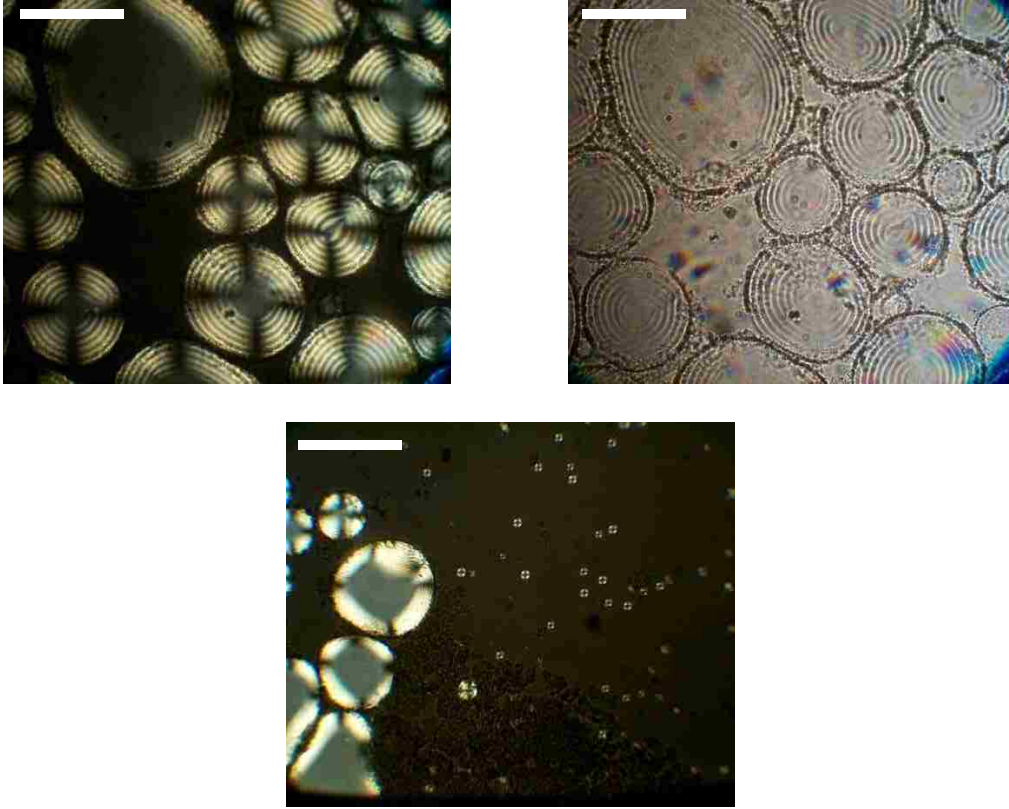
Figure A3.20 Composition: 30.8 wt% PBLG, 6.4 wt% silica, 62.8 wt% pyridine. (MC.1.52B) Top row is the same position with and without crossed polars. Scale bar is 100 microns.
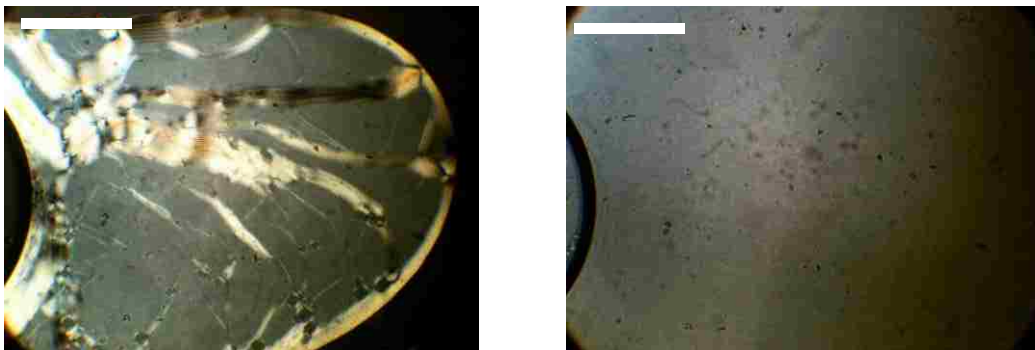

Figure A3.21 Composition: 14.4 wt% PBLG, 9.3 wt% silica, 76.3 wt% pyridine. (MC.1.52C) Photographs are of the same spot on the sample, with and without crossed polarizers. Scale bar is 200 microns.
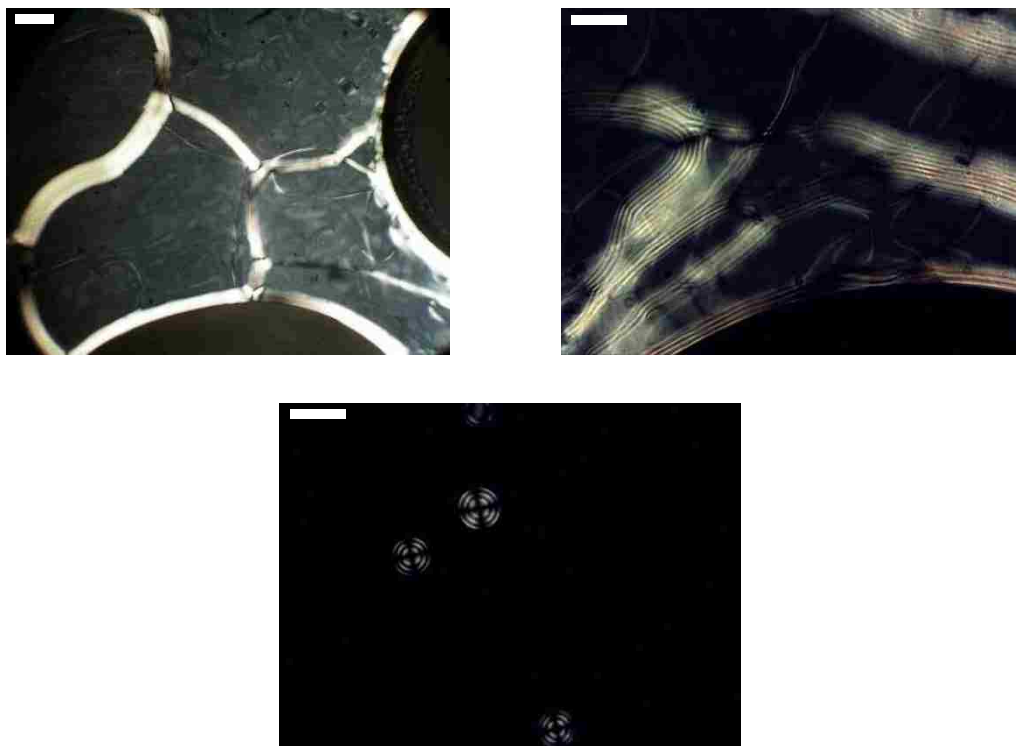
Figure A3.22 Composition: 15.4 wt% PBLG, 10.0 wt% silica, 74.6 wt% pyridine. (MC.1.52D) Scale bar is 100 microns.

Figure A3.23 Composition: 20.9 wt% PBLG, 13.6 wt% silica, 65.5 wt% pyridine. (MC.1.52F) Scale bar is 100 microns.

Table A3.1 Compositions for isotropic samples in phase diagram for 400 nm (diameter) silica-PBLG hybrid particles.

Sample Name	wt% PBLG	wt% Silica-PBLG	wt% Pyridine
MC.1.41A	9.9	9.7	80.4
MC.1.41B	12.2	12.1	75.7
MC.1.41C	12.9	12.7	74.4
MC.1.45A	8.0	14.5	77.5
MC.1.46A	0	10.2	89.8
MC.1.46B	0	12.3	87.7
MC.1.46C	0	15.3	84.7
MC.1.46D	0	25.9	74.1
MC.1.46E	0	29.1	70.9
MC.1.51F	11.8	2.5	85.7

APPENDIX B. MATLAB PROGRAM TO GENERATE COORDINATES FOR CORE-SHELL BEAD MODEL

```
**generates spiral coordinates around central point
r=1;
center (3,1)=0;
n=30;
p=zeros (3,n);

for i = 1 : n
    cosphi = ((n - i)*(-1.0)+(i - 1)*(+1.0))/(n - 1);
    sinphi = sqrt(1.0-cosphi^2);

        if ( i == 1 || i == n )
            theta = 0.0;
        else
            theta = theta + 3.6 / ( sinphi * sqrt ( n ) );
            theta = mod ( theta, 2.0 * pi );
        end

    p(1,i) = center(1,1) + r * sinphi * cos ( theta );
    p(2,i) = center(2,1) + r * sinphi * sin ( theta );
    p(3,i) = center(3,1) + r * cosphi;

end

**print results to a text file
fileID = fopen('spicoo.txt','w');
fprintf(fileID,'%6s %10s %10s\n','x','y','z');
fprintf(fileID,'%8.5f %10.5f %10.5f\r\n',p);
fclose(fileID);
type spicoo.txt

**view spiral in graphics window
x=p(1,:);
y=p(2,:);
z=p(3,:);
scatter3 (x,y,z,'filled'), view (-60, 60), view (40, 35);
```

```
plot3(x,y,z);
grid on
axis square

**"grow" polypeptide chain from sphere surface and print results to a text file
fileID = fopen('fbA.txt','w');
for i=100:200;
    b=i*p;
    c=b.';
    fprintf(fileID,'%8.2f %15.2f %22.2f\r\n',b);
end
fclose(fileID);
type fbA.txt;
```

VITA

Melissa Collins, a native of New Orleans, Louisiana, received her Bachelor's degree in chemical engineering from Louisiana State University in 2003. Melissa was accepted into the chemistry graduate program at Louisiana State University where she will complete the degree of Doctor of Philosophy in December of 2013.